ADVANCES IN GEOMATICS

Volume: 04 - Issue: 01 - April 2026 e-ISSN: 3023-4980

INTERNATIONAL REFEREED JOURNAL
PUBLISHED TWICE A YEAR
OPEN ACCESS

ADVANCES IN GEOMATICS

Volume: 04 - Issue: 01 - April 2026 e-ISSN: 3023-4980

INTERNATIONAL REFEREED JOURNAL
PUBLISHED TWICE A YEAR

OPEN ACCESS

Powered By
OJS
OPEN JOURNAL SYSTEMS

Special Thanks to
Assoc. Prof. Elvan ATAMTÜRK
for assuming the editorship of this issue and designing cover and interior pages...

April 30, 2026

ADVANCES
IN GEOMATICS
e-ISSN: 3023-4980

CONTACTS

https://aigjournal.com advancesingeomatics@gmail.com

+90 262 303 32 46

ADVANCES IN GEOMATICS
e-ISSN: 3023-4980

INDEXES

Google Scholar

OpenAIRE

ROAD

ADVANCES
IN GEOMATICS
e-ISSN: 3023-4980

REVIEWERS OF THIS ISSUE

Arzu Erener, Prof.
Kocaeli University - Turkey

Resul Çömert, Assoc. Prof.
Eskişehir Technical University - Turkey

Murat Selim Çepni, Assoc. Prof.
Kocaeli University - Turkey

İsmet Yener, Assoc. Prof.
Artvin Çoruh University - Turkey

Özer Akyürek, Assoc. Prof.
Kocaeli University - Turkey

Hale Öncel, Asst. Prof.
Konya Technical University - Turkey

Mohamed Freeshah, Asst. Prof.
Benha University – Egypt & UAE University – UAE

Efdal Kaya, Asst. Prof.
İskenderun Technical University - Turkey

Muhammad Arqim Adil, Ph.D.
Wroclaw University of Environmental and Life Sciences - Poland

Hamdullah Livaoğlu, Ph.D.
Kocaeli University - Turkey

Nik Mohd Zarifie Hashim, Ph.D.
Technical University of Malaysia Malacca - Malaysia

ADVANCES
IN GEOMATICS
e-ISSN: 3023-4980

ABOUT

Advances in Geomatics (AIG) is a peer-reviewed scientific journal dedicated to the dissemination of cutting-edge research in the field of geomatics. The Journal publishes English language original research articles, review papers, and technical notes in the multidisciplinary domain of geomatics.

AIM

Advances in Geomatics has started its publication life in 2023. This journal has embarked on the Open Access Policy with the idea that scientific information produced by academics, professionals, and others can be accessed by anyone, both locally and internationally, without any limitation. The journal aims to publish high-quality research articles, review papers, and technical notes that contribute to the understanding, development, and application of geomatics principles, technologies, and methodologies.

SCOPE

Advances in Geomatics welcomes contributions from researchers, academicians, professionals, and practitioners in the multidisciplinary domain of geomatics, including but not limited to the following areas: Geospatial data acquisition, geospatial data processing and analysis, geospatial data management, geospatial information systems, geospatial applications, geomatics for sustainable development, the journal encourages original research that pushes the boundaries of geomatics, promotes interdisciplinary collaborations, and addresses emerging challenges in the field.

PUBLICATION POLICIES

Advances in Geomatics is an international refereed journal that adopts double-blind peer-review process. Editorial board of our journal follows Editorial Policy of the Council of Scientific Committee.

PUBLICATION PERIOD

Advances in Geomatics is published twice a year in October and March. Publications are made from the following areas, which will contribute to the development of geomatics discipline and contribute to the literature: Other disciplines assessed in relation to geomatics, civil, geography, geophysics, geology, environmental and other engineering sciences, etc.

ADVANCES
IN GEOMATICS
e-ISSN: 3023-4980

FROM THE EDITOR

Dear academics, practitioners and our readers;

It is with great pleasure and enthusiasm that I welcome you to the inaugural issue of "Advances In Geomatics." As the Editor-in-Chief of this esteemed journal, I am honored to present a platform dedicated to the dissemination of cutting-edge research and innovation in the field of geomatics.

Geomatics, as a multidisciplinary science, plays a pivotal role in our understanding and management of the Earth's resources. The articles in this issue reflect the diverse range of topics within the geomatics domain, from geospatial technology and remote sensing to geographic information systems (GIS) and spatial analysis.

Our goal with "Advances In Geomatics" is to foster collaboration and exchange of knowledge among researchers, academics, and professionals in the geospatial community. The peer-reviewed articles featured in this issue represent the latest advancements and contribute to the ongoing discourse in geomatics.

I extend my gratitude to the authors for their valuable contributions and to the dedicated reviewers who have rigorously evaluated the manuscripts. Their commitment to maintaining the highest standards of scientific excellence is commendable.

As we embark on this scholarly journey together, I encourage readers to explore the diverse perspectives presented in this inaugural issue. "Advances In Geomatics" aims to be a catalyst for further advancements, discussions, and collaborations in the dynamic field of geomatics.

I look forward to your continued support and engagement with "Advances In Geomatics." May this journal serve as a source of inspiration and knowledge for all those passionate about advancing the frontiers of geomatics.

Sincerely,

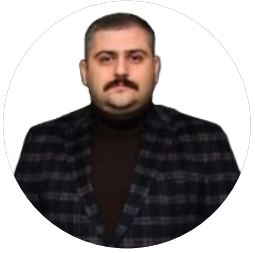

Erman ŞENTÜRK, Assoc. Prof.
Editor

ADVANCES
IN GEOMATICS

ADVANCES IN GEOMATICS

VOLUME 04 • ISSUE 01 • APRIL 2026
e-ISSN: 3023-4980

ORIGINAL ARTICLE

Submission: 27/02/2026
Accepted: 18/04/2026

A BAYESIAN APPROACH TO INTEGRATE AND PREDICT LAND COVER CHANGES IN THE CONTEXT OF LAND SURFACE TEMPERATURE VARIATIONS USING MULTISPECTRAL REMOTE SENSING DATA

Nadeeka A.M.T.[1]* **Duminda WELIKANNA[2]**

[1] The State Key Laboratory of Information Engineering in Surveying, Mapping and Remote Sensing, Wuhan University, China .

[2] Department of Surveying and Geodesy, Faculty of Geomatics, Sabaragamuwa University of Sri Lanka, Sri Lanka.

* Corresponding Author: Nadeeka A.M.T., tharukaggc@gmail.com 0009-0004-4712-5553

ABSTRACT

Land Surface Temperature (LST) is an important geophysical parameter in global energy balance studies and hydrologic modeling. Many studies have suggested that there is a strong correlation between LST and Land Cover (LC) changes due to its sensitivity to vegetation cover. Due to rapid urbanization and population growth, significant changes in LC are caused, which directly contribute to climate change through a variety of processes causing changes in LST. Thermal remote sensing is sensitive to an object's temperature and emittance depending on the wavelength. The objective of this experiment is to build a mathematical model to investigate the relationship between LST and the LC changes in Sri Lanka. The model built in the study could be used to analyze relationships between parameters depending on their frequency distributions, which is quite useful in the applied science domain. The model is based on Bayes' theorem, which determines the conditional probability of the events. Landsat 8 OLI/TIRS images throughout 2015 to 2020 were classified into five LC classes as water, soil, vegetation, impervious, and cloud using Support Vector Machine (SVM) classification. LST was retrieved for the same period using the standard equations for LST retrieval by Landsat 8 using the normalized difference vegetation index (NDVI). Multispectral bands were used for the LC classification, and thermal bands were used to obtain the LST. Vegetation cover has been significantly affected by the changes in LST, while other LC types show a less significant relationship with the LST. The novelty of this study lies in applying a Bayesian probabilistic framework to quantify the degree of association between LC types and LST using frequency distributions. Unlike traditional correlation-based approaches, this model enables a more robust conditional probability estimation, offering a more nuanced understanding of how each LC type interacts with LST variations. This probabilistic insight can be particularly useful for predictive land management and climate modeling.

Keywords: Land Surface Temperature, Land Cover, Bayesian Theorem, Landsat 8, Support Vector Machine.

Cited As: Nadeeka, A. M. T., & Welikanna, D. (2026). A Bayesian Approach to Integrate and Predict Land Cover Changes in the Context of Land Surface Temperature Variations Using Multispectral Remote Sensing Data, Advances in Geomatics, 4(1), 1-34. https://doi.org/10.5281/zenodo.20541417

INTRODUCTION

Land surface temperature (LST) serves as a manifestation of the energy flow in the interactions linking the land surface with both atmosphere and biosphere (Tan et al., 2020) which is an important geophysical parameter in many aspects of the Geosciences mainly to get an overall understanding of land-surface processes at different scales. The temperature felt when the land surface is touched with the hands or the skin temperature of the ground is defined as the LST (Avdan & Jovanovska, 2016). Climate change and global warming have become two of the major concerns in recent decades. Global climate change, hydrological and agricultural processes, urban land use/land cover, Land and atmospheric effects, Crop management, water management, forest fire monitoring, urban heat islands, deforestation, draughts, surface water evapotranspiration are some of the applications of studying and measuring LST variations. Due to rapid urbanization and population growth significant changes in Land Cover (LC) are caused. Human activities are hugely affected by the Earth's vegetative cover which directly contributes to climate change through a variety of processes causing changes in LST. Many studies have suggested that there is a high correlation of LST the LC changes due to its sensitivity to vegetation cover and soil moisture.

Thermal remote sensing is sensitive to objects' temperature and emittance depending on the wavelength. Further, it also provides regional and global coverage at good temporal and spatial resolutions. Land surface temperature has a strong correlation with LC Changes and it could be estimated with a mathematical model developed using Bayes theorem. LST and LC are inherently related spatial parameters that could be assessed using Thermal and multispectral remote sensing respectively. LST varies spatially according to soil type, LC, and land use and temporally with the time of day and season of the year. Satellite observations are important for observing LST due to their spatial and temporal coverage (Richards & Jia, 2005, p. 195). Due to LC changes, rapid urban expansions are caused, which is highly affecting the ecological environmental process at local and regional levels (Guha et al., 2020).

Sun. Q. et al. have integrated remote sensing, GIS, landscape ecology, and statistical analysis methods to study the urban thermal environment in Guangzhou, China. They have focused on the different indices (NDVI, NDBI, NDBaI, and MNDWI) to analyze the relationships between land surface temperature (LST) and land use land cover (LULC) using multiple regression analysis with the Landsat 7 TM data. The elevation data extracted from the DEM has been added to the computation. The maximum likelihood classification method has been used for the LC classification. Finally, the study has revealed that LST increased with the density of urban built-up and barren land due to sparse vegetation and bare soil in barren lands. LST has decreased with vegetation cover (forest, grassland, and cropland), where forest had the highest mean NDVI. Water has the lowest mean NDVI but not the highest mean LST, which is due to the high thermal inertia and convection of water. The correlation between MNDWI, DEM, and LST was found to be negative, which implies that pure water would

decrease the surface temperature and polluted water would increase the surface temperature. Both the qualitative and quantitative analysis of this study showed that land use has a great influence on LST. Therefore, the results obtained by the study could be used to mitigate the urban heat island effect with appropriate land use planning.

Sandipta Das, S., and Angadi, D.P., have used Landsat TM/ETM+ data seasonally (January, April, and November) to identify LST variations for two different periods of 1990 and 2016 in their case study of Barrackpore Subdivision, West Bengal, India. Different indices; the normalized difference vegetation index (NDVI), the normalized difference moisture index (NDMI), the normalized difference built-up index (NDBI), and the normalized difference water index (NDWI) were derived, and regression analysis was used to analyze and validate the relationship between LST and LULC. The spatial autocorrelation method of the Getis-Ord Gi formula has been used to delineate the concentration of hotspot and cold spot areas. The positive correlation between LST and NDBI has confirmed that impervious surfaces have strongly influenced the increase in surface temperature. They could have revealed that vegetation, water bodies, and wetlands are negatively related to LST while built-up land is positively related. The positive correlation exhibited by the Seasons statistical relationship between LST and NDBI has confirmed that impervious surfaces have strongly affected surface temperature. The regression line has shown a negative relationship between LST and wetlands and waterbodies, which shows the LST effects are very low over extremely humid or moist areas. They have considered only two years for the analysis. The obtained results may be stronger if they could consider some more years between the considered 25 years. The study could be used by the municipal authority to implement new decision policies and management to reduce the effects of LST on sustainable development in the future

A time series analysis was carried out as a case study in the Atlanta metropolitan area by Fu. P. and Weng. Q. to illustrate LULC change and its impact on land surface temperature (LST) variations using the Landsat TM/ETM+ images from 1984 to 2011. The LCs were classified as water, barren land, shrub land, urban-low intensity, urban medium intensity, urban-high intensity, crops, herbaceous, pasture, and woody wetlands using the Continuous Change Detection and Classification (CCDC) algorithm. The classification accuracy was checked with the Random Forest. The time series LSTs were determined using the single channel algorithm, which can derive LSTs independent of most of the necessary atmospheric profiles in empirical ways with high accuracy. This algorithm required only the parameters of water vapor and land surface emissivity. The final results were performed with an average classification accuracy of 89% and a change detection accuracy of 92%. The cloud-, cloud shadow and snow-contaminated pixels are excluded from the analysis. The larger trend change of the urban LCs has shown the LSTs were influenced by the urbanization-induced LC changes. They have identified that the conversion of evergreen forests to medium-intensity urban land generated the largest difference in annual LST variation. To reduce the outlier effects, the study has used the locally

weighted regression smoother (LOESS) scheme for the decomposition analysis. The effectiveness of the algorithm may depend on the number of clear-sky pixels available for the study area.

Guha, S., et al. have focused on estimating the land surface temperature of Raipur City in India, emphasizing the urban heat island (UHI) and non-UHI inside the city boundary and their relationship with LULC using Landsat 8 (OLI/TIRS) data. NDVI, NDWI, and NDBI were used to perform LULC classification for vegetation, water, and built-up areas, respectively, and the NMDI index for dry soil and bare lands. The study has been carried out on four satellite images, considering four different seasons: pre-monsoon, monsoon, post-monsoon, and winter in the same year. The mono-window algorithm was used to derive LST, where ground emissivity, atmospheric transmittance, and effective mean atmospheric temperature are considered the three required parameters. MODIS datasets have been used for the validation of LST values as a reference image instead of taking in situ field measurements. They could identify the strongest correlation between LST and the LULC indices during the monsoon and post-monsoon seasons, while winter and pre-monsoon images show a comparatively weak correlation. In this study, the relationship between LST and some weather and terrain components has been analyzed, including elevation, wind speed, humidity, air temperature, and air pressure. A strong positive relationship was identified between air temperature and LST, while LST and air pressure had a strong negative relationship. LST and wind speed correlate moderately negatively, and humidity and LST have a weakly negative relationship. No linear correlation was found with the elevation. A negative relationship was observed between NDVI and NMDI with LST, while a positive relationship was observed with NDBI. No significant relationship has been identified between LST and NDWI. Furthermore, the relationships of LST to NDVI, NDWI, NDBI, and NMDI have been interpreted quantitatively by linear regression analysis (using Pearson's product-moment correlation coefficient) at the pixel level. This study can be further developed by considering other LULC indices such as the enhanced vegetation index, soil adjusted vegetation index, modified normalized difference water index, normalized difference mud index, burn area index, etc. to examine the better correlation with LST and other statistical methods and algorithms like the Spearman Rank Correlation Coefficient, the Kendall Correlation Coefficient, etc. to estimate the correlation between LST and different LULC indices.

Tan. J. et al. have studied the Dongting Lake area (China), which is a climate change-sensitive and ecologically fragile area, to determine the relationship between LST and LULC using Landsat TM/ETM+, DEM, and MODIS data. A single-window algorithm was used for the LST retrieval, which had the greatest consistency with the actual measurements. Also, the results were compared with the MODIS temperature products from the same time and identified a relative error of 2% or less. Using the decision tree methodology, which is based on the classification and regression tree (CART) algorithm for the LULC classification, the area was categorized into nine categories: water bodies, riparian forest, marshland, paddy fields, reed beach land, mud beach land, dry land, built-up land, and forest

land. The results showed that LST is significantly affected by LULC types. The LST of forest land and dryland is higher than that of other land types, and the LST of water bodies is much lower than that of other land types and also much lower than the mean LST of the study area. The NDMI showed a strong negative spatial correlation with LST, while the DEM, NDVI, and distance showed a weak spatial correlation with LST. This exploration of regional LULC and climate change patterns and processes can provide a typical case for a larger range of global change studies

Rheea.J. et al. have investigated the relationship between LC patterns and surface temperature using an advanced machine learning technique (random forest as well as simple linear regression). The purpose was to derive important spatial metrics of LC affecting surface temperature to provide information for alleviating heat stress and reducing the adverse impacts of drought in urban areas, considering two urban sites in Denver, Colorado, USA. Random forest is based on an ensemble approach to predicting a target variable by combining predictions from multiple Classification and Regression Trees (CART), which has the robustness to counteract noise, outliers, and overfitting. The LC map was derived from light detection and ranging (LiDAR) data with 0.5 m spatial resolution, and the LST map was derived using Landsat 5 Thematic Mapper (TM) data with 120 m spatial resolution. Maps were classified into four LC types: buildings, trees, grass, roads, and parking lots. Only trees, roads, and parking lots showed significant spatial metrics affecting surface temperature using both methods in their study. The results of this study provide information that can be used for planting trees and locating parking lots to alleviate heat stress in urban areas, especially during the summer. These measures can be used to reduce the adverse impacts of urban drought since the heat wave and drought are closely related and affect each other. The effect of land use on surrounding regions was not considered for analyses such as those of nearby large waterbodies, which affect large-scale circulations of climate and meteorological events

Many studies have suggested that there is a strong correlation between LST and LC changes due to their sensitivity to vegetation cover. The relationship between these two parameters has been scrutinized using regression-based analysis, mainly linear regression, in previous studies. However a model to integrate these parameters into a single framework is not being investigated or developed. The problem is to be addressed using a contextual Bayesian approach in the study. In regression analysis, the best-fitting value is determined by considering all the available data without considering the precision of the values, where outliers are also considered. The proposed Bayesian method directly gives the actual probability according to the occurrence of the events. It calculates the exact conditional probability of each single event within the 3*3 moving window, which is not affected by all the values in the dataset.

This experiment was performed to investigate the relationship between LST and LC using a mathematical model based on Bayes Theorem. Time series analysis was performed in this study from 2015-2020 to obtain LST and LC for each selected study area using the standard equations provided for

LST retrieval by Landsat 8 and SVM classification respectively. Here, five different cities with divergent climate conditions and three national forests were selected as the study area. Based on satellite images, vegetation Indices are used to estimate the percent vegetation cover in each pixel (Purevdorj et al., 2010) which is used for emissivity calculation in the LST retrieval process. The model built in the study could be used to analyze the relationship between parameters depending on their frequency distributions, which is quite useful in the applied science domain.

DATA AND METHOD

Model development

The model is developed based on two sample datasets (8 by 8 matrices) of LST and LC values, including five LC classes and five LST values.

29	29	29	28	28	27	27	28
29	29	28	28	27	27	27	27
29	28	28	26	27	27	27	28
28	28	28	28	29	29	28	28
28	28	28	27	27	27	28	28
29	26	28	28	27	27	27	28
28	28	28	28	29	29	28	28
28	28	28	27	27	27	28	26

(a)

1	1	1	2	2	3	3	3
1	1	2	2	2	3	3	3
1	2	2	4	3	1	3	2
2	2	2	1	1	1	2	2
2	2	3	3	3	2	1	2
1	4	3	2	1	1	2	2
2	2	2	2	1	1	2	2
2	2	2	3	3	3	2	4

(b)

Figure 1. (a) sample dataset for LST with values 26,27,28,29; (b) sample dataset for LC with values 1,2,3,4. Highlighted pixels show the respective LC classes when the LST value is 27.

A 3 by 3 moving window is considered to check the direct influences of neighboring pixels for probability calculation in each center pixel, and the resultant probability images are used for the analysis. The model development coding was done with MATLAB programming language.

27	27	28
27	27	27
29	29	28

3	2	1
1	1	2
1	1	2

P (1) = (5/9)
P (27|1) = (2/5)
P (27) = (5/9)

Figure 2. Probability calculation for the center pixel being LC class 1 for given LST value 27.

P (1|27) = P (1) *P(27|1)/P (27)

= (5/9) *(2/5)/ (5/9)

= (2/5)

Resulting probability - Conditional Probability of LC with respect to LST

The model was developed using equation (1), which calculates the conditional probability of each LC class concerning each LST value.

$$P_{t1}(\omega \mid T) = \frac{P_{t1}(\omega \cap T)}{P_{t1}(T)} = \frac{P_{t1}(\omega) * P_{t1}(T \mid \omega)}{\sum^{pixels(t_1)} P_{t1}(T) * P_{t1}(T \mid \omega)} \quad (1)$$

There are four unique LST values and four unique LC values included in the sample dataset. Therefore, four probability images per one LST class were generated by the model (for example: for LST value 26, the created probability images are related to the P (1|26), P(2|26), P(3|26), and P(4|26)). The same procedure was followed for each LST value, and finally, 16 probability images (4*4) were created. The highly affected LC for each LST value can be determined by the images with the highest probability; therefore, the highest probability images were selected by image plot analysis, and the percentage for the highest probability was calculated. Then the LC with the highest percentage was assigned to each LST value. See Appendix A for all probability images generated by the model for each area.

Table 1. Percentage for each LC in the highest portability images.

LST	LC	Percentage
26	4	100
27	3	62.5
28	2	81.5789
29	1	100

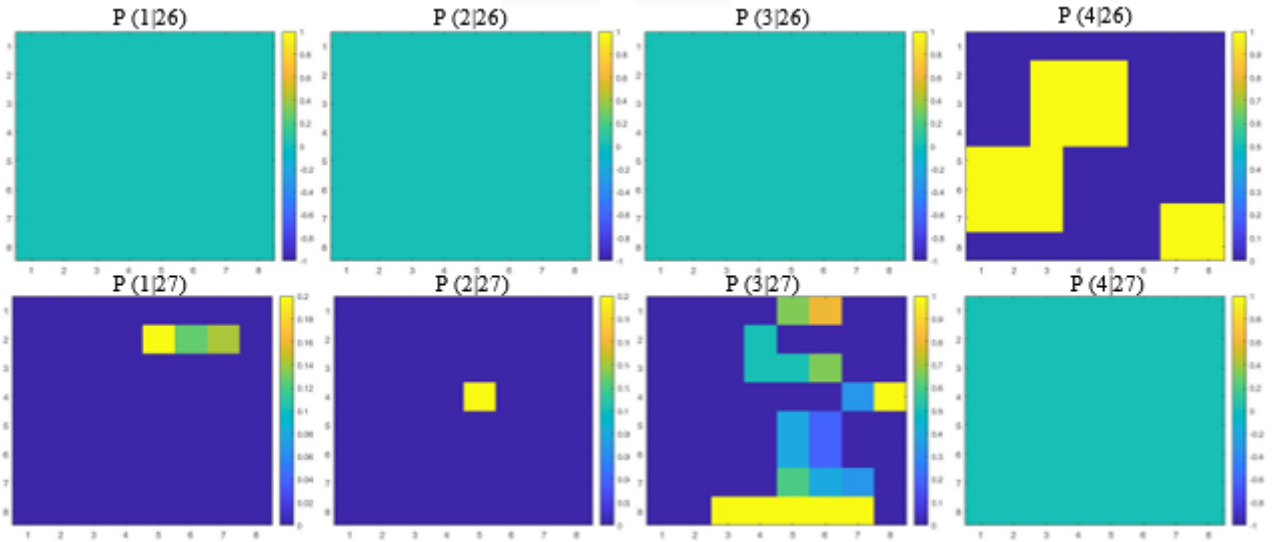

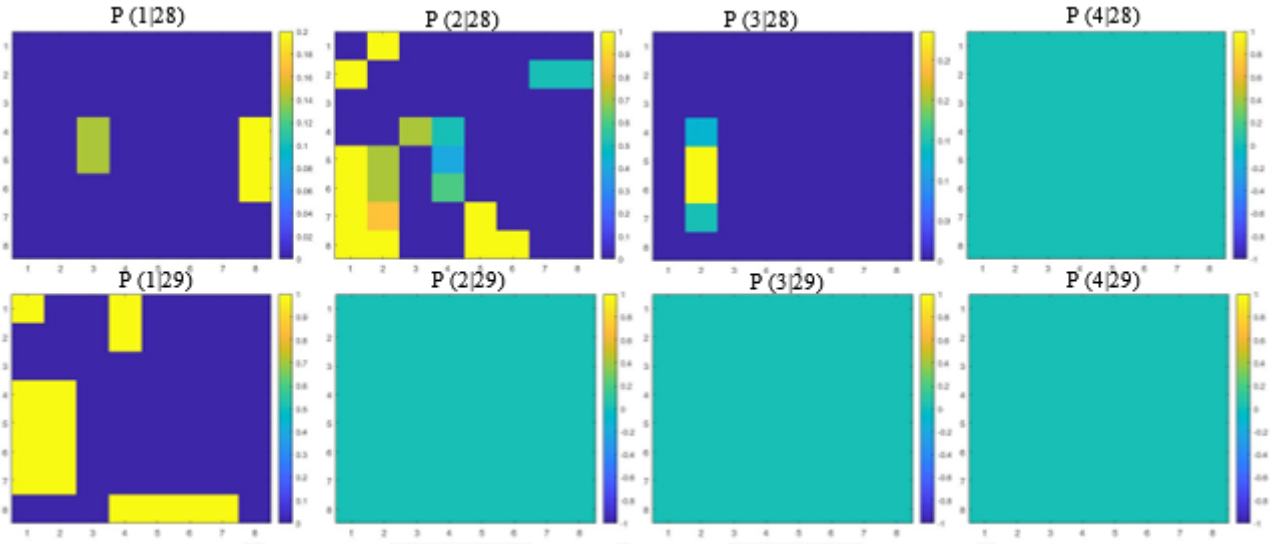

Figure 3. Highest probability for LST 26 with LC 4, LST 27 with LC 3, LST 28 with LC 2, and LST 29 with LC 1.

P(4|26)

0	0	0	0	0	0	0	0
0	0	1	1	1	0	0	0
0	0	1	1	1	0	0	0
0	0	1	1	1	0	0	0
1	1	1	0	0	0	0	0
1	1	1	0	0	0	0	0
1	1	1	0	0	0	1	1
0	0	0	0	0	0	1	1

P(3|27)

0	0	0	0	0.67	0.8	0	0
0	0	0	0.5	0	0	0	0
0	0	0	0.5	0.5	0.7	0	0
0	0	0	0	0	0	0.33	1
0	0	0	0	0.4	0.2	0	0
0	0	0	0	0.4	0.2	0	0
0	0	0	0	0.6	0.4	0.33	0
0	0	1	1	1	1	1	0

P(2|28)

0	1	0	0	0	0	0	0
1	0	0	0	0	0	0.5	0.5
0	0	0	0	0	0	0	0
0	0	0.71	0.5	0	0	0	0
1	0.71	0	0.4	0	0	0	0
1	0.71	0	0.6	0	0	0	0
1	0.86	0	0	1	0	0	0
1	1	0	0	1	1	0	0

P(1|29)

1	0	0	1	0	0	0	0
0	0	0	1	0	0	0	0
0	0	0	0	0	0	0	0
1	1	0	0	0	0	0	0
1	1	0	0	0	0	0	0
1	1	0	0	0	0	0	0
1	1	0	0	0	0	0	0
0	0	0	1	1	1	1	0

Figure 4. Highest probability Images for sample data sets which representing the best relationship of LC classes with each LST value; LST 26 with LC class 4, LST 27 with LC class 3, LST 28 with LC class 2 and LST 29 with LC class 1.

Model validation

The model validation is performed for a well-known area where the LC had a significant change in two consecutive years with Landsat OLI/TIRS Level-1 thermal and multispectral bands data by obtaining their LST and LC classification respectively. The LST estimation has done using the standard equations related with the NDVI and the Support vector machine (SVM) is used for the LC classification. Google earth and the Land Use LC maps are used as reference for LC classification.

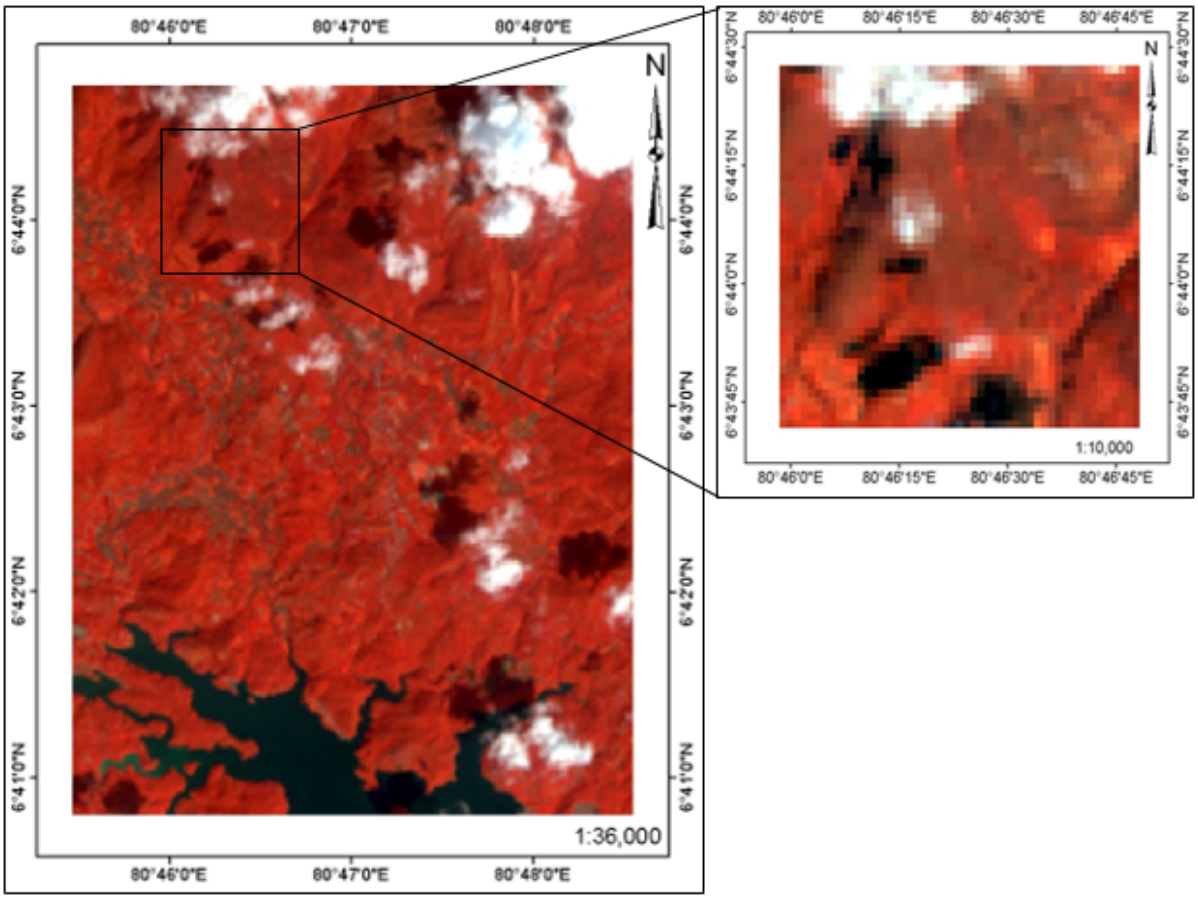

Figure 5. False color composite image in 2015, Belihuloya showing the area before the huge landslide occurred in 2016 with the zoom image; where the LCs were identified as vegetation and cloud.

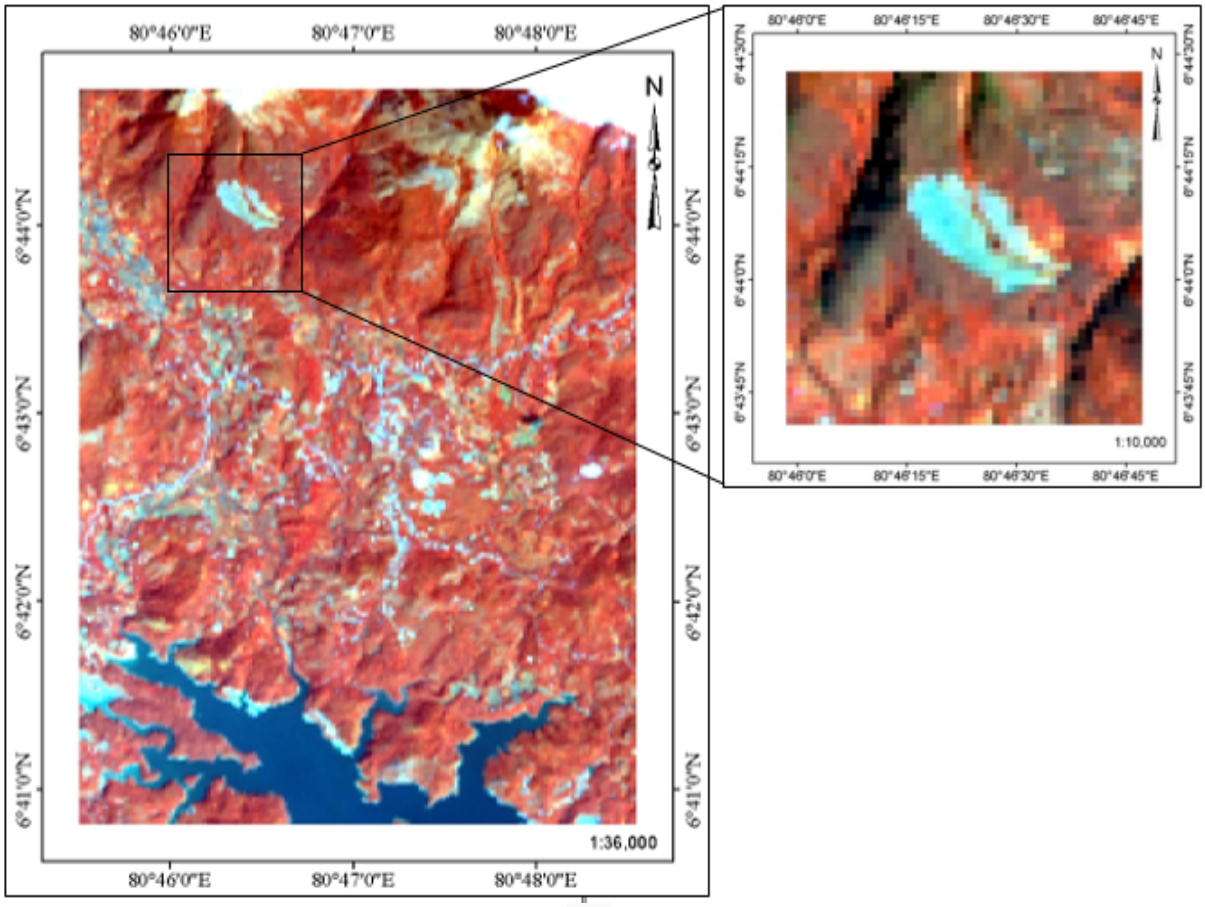

Figure 6. Comparison of LC change in Belihuloya, Sri Lanka area with Landsat 8 OLI\TIRS false-color composite images in 2016 where a huge landslide occurred and the vegetation cover has altered into Soil which is represented by the blue color patch of the zoomed image.

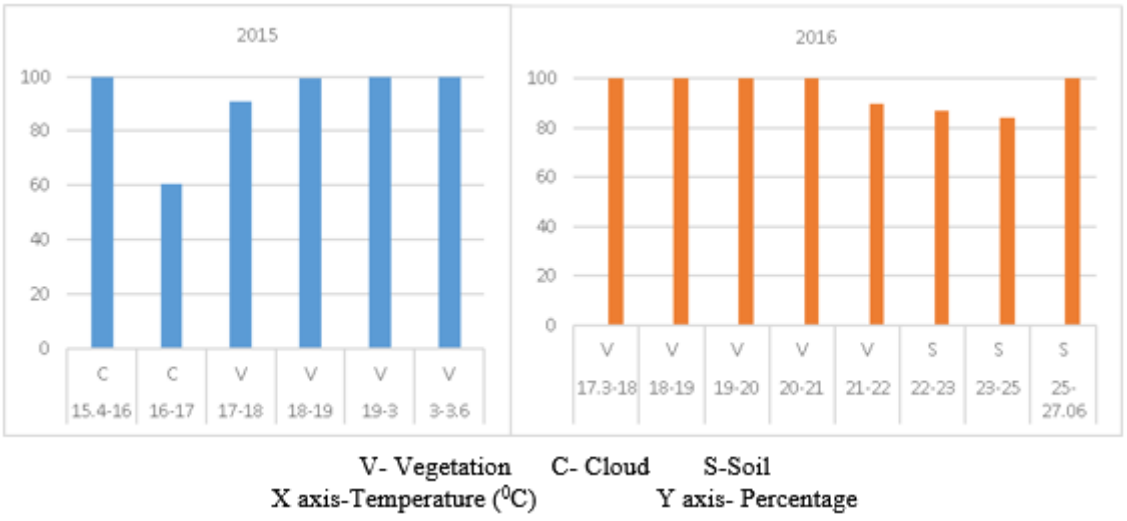

Figure 7. Model validation results that show Highly affected LCs percentage for LST ranges in 2015 and 2016 in the Belihuloya area with the changes of land covers in 2016 due to the landslide in this area.

The average LST for Belihuloya in 2015 was 18.76 C, and in 2016, it was 19.86 C. The highly affected LC classes were analyzed for each land surface temperature range. The model clearly shows that the LST increment has occurred due to the change of LC from vegetation to soil in 2016.

Regression analysis was performed with the R programming language and checked the relationship between the LST and LC classes for the selected area. It showed that the lowest LST values occurred due to the cloud cover, and the middle LST values were created by vegetation cover. The highest LST values occurred due to the soil cover in 2016. The regression analysis has also proved that the LC change has had a significant impact on the LST increment in 2016.

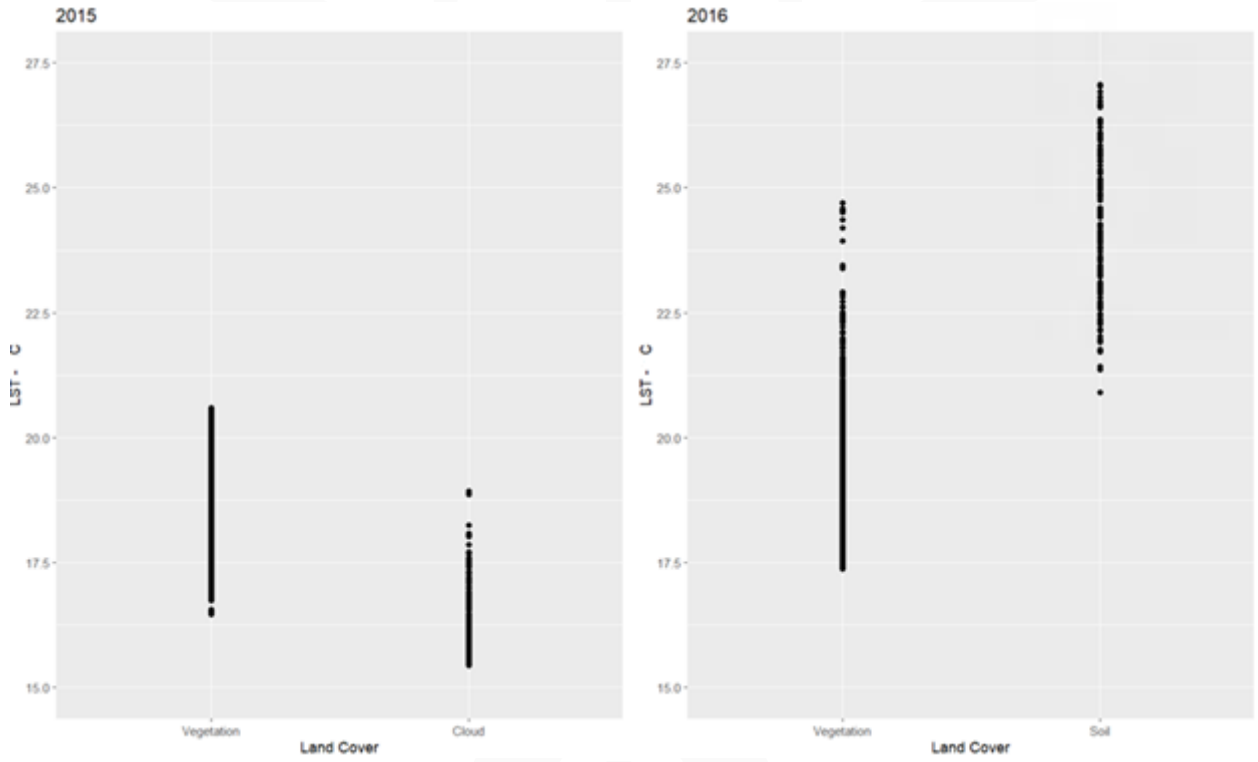

Figure 8. Regression Analysis for LST vs LC in 2015 and 2016 in Belihuloya area.

Land surface temperature calculation

Thermal band (Band 10, wavelength 10.60 µm –11.19 µm), Near Infrared band (band 5, wavelength 0.85 µm – 0.88 µm), and red band (band 4, wavelength 0.64 µm –0.67 µm) in Landsat 8 OLI/TIRS sensor data were used for LST calculation as shown in the following equations. The thermal band, Band 11, has not been used for the calculations due to its larger uncertainty in calibration with the recommendations of the USGS following January 6, 2014. This thermal band (band 10) was resampled using the nearest neighbor algorithm with a pixel size of 30 m to match the optical bands.

Top of atmospheric spectral radiance

$$L\lambda = ML * Qcal + AL - O_i \quad (2)$$

where ML represents the band-specific multiplicative rescaling factor (0.000342), Qcal is the Band 10 image, AL is the band-specific additive rescaling factor (0.1), and Oi is the correction for Band 10 (0.29) (Barsi et al., 2014).

Conversion of radiance to at-sensor temperature

$$BT = \frac{K2}{\ln[(K1/L\lambda)+1]} - 273.15 \quad (3)$$

where K1(1321.08) and K2 (777.89) stand for the band-specific thermal conversion constants from the metadata. For obtaining the results in Celsius, the radiant temperature is revised by adding the absolute zero (approx.–273.15 C) (Xu et al., 2004).

Calculating NDVI

Normalized Difference Vegetation Index (NDVI) can be used to calculate the Emissivity using percent vegetation of each pixel. For Landsat 8 OLI/TIRS images, Band 5 is representing NIR band and Band 4 is representing the red band. Following equation is used to calculate the NDVI

$$NDVI = \frac{NIR(Band5) - R(Band4)}{NIR(Band5) + R(Band4)} \quad (4)$$

NDVI was calculated in order to estimate land surface emissivity (LSE), which is a critical parameter for accurate LST retrieval. Since emissivity varies with vegetation density, NDVI provides a reliable way to determine the proportion of vegetation in each pixel. This step is therefore essential to correct for emissivity differences across land cover types and to improve the accuracy of the LST calculation

Calculating the proportion of vegetation

$$P_V = \left(\frac{NDVI - NDVI_{Min}}{NDVI_{Max} - NDVI_{Min}}\right)^2 \quad (5)$$

Calculating land surface emissivity (LSE)

$$\varepsilon = 0.004 * P_V + 0.986 \quad (6)$$

LSE is the efficiency of transmitting thermal energy across the surface into the atmosphere which is a proportionality factor that scales blackbody radiance (Planck's law) to predict emitted radiance. (Sobrino et al., 2004; Qin et al., 2001)

The constants 0.004 and 0.986 in the LSE equation are derived from empirical studies (e.g., Sobrino et al., 2004; Qin et al., 2001) that established a linear relationship between vegetation proportion (PV) and emissivity. These values have been widely used in LST retrieval studies using Landsat data

and are recommended in the remote sensing literature. They were chosen to ensure methodological consistency with previous research and to allow comparability of our results with other studies.

Retrieving the LST

$$Ts = \left(\frac{BT}{1 + [(\lambda BT / \rho) \ln \varepsilon \lambda]} \right) \quad (7)$$

where Ts is the LST in Celsius (C, (2)), BT is at-sensor BT(C), λ is the wavelength of emitted radiance (for which the peak response and the average of the limiting wavelength (λ=10.895) (Markham et al., 1985).

$$\rho = h\frac{c}{\sigma} = 0.01438mK \quad (8)$$

where σ is the Boltzmann constant (1.38 x 10^{-23} J/K), h is Planck's constant (6.626 x 10-^{34} J s), and c is the velocity of light (2.998 x 108 m/s) (Weng et al., 2004).

Using the above equations LST maps were generated and LST classes were assigned according to the color density of the generated map using density slice analysis. Finally obtained LST classes were transformed into .txt format and used as the LST input for the model. See appendix B for the LST Class maps of each area in each year.

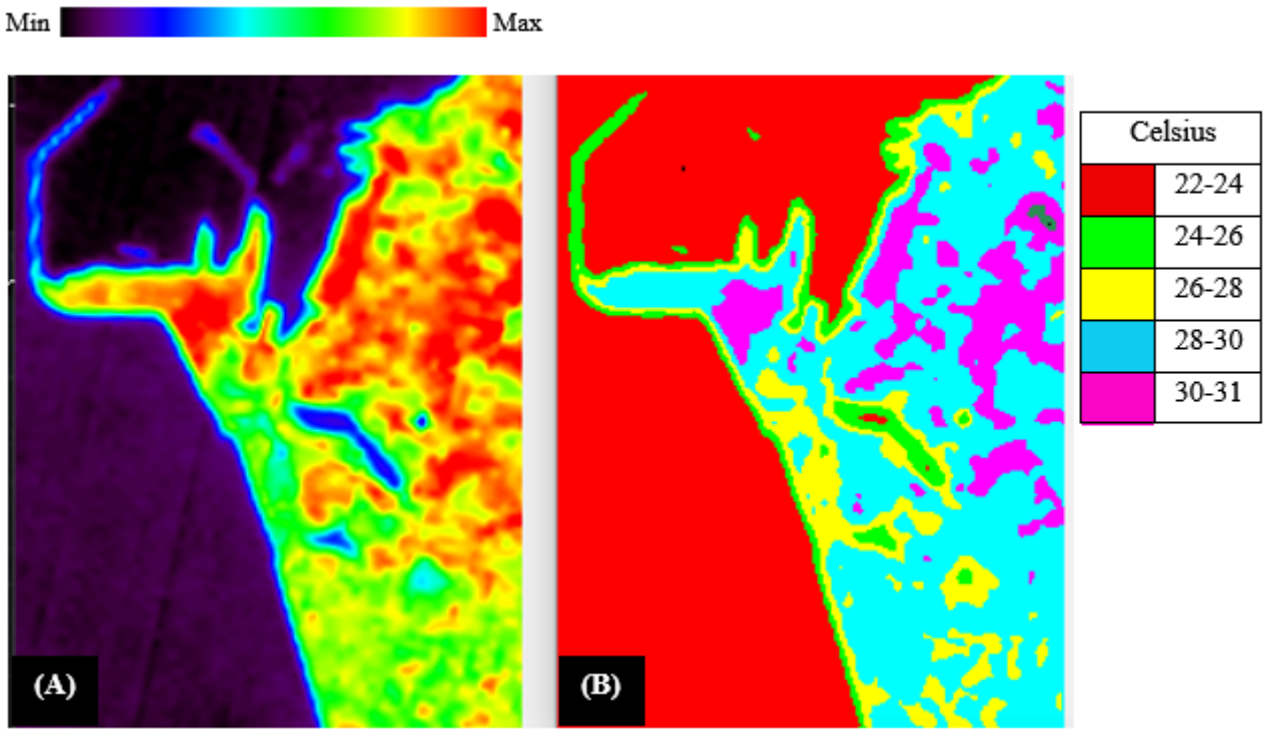

Figure 9. LST map (A) Generated for Colombo Area in 2016 and the LST class map (B) for the same area.

Land cover classification

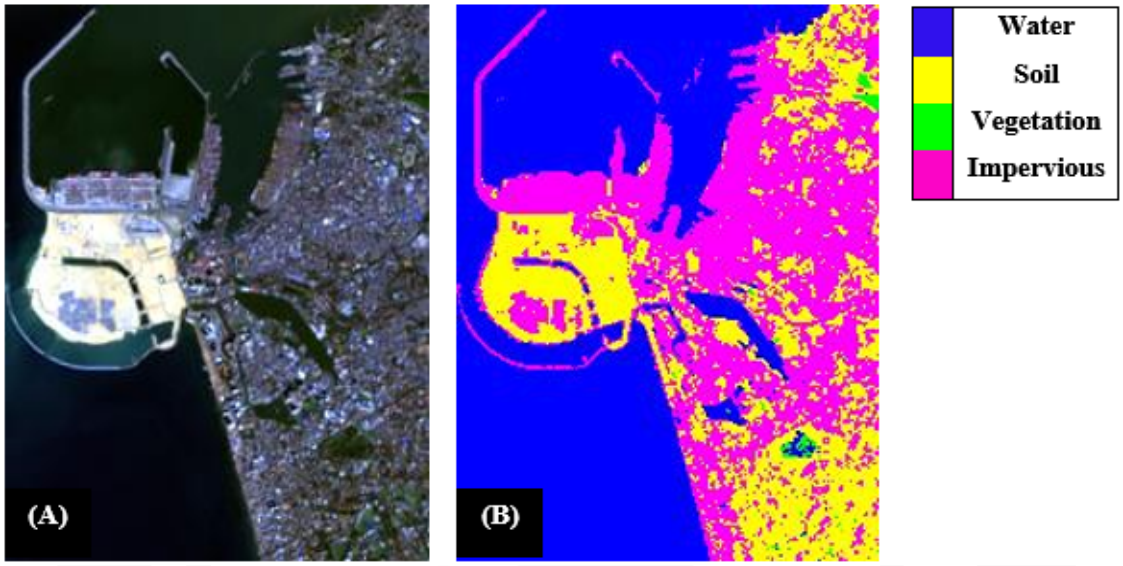

Figure 10. True color composite image(A) for Colombo Area in 2018 and the LC classification map (B) of the same image using SVM Classification showing the completed port city area.

Five major LCs were considered in the study as Vegetation, Water Impervious, Soil and Cloud. LC classification was performed with the Support Vector Machine Classification for each selected area. Google earth maps and Land Use LC maps by the Survey Department Sri Lanka were used as the reference data for sample generating.

Following the above procedure, the processing of LST retrieval and LC classification was done for the selected five cities from 2015 to 2020.These images were the input for the developed model in text format. As the output of the model, conditional probability of each LC class with respect to each LST values in each pixel of the image were calculated and after analyzing the obtained probability mages highly affected LC classes for each LST class was identified.

RESULTS

Colombo is the commercial capital and the largest city in Sri Lanka by population, which makes it a highly urban area. The LC maps are clearly showing how the LCs are changed in Colombo from 2015. The major change has occurred due to the construction of the port city, which spans 269 hectares of reclaimed land from the sea. Due to the absence of vegetation cover, the area is showing a higher LST compared with the other areas in the study, which have an average of 25.52 C. The model shows the lowest LST values are due to the water surface, and the highest are due to the impervious surface. The regression analysis shows that both the impervious and soil classes are highly affected by the higher LST values, and the Bayesian model has proven that impervious surfaces have had the greatest effect on the highest LST in each year except for 2020.

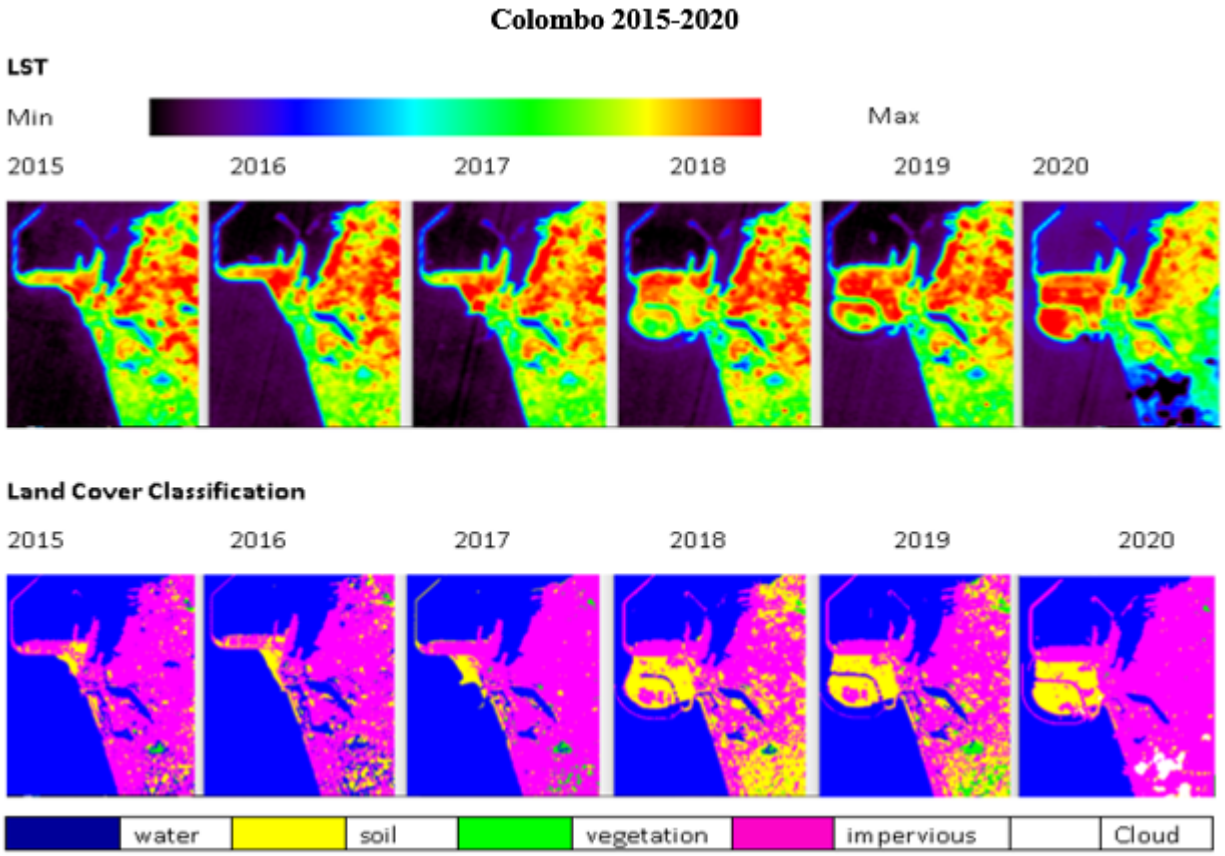

Highly effected LC classes for each LST range for Colombo area from 2015 to 2020

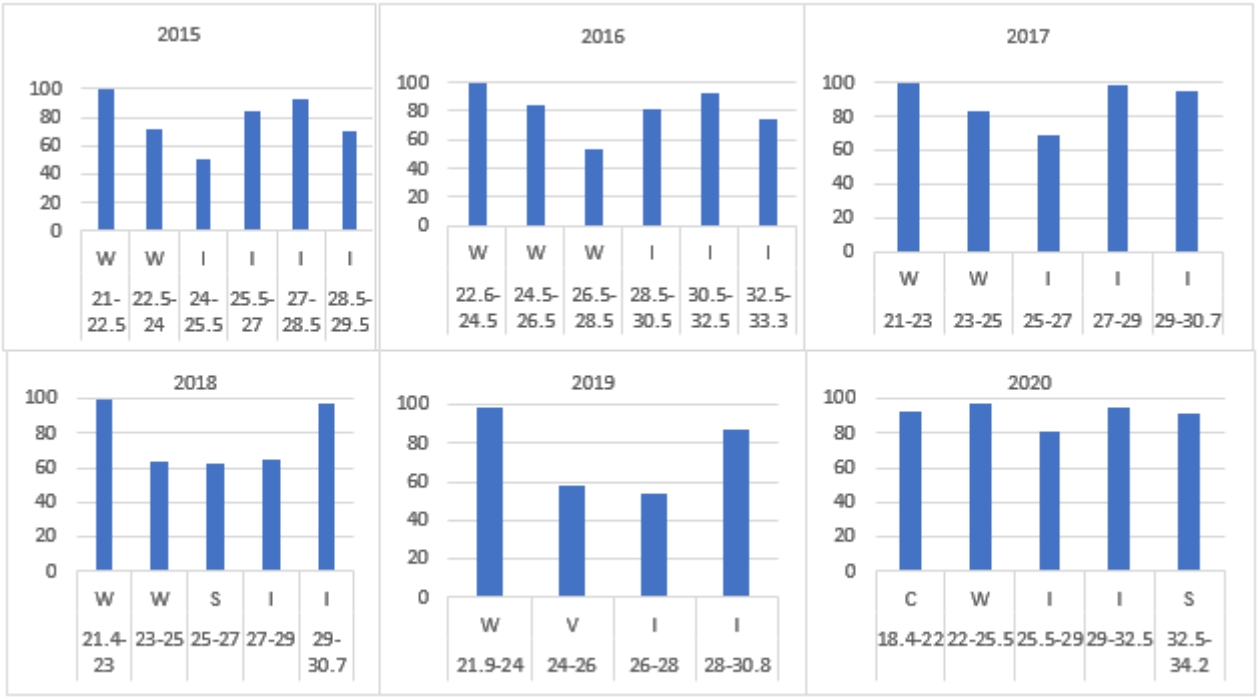

W-water I-Impervious V- Vegetation C- Cloud S-Soil

X axis-Temperature(^{0}C) Y axis- Percentage

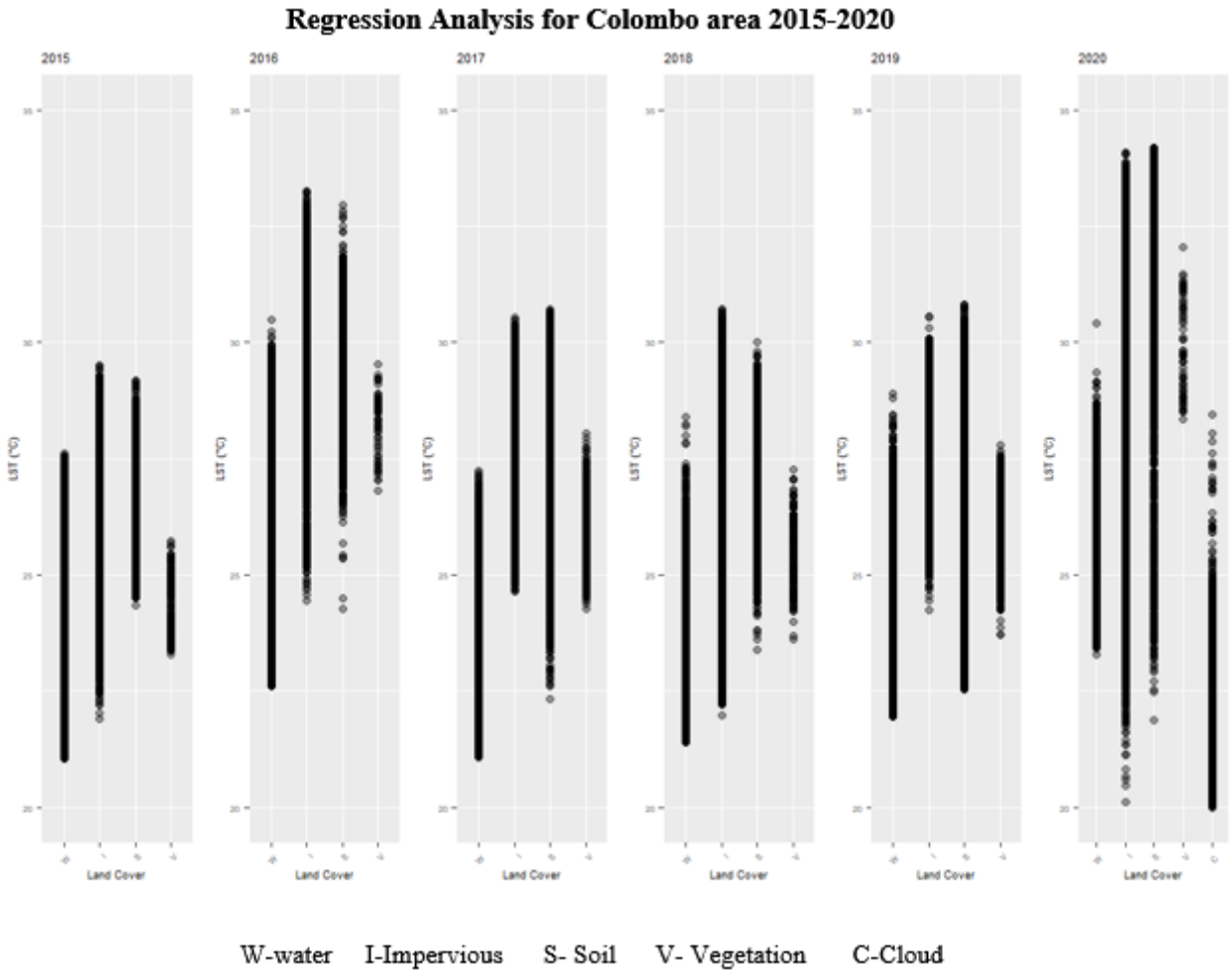

Figure 11. LST map, LC map, highly affected LCs and regression analysis of Colombo area from 2015-2020.

Ratnapura is very famous for being the gem trading center of Sri Lanka, which has a tropical rainforest climate. The study area consisted of a part of the 'Kalu River', which is the main irrigation source in the area. The area contains around 68% vegetation and 29% impervious surface. The model has shown that the impervious surface has contributed to the highest LST in the town area, and cloud cover and vegetation have affected the lower values of LST. The average LST has been recorded at 24.20 C throughout the 6 years, and the highest LST has been recorded in 2019 at 26.02 C while the minimum has been recorded in 2015 at 22.95 C. The regression analysis shows that the soil and impervious surfaces are highly affected for the highest LSTs in the area, while the clouds and vegetation are affected for the lowest LST.

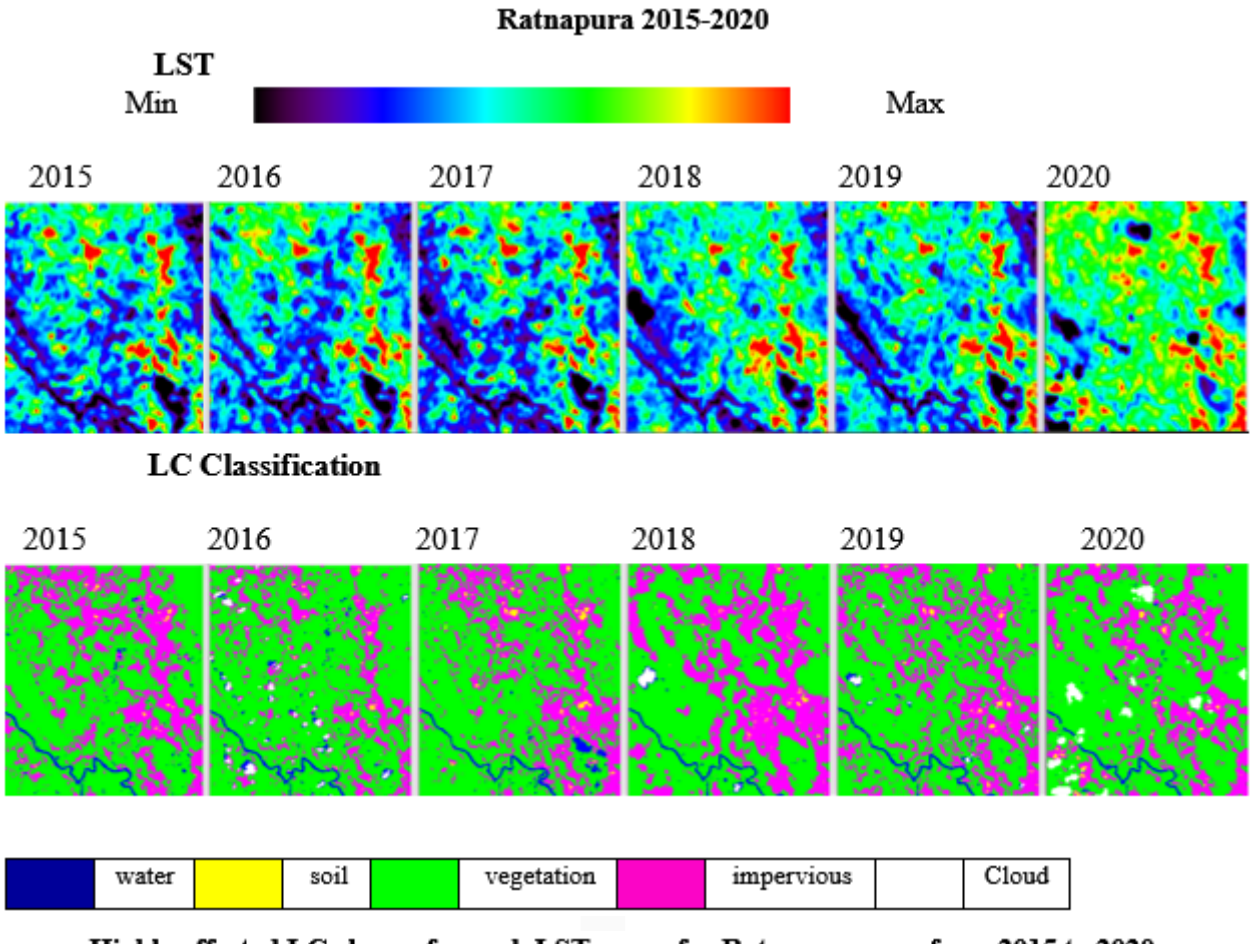

Highly effected LC classes for each LST range for Ratnapura area from 2015 to 2020

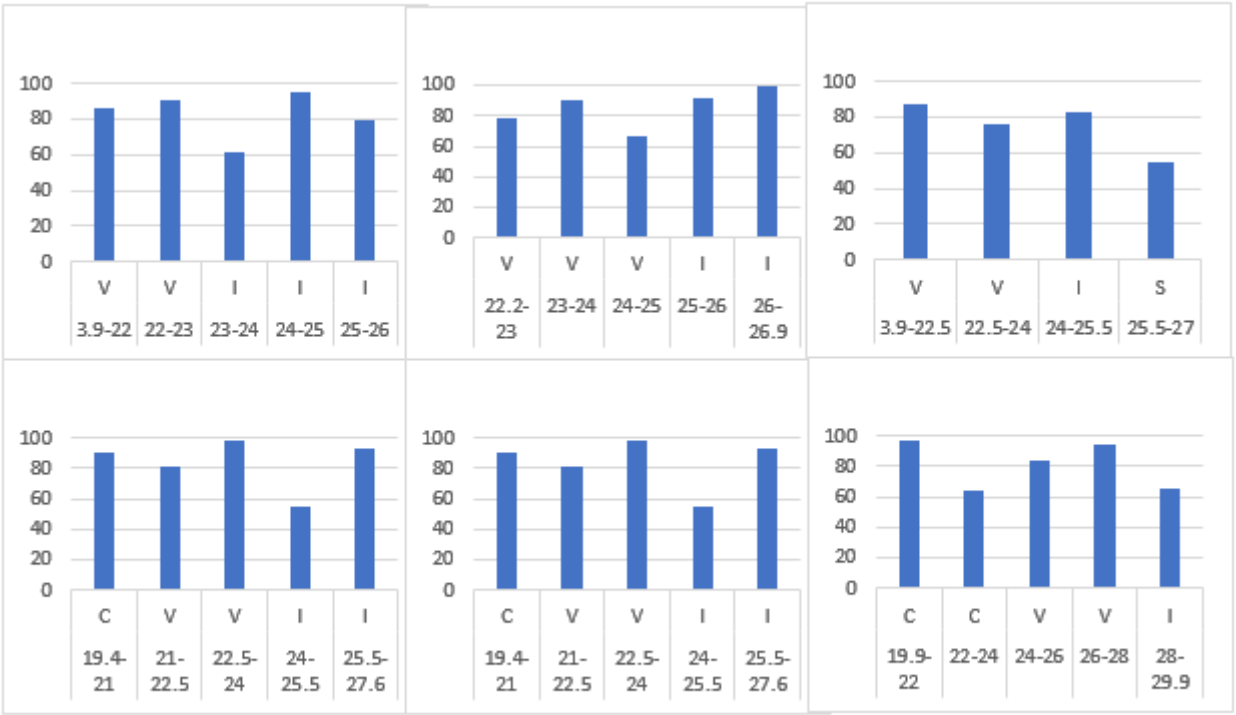

W-water I-Impervious V- Vegetation C- Cloud S-Soil

X Axis-Temperature(^{0}C) Y axis- Percentage

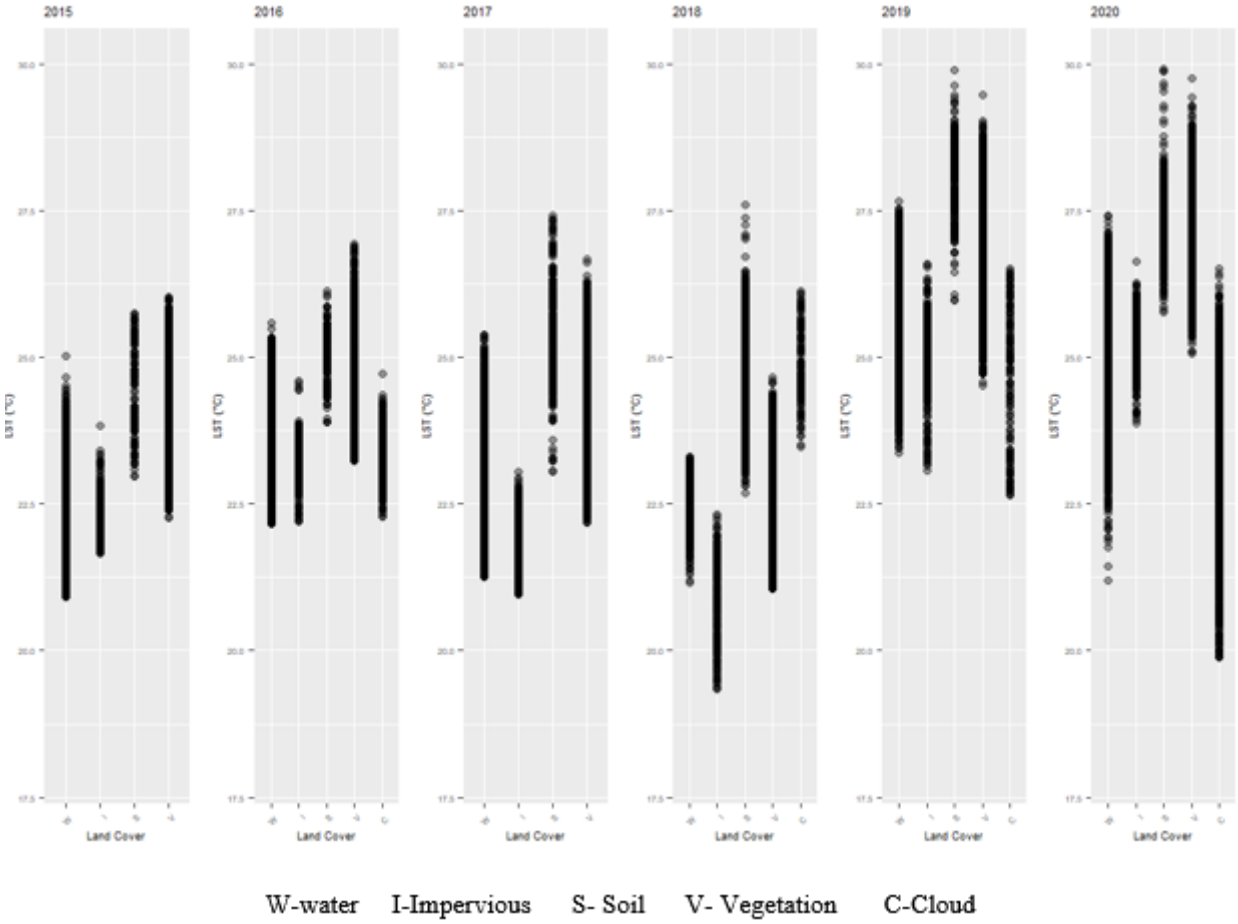

Figure 12. LST map, LC map, highly affected LCs and regression analysis of Ratnapura area from 2015-2020.

Kandy is a major tourist destination with a cooler climate than the coastal regions of Sri Lanka. The LC maps show the area contains a highly vegetated area of around 54% and an impervious surface of around 22%. The average LST has recorded as 24.67 C where the minimum and maximum LST has recorded as 22.4276 C and 28.53 C. The model has shown that the higher LST values are caused by the impervious surface, while the lower LST values are highly affected by the vegetation cover. According to the regression analysis, water and soil have contributed to the middle LST values, and impervious has contributed to the highest LST values in each year. The trend analysis of this Kandy area shows the LST has a great positive correlation with the impervious surface and a negative correlation with the vegetation.

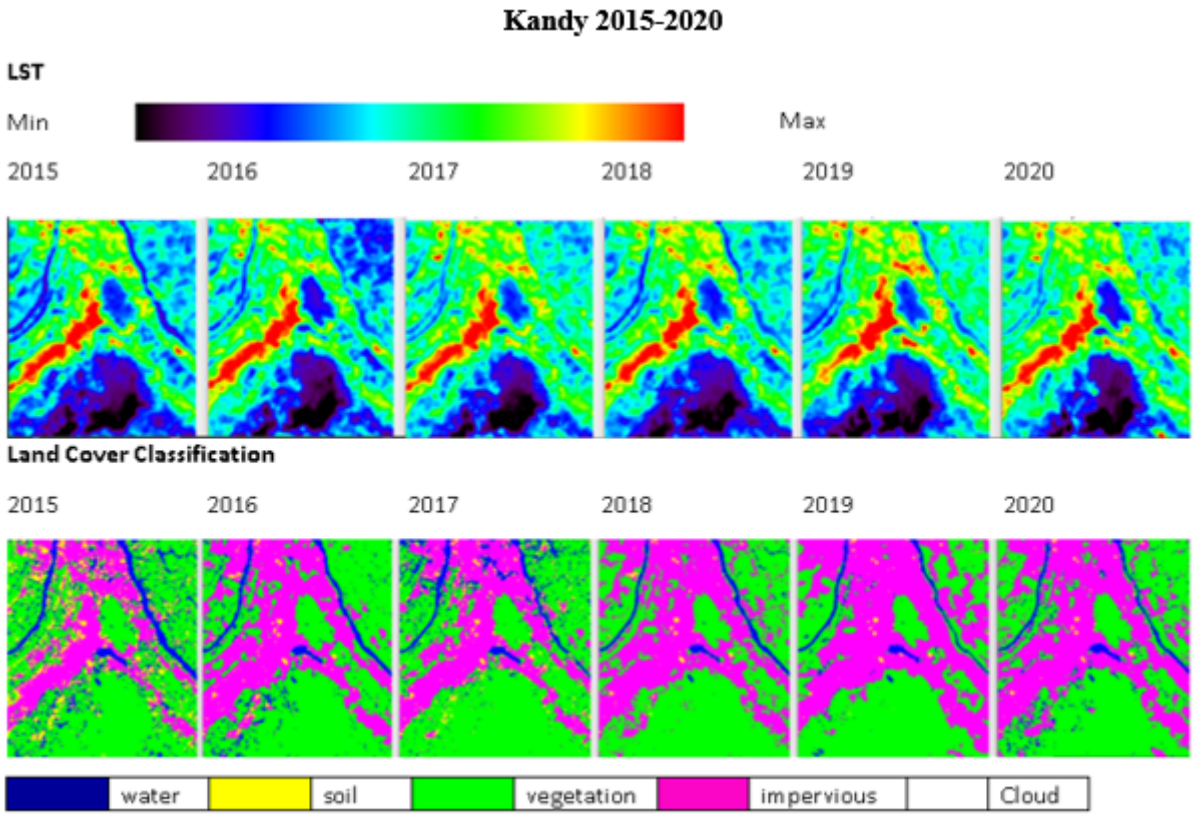

Highly effected LC classes for each LST range for Kandy area from 2015 to 2020

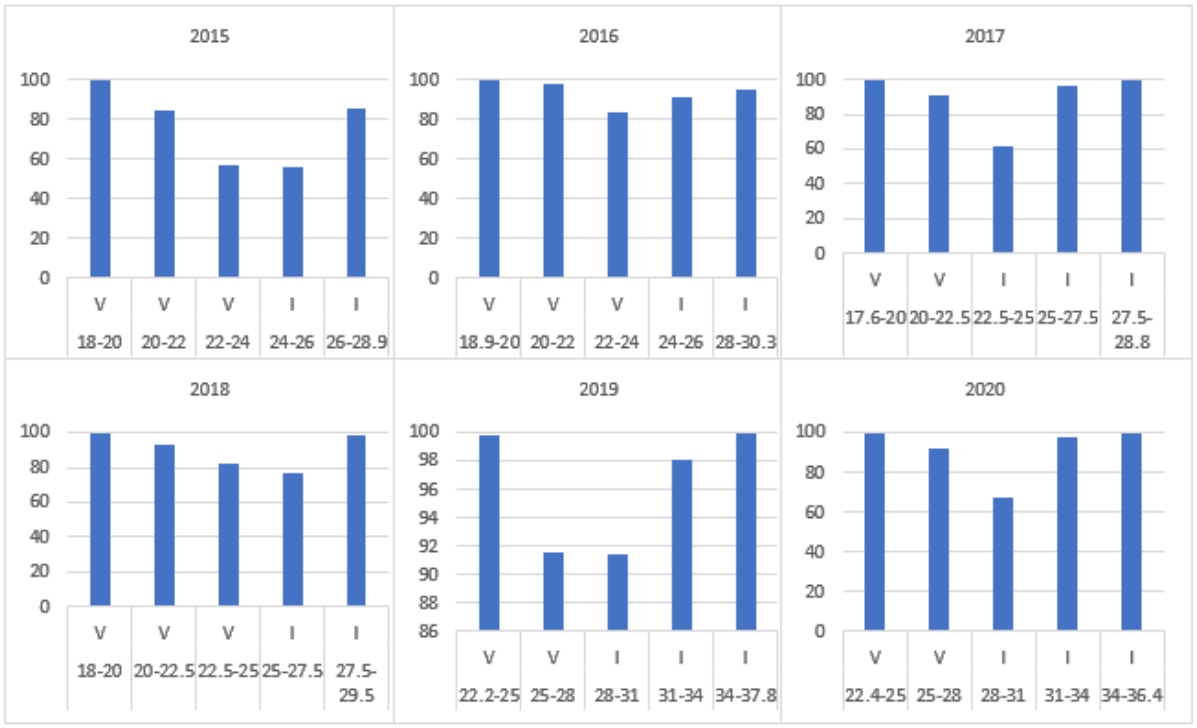

W-water I-Impervious V- Vegetation C- Cloud S-Soil

X – axis -Temperature(^{0}C) Y - axis- Percentage

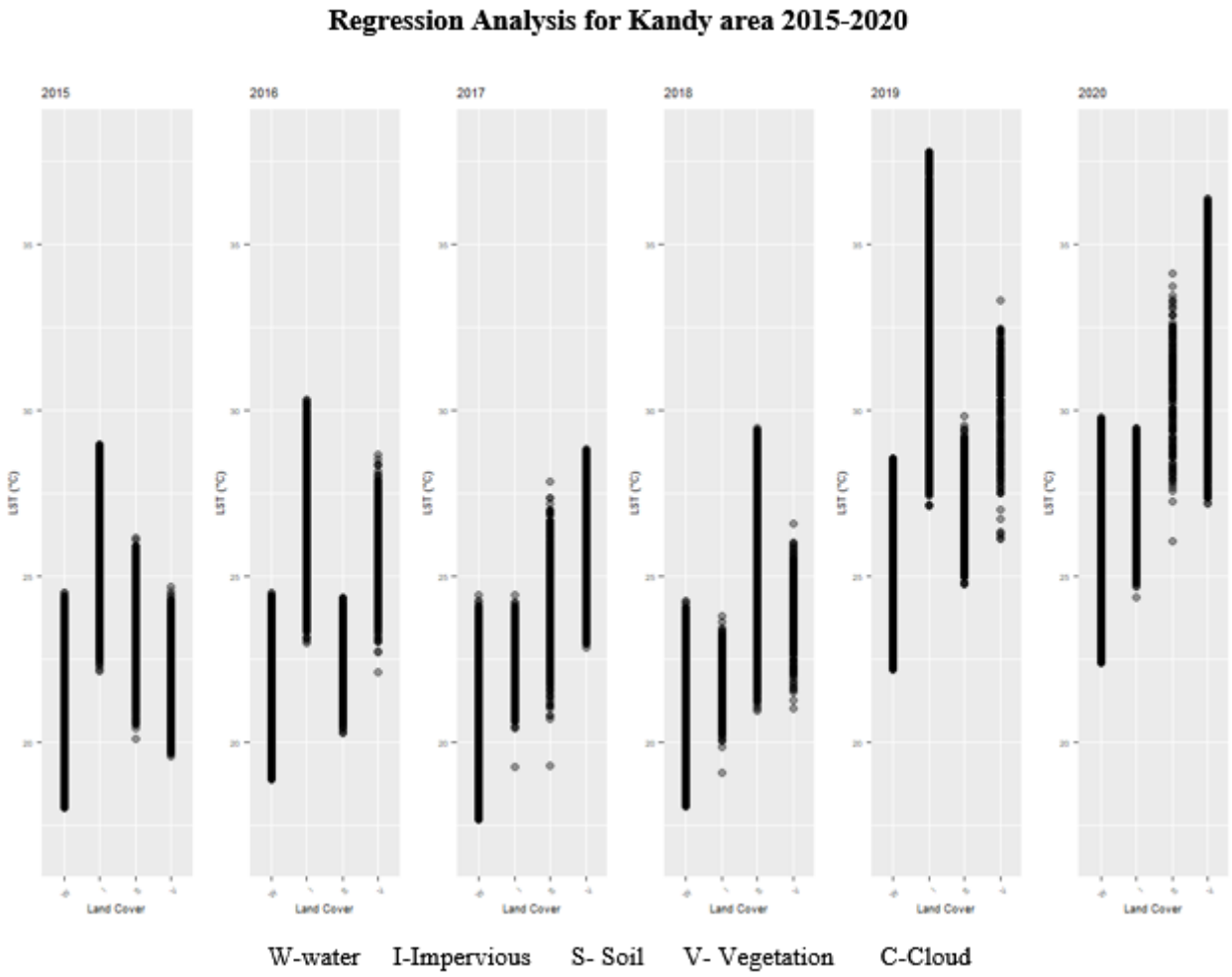

Figure 13. LST map, LC map, highly affected LCs and regression analysis of Kandy area from 2015-2020.

The Belihuloya area has a tropical rainforest climate and is at an elevation of 616 m above the mean sea level. The study area contains a part of the Samanala Wewa reservoir, where the third largest hydropower plant in Sri Lanka was commissioned. Finding cloud-free images for each year was a quite challenging task, and we had to select the images with the minimum amount of cloud cover (less than 10% for the area). According to the LC classification maps, 70% of the area is covered by vegetation and 20% by impervious surfaces. The lowest average LST over the selected main cities was recorded in the Belihuloya area with 21 C. The highest LST and the lowest LST were recorded at 19.780 C in 2017 and 23.880 C in 2019, respectively. According to the model, the highest LST values were obtained due to the soil and impervious LCs, the middle LST values were caused by the water surface, and the lowest LST values were caused by the clouds and vegetation covers. Regression analyses have also proved that the highly affected LCs for the LST changes are similar to the LCs obtained by the model.

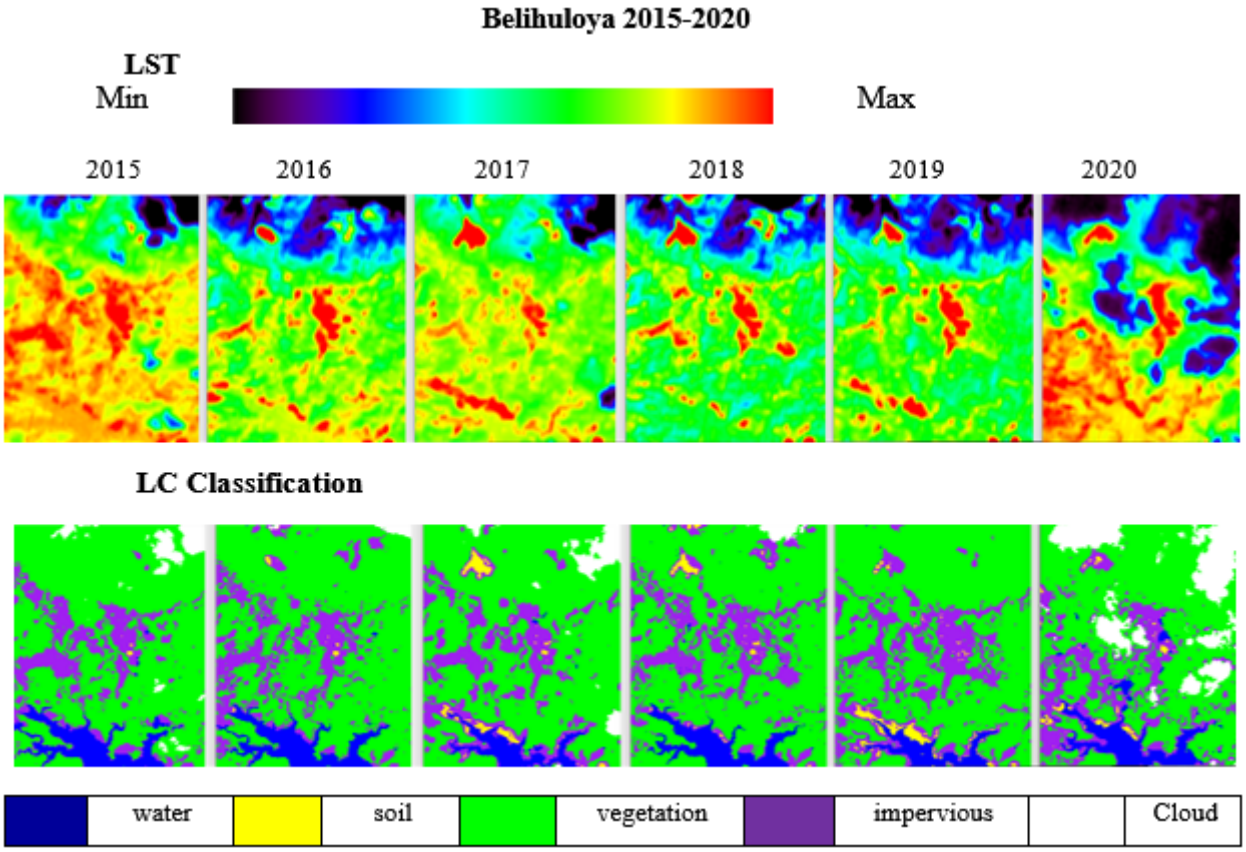

Highly effected LC classes for each LST range for Belihuloya area from 2015 to 2020

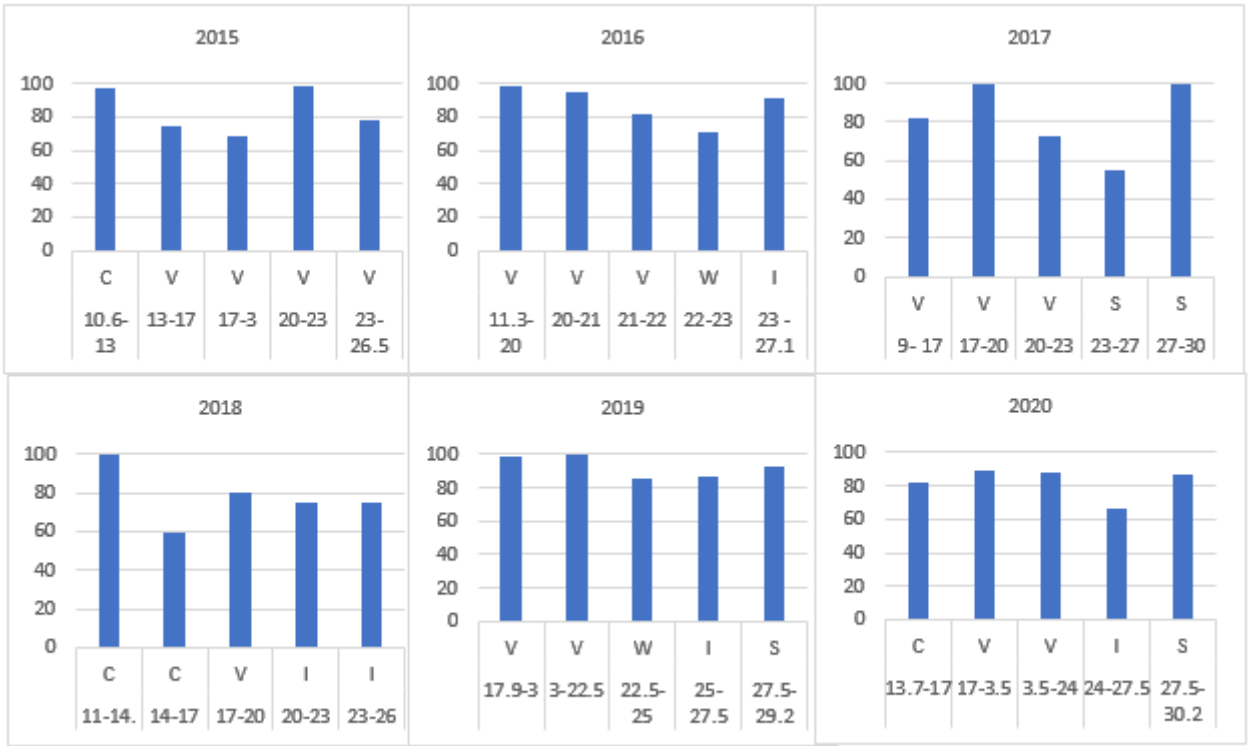

W-water I-Impervious V- Vegetation C- Cloud S-Soil
X – axis -Temperature(^{0}C) Y - axis- Percentage

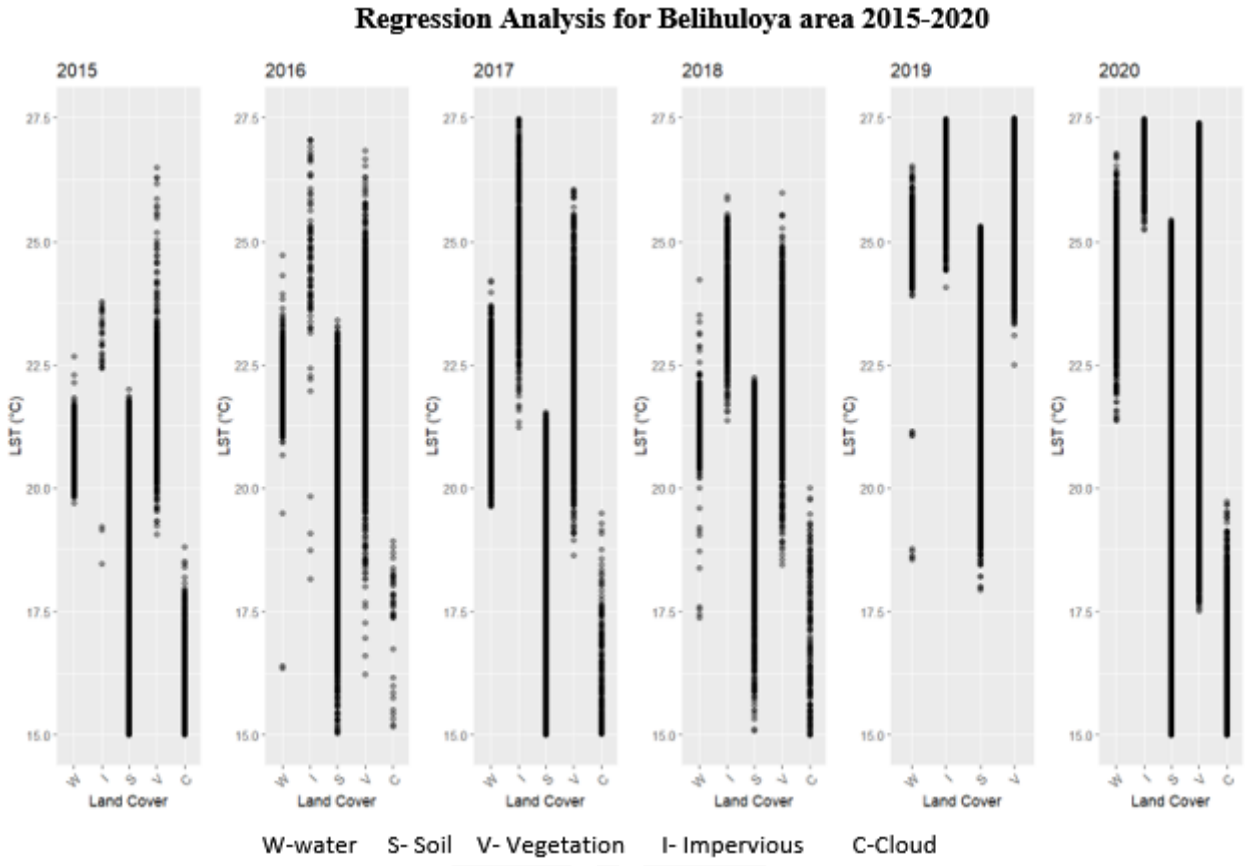

Figure 14. LST map, LC map, highly affected LCs and regression analysis of Belihuloya area from 2015-2020.

Jaffna features a tropical savanna climate, which is recorded as the highest temperature area in Sri Lanka. The selected area for the study is very close to the sea surface and has a flat terrain with around 10 m above the MSL. Both the Bayesian model and the regression analysis have shown that the highest LST has occurred due to the impervious surface in each year, but in 2016, the soil LC has been highly affected by the highest LST. The vegetation cover in 2015 was 38.9%, and in 2020 it was 33.9%. The impervious surface has increased from 47.6% to 57.9% in 2015 and 2020, respectively. The increment of the impervious surface while decreasing the vegetation surface have highly affected the LST change through the years. The highest LST has been recorded in 2018 at 28.01 C and the minimum LST was 23.81 C in 2017. The huge variation between these two consecutive years can be attributed to the misclassification of the 2018 image, which shows a waterbody inside the land area that does not really exist there, and the unexpected vegetation cover increment.

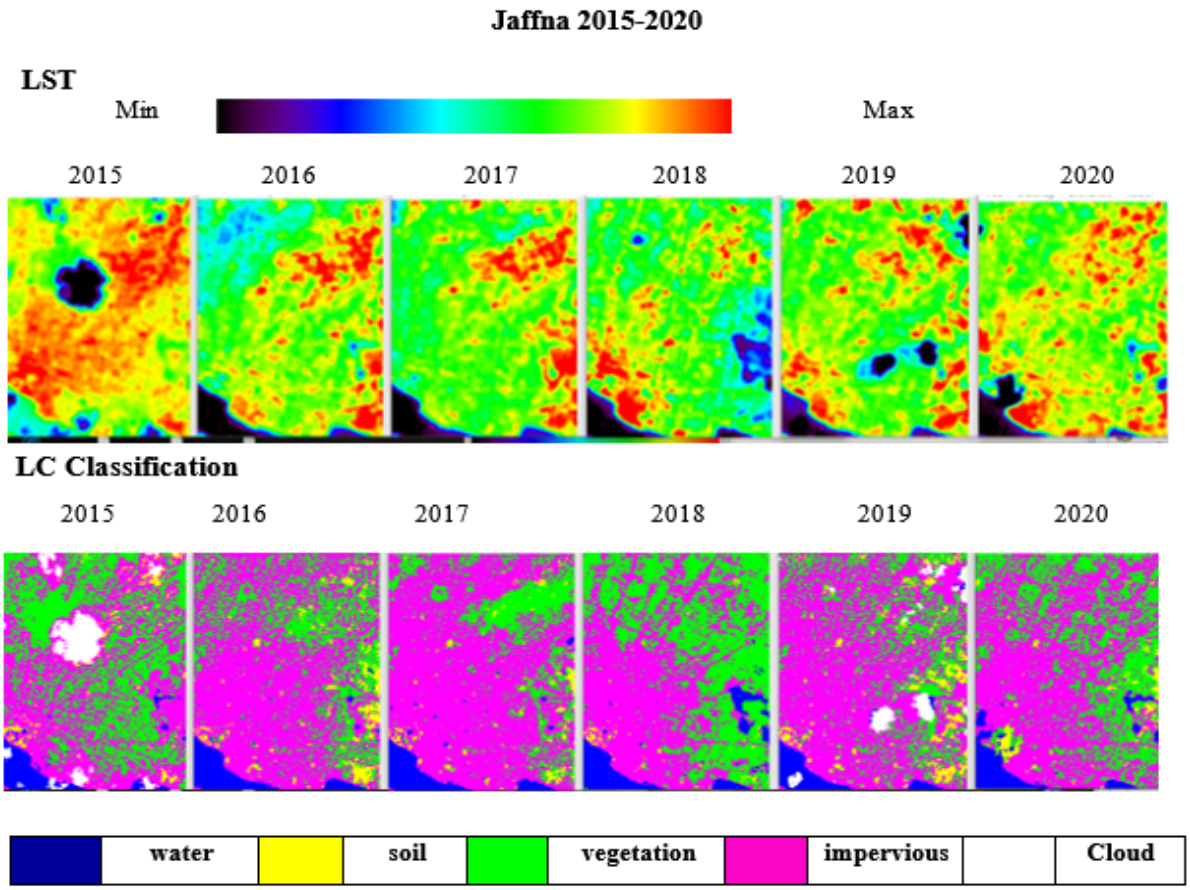

Highly effected LC classes for each LST range for Jaffna area from 2015 to 2020

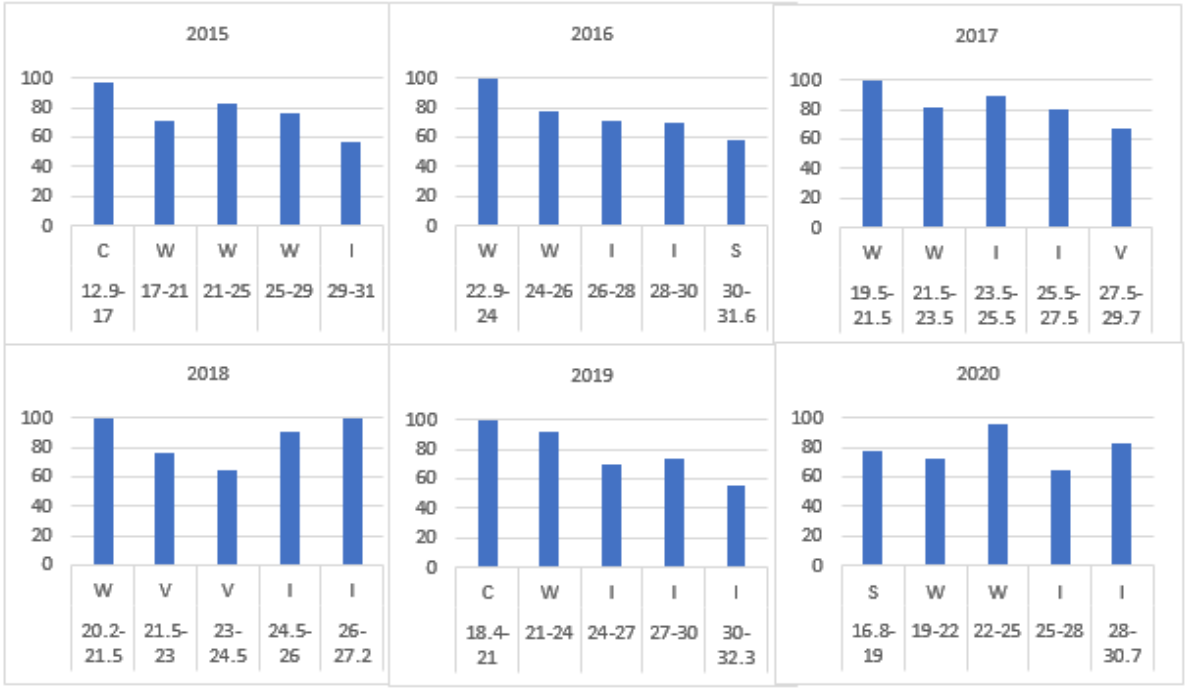

W-water I-Impervious V- Vegetation C- Cloud S-Soil
X Axis-Temperature(^{0}C) Y axis- Percentage

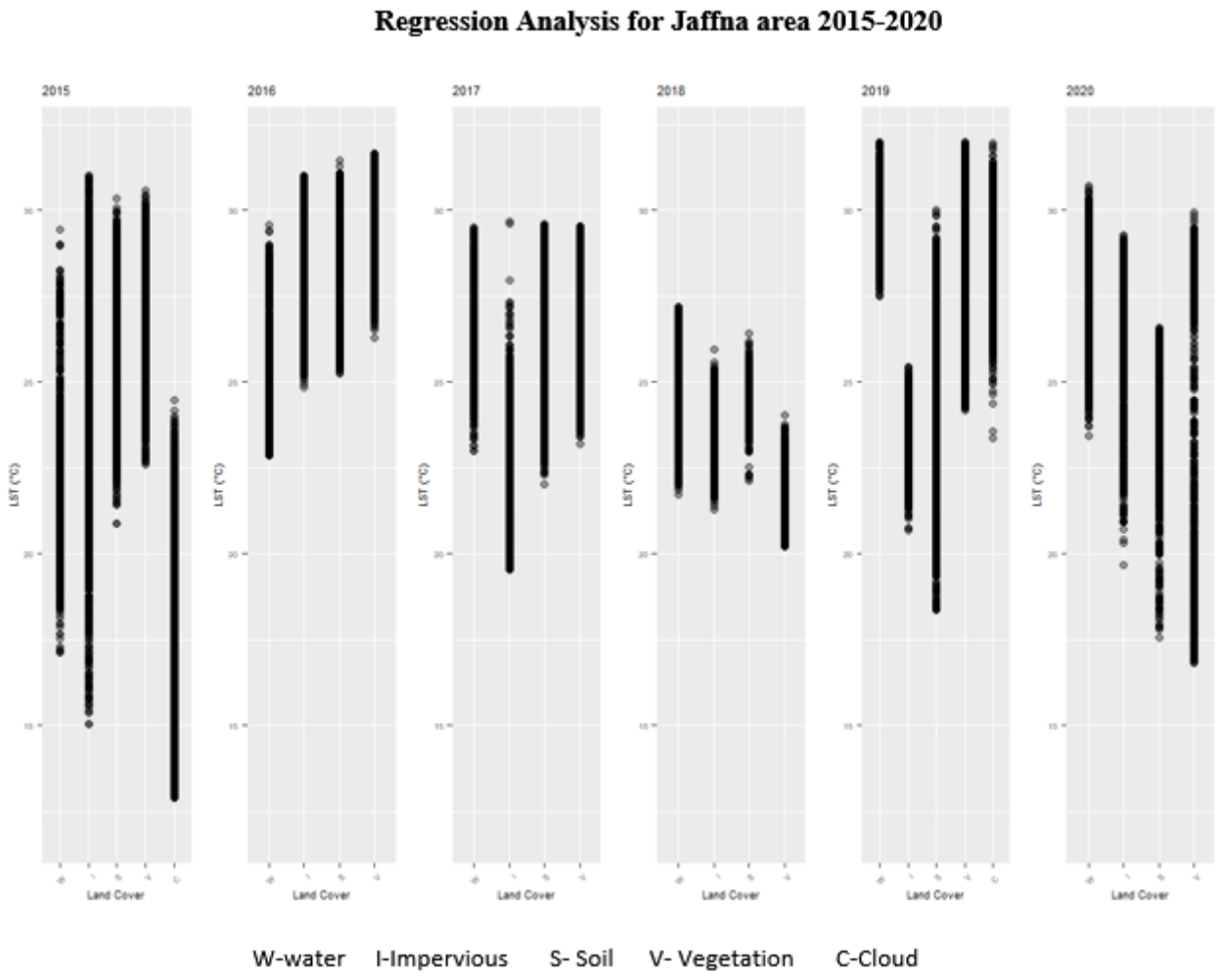

Figure 15. LST map, LC map, highly affected LCs and regression analysis of Jaffna area from 2015-2020.

The LC classification map shows that around 92% of the area is covered with vegetation and 4% is covered with water (Figure 16). The impervious and soil surface had the greatest influence on the LST, according to the e model, while the cloud and vegetation cover had the greatest influence on the lowest LST values. The average LST for the three years 2015, 2017 and 2020 has been recorded at 23.25718 C. The highest and lowest LSTs were obtained in 2017 and 2015, respectively.

Sinharaja is a forest reserve and a biodiversity hotspot in Sri Lanka that has been designated a Biosphere Reserve and World Heritage Site by UNESCO. The average LST was recorded at 21.36 C, where the vegetation cover is around 79% and the water cover is around 7% over the area (Figure 17). The model has shown that the highest LST values are mostly affected by the impervious LC, while vegetation and cloud cover affect the lowest LST values. Regression analysis shows that the middle LST values are caused by the soil and water surfaces, while the impervious surface is highly affected by the highest LST values.

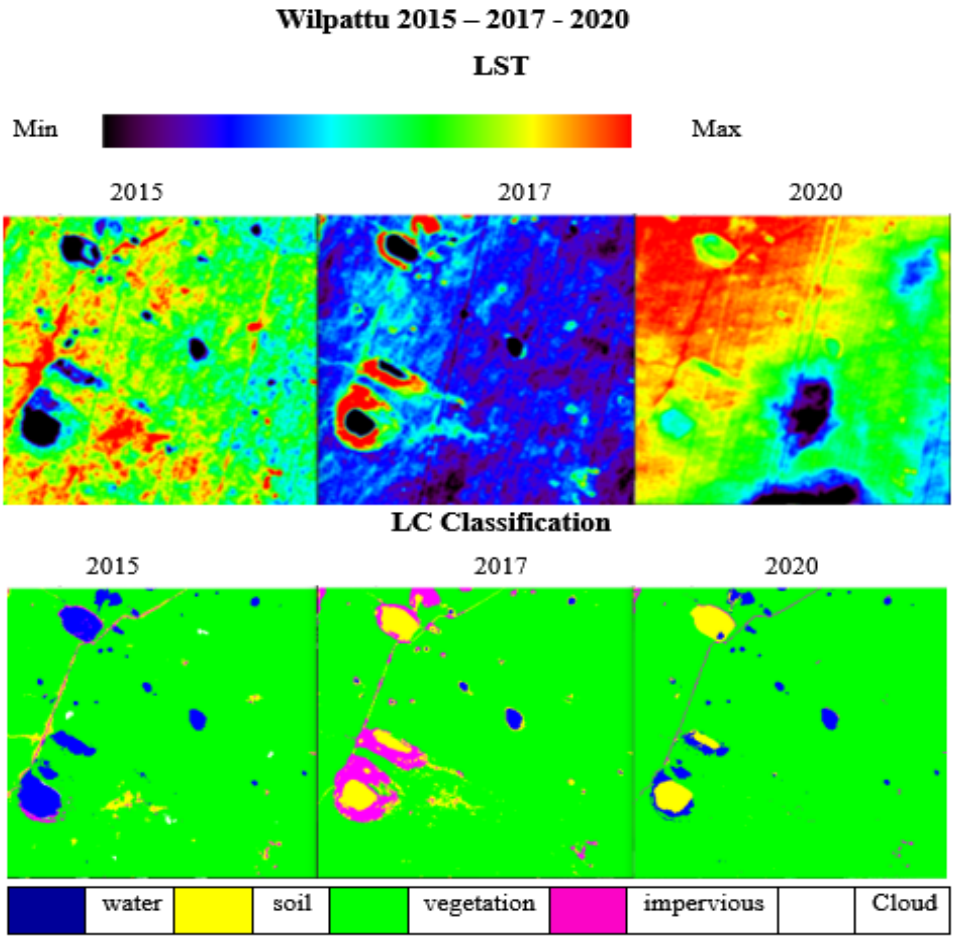

Highly effected LC classes for each LST range for Wilpattu area

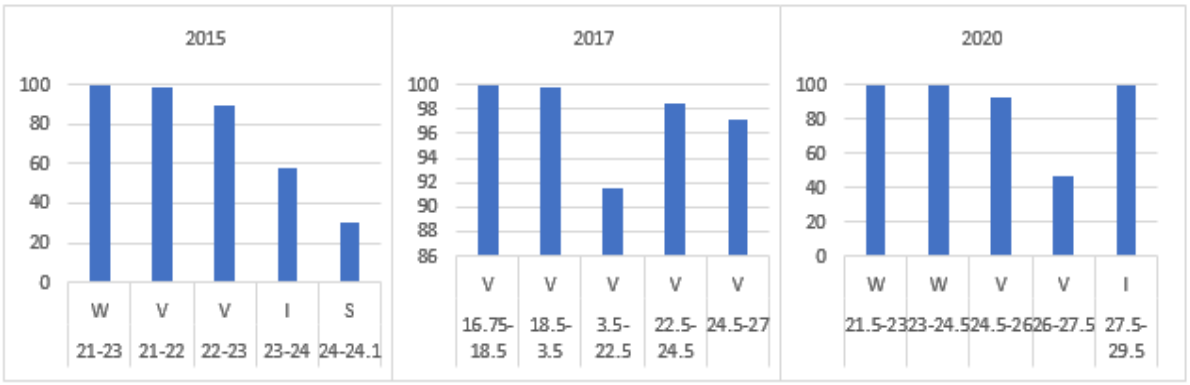

W-water I-Impervious V- Vegetation C- Cloud S-Soil
X Axis-Temperature(^{0}C) Y axis- Percentage

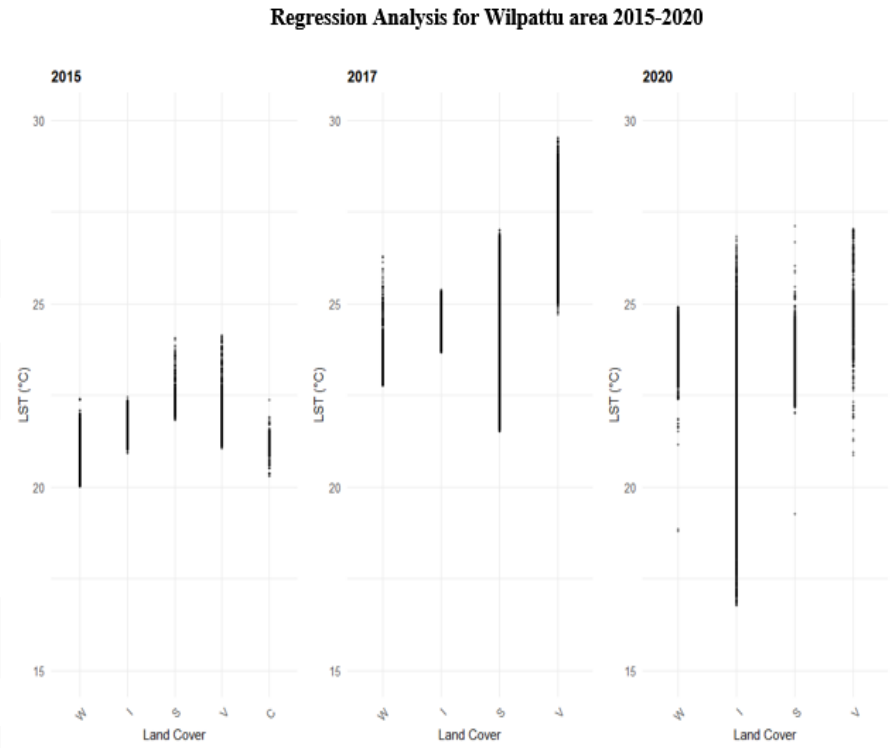

Figure 16. LST map, LC map, highly affected LCs and regression analysis of Wilpattu area from 2015-2020.

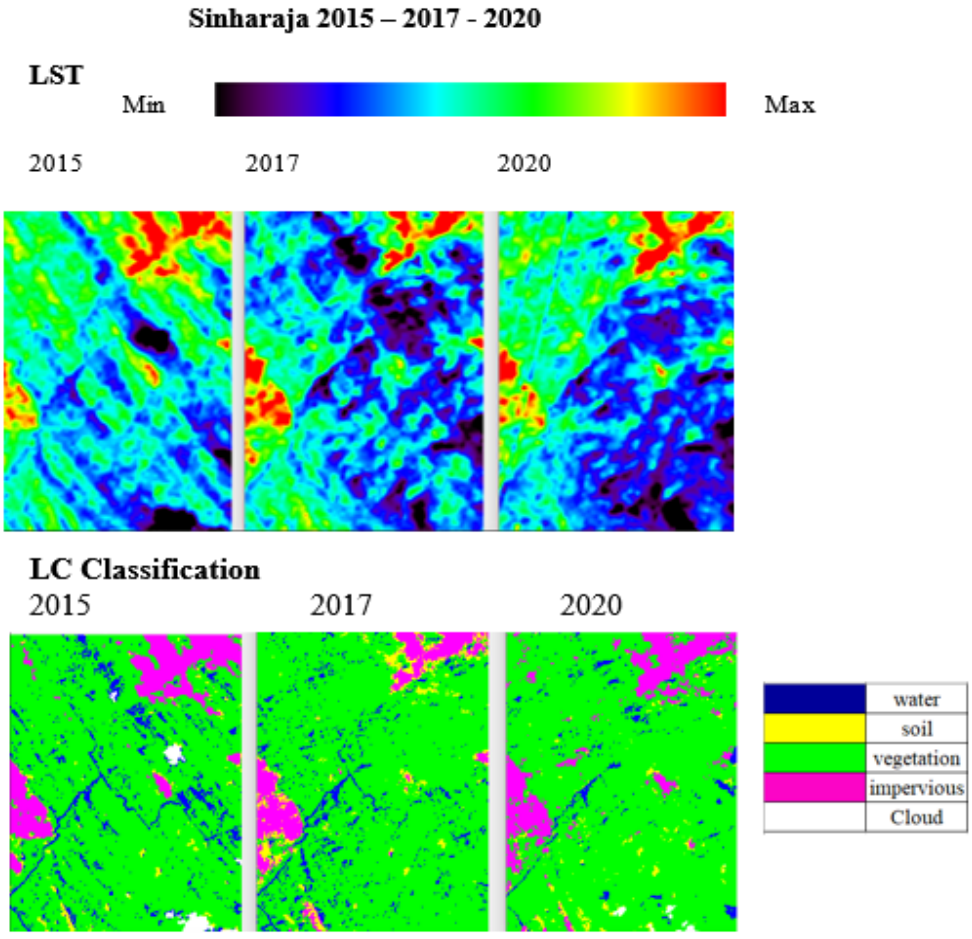

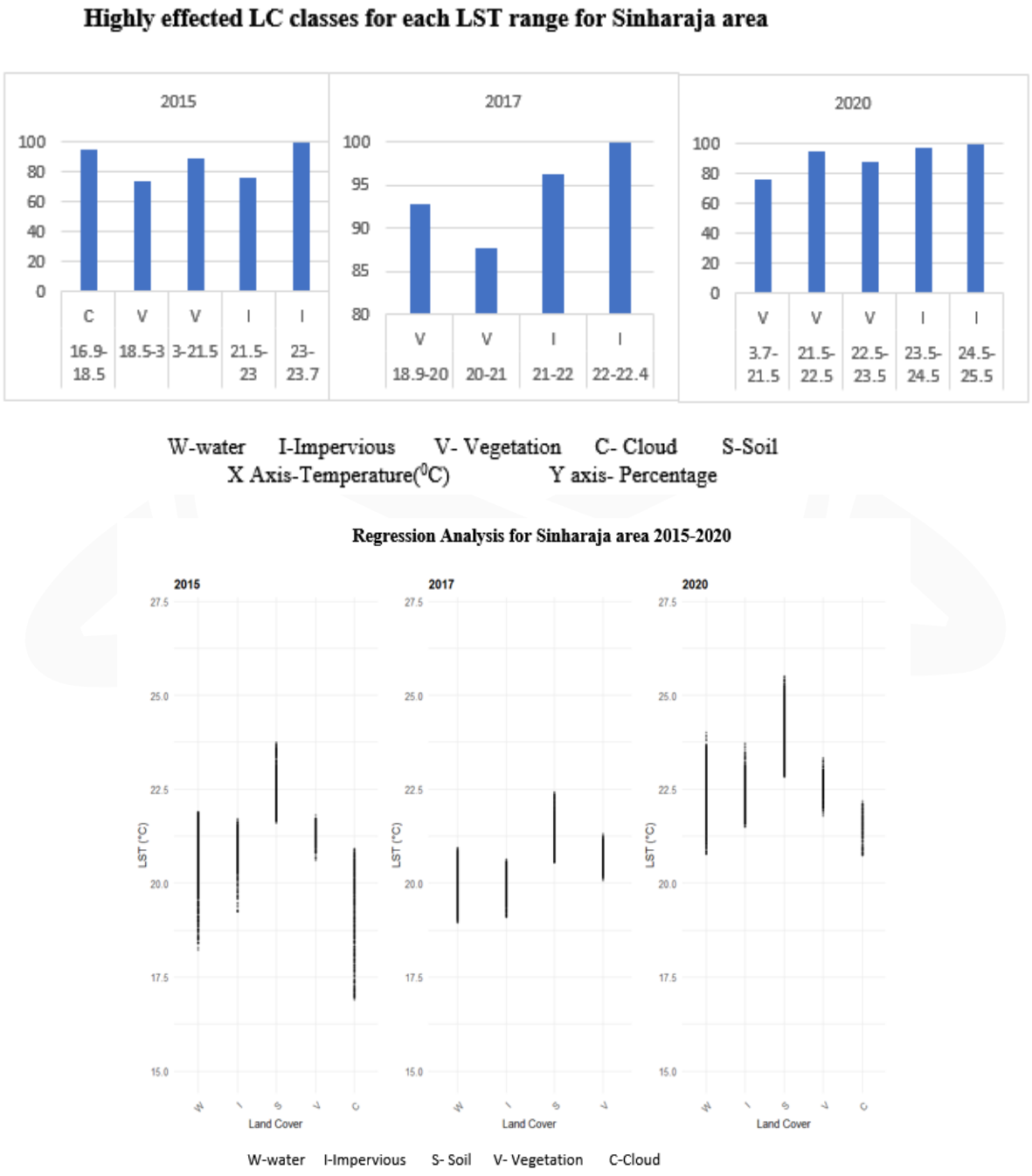

Figure 17. LST map, LC map, highly affected LCs and regression analysis of Sinharaja area from 2015-2020.

The LC maps have shown the vegetation cover at around 68%, soil at 21%, water at 4%, and impervious at 4% over the area (Figure 18). The lowest LST has been recorded in Horton Plains when compared with the other areas in the study, which are 17.93 0C on average. Soil and impervious surfaces have been highly affected for the highest LST values, and vegetation and cloud covers are affected for the lowest LST values. The middle LST values have been affected by water, but not the highly affected LC for those values. Regression analysis also shows that the highest of the LST values are affected by the soil and impervious surface.

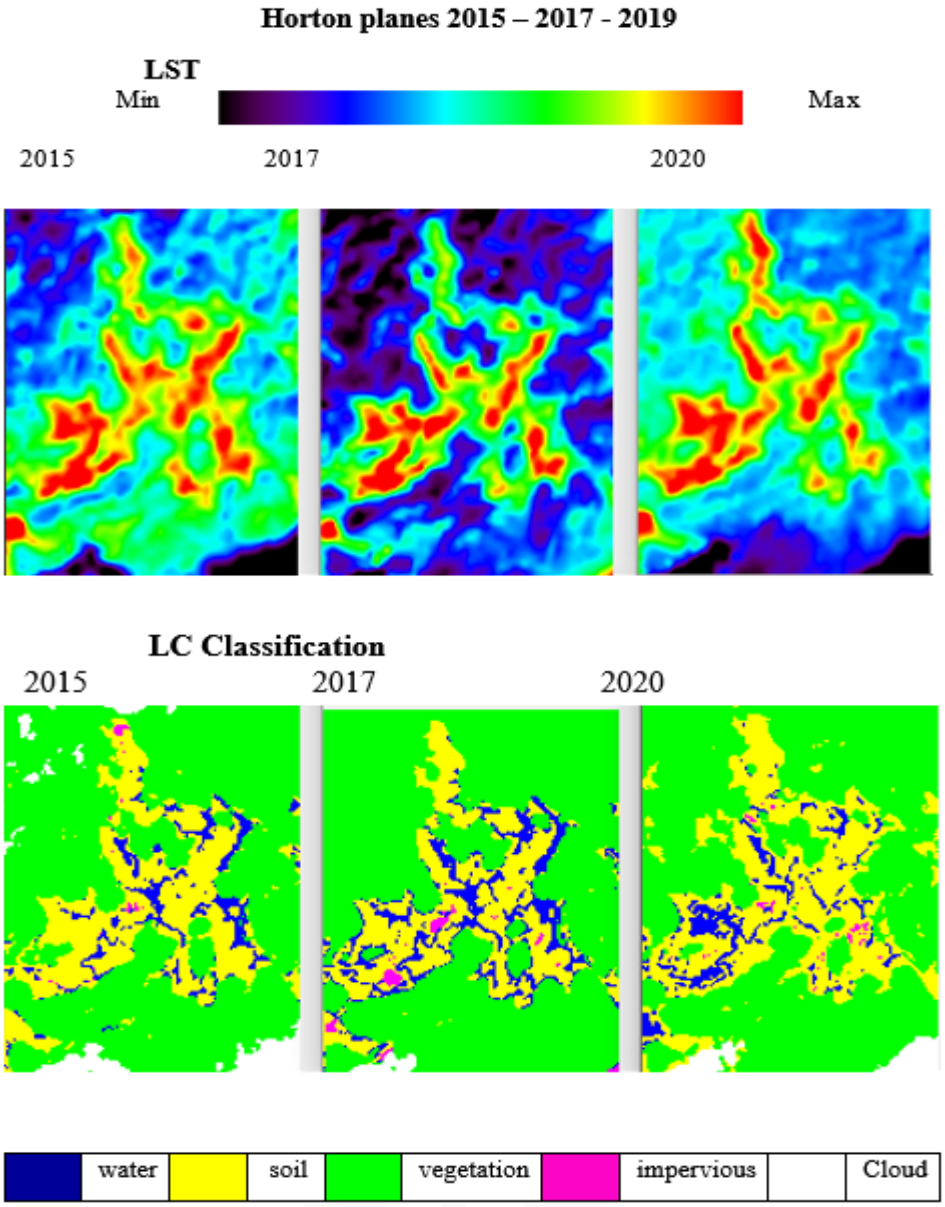

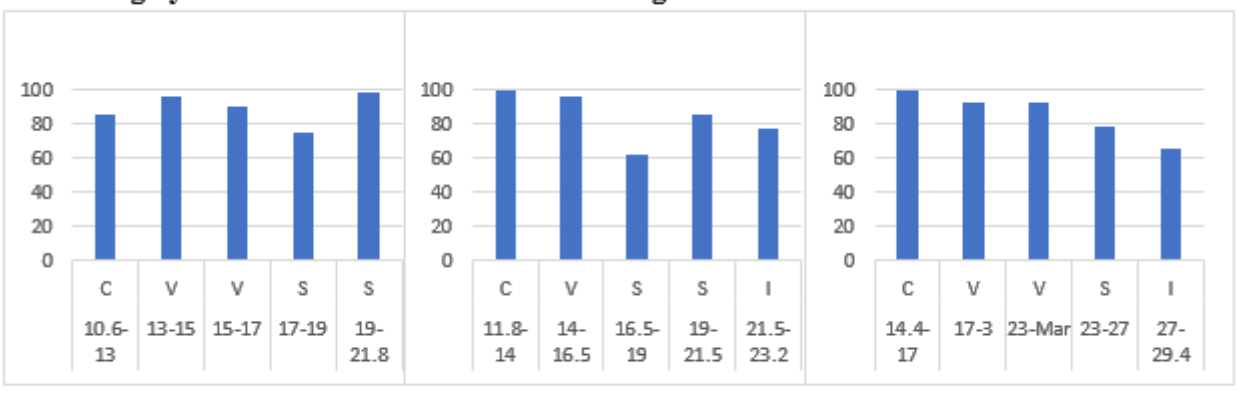

W-water I-Impervious V- Vegetation C- Cloud S-Soil

X Axis-Temperature(^{0}C) Y axis- Percentage

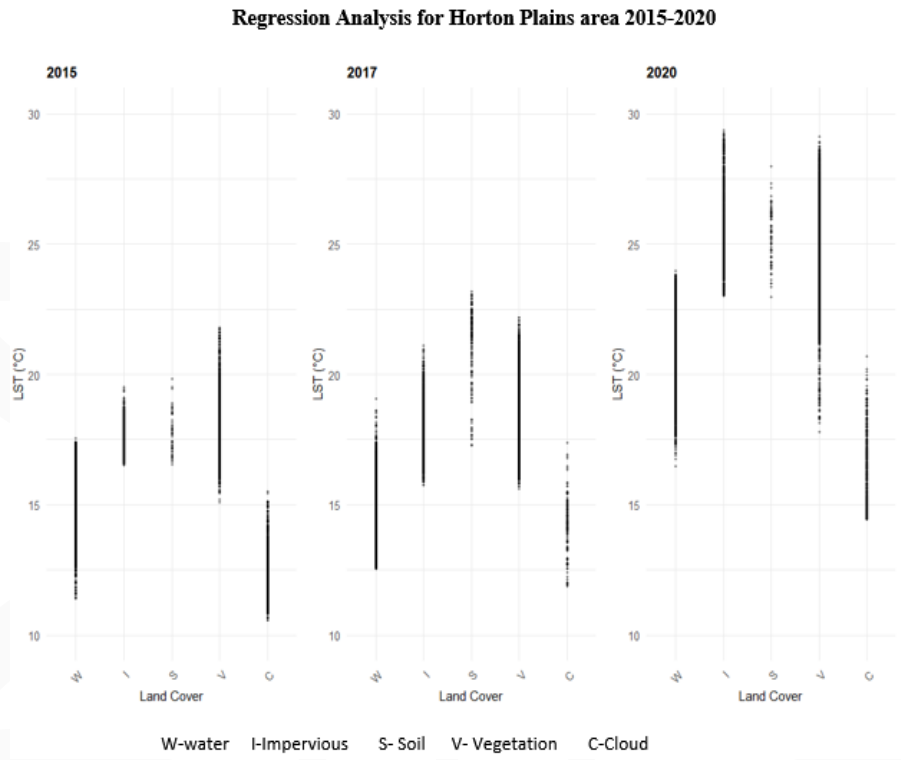

Figure 18. LST map, LC map, highly affected LCs and regression analysis of Horton Plains area from 2015-2020.

DISCUSSION

Incorporating the three parameters LST and LULC into a single Bayesian framework for estimate and prediction was the main goal of this study. The model was built using two sample datasets (8x8 matrix) for LST and LC while taking into consideration a 3x3 moving window. It was based on the Bayes theorem. Finally, model validation was carried out for a well-known area where LC changes happened in two consecutive years as a result of a huge landslide and the area's vegetation cover changing into soil. The association between LST and LC changes for each chosen research area was then investigated using the model using a time series analysis, and the most affected LCs for each temperature class were discovered. There, the LC classification and all of the LST values for each area were determined. The average LST for each region (main cities) in each year is shown in the table below. Ultimately, an average LST for six years was determined. There all the LST values for each area was calculated and LC classification was performed.

The present study developed and applied a Bayesian framework to integrate Land Surface Temperature (LST) and Land Use/Land Cover (LULC) information for estimating and predicting spatial temperature variations. The proposed model successfully incorporated both parameters into a unified probabilistic structure, enabling a more comprehensive understanding of the dynamic relationship

between surface temperature and land cover transitions. Model validation conducted in an area affected by a major landslide further demonstrated the framework's capability to identify temperature changes corresponding to vegetation loss and conversion to bare soil, highlighting the strong dependency of LST on LULC variations.

Following table is showing the average LST for each area (major cities) in each year and finally average LST was calculated for 6 years.

Table 2. Average LST for major cities (Colombo, Kandy, Belihuloya, Ratnapura and Jaffna) from 2015 to 2020.

Area	2015	2016	2017	2018	2019	2020	Average
Kandy	22.4276	23.5284	22.7608	22.6021	28.1680	28.5294	24.6694
Colombo	24.0286	26.2861	24.6971	25.1572	25.5283	27.4104	25.5179
Belihuloya	19.8269	21.0165	19.7809	20.8733	23.8845	20.6441	21.0044
Ratnapura	22.9479	23.9633	23.0841	23.4869	26.0189	25.7265	24.2046
Jaffna	25.6564	27.8384	25.8820	23.8142	28.0135	26.9540	26.3597

Among the major cities in Sri Lanka that were chosen, Belihuloya has the lowest average LST and Jaffna has the highest average LST, with a mean LST of 26.36 0C throughout the years from 2015 to 2020. This pattern aligns with the climatic and land cover characteristics of these regions. Jaffna, located in the dry zone with limited vegetation and higher impervious surface proportions, tends to accumulate more heat, whereas Belihuloya, situated in a highland environment with dense vegetation and greater elevation, promotes cooling through evapotranspiration and canopy shading. These results are consistent with findings by Weng et al. (2004) and Guha et al. (2020), who reported that vegetation cover substantially mitigates LST by enhancing latent heat flux and surface moisture availability.

The temporal analysis further demonstrated a gradual increase in mean LST values from 2015 to 2020 in most cities, suggesting possible urbanization and reduction in vegetation density. This observation aligns with Fu and Weng (2015) and Tan et al. (2020), who highlighted that urban expansion and impervious surface growth significantly contribute to the intensification of surface temperatures and the urban heat island effect. The lowest LST ranges are induced by cloud and vegetation cover when taking into account the heavily affected LC classes for each LST range, whereas water class has a significant impact on the intermediate LST values. Highest LST Values are caused due to the impervious and Soil classes.

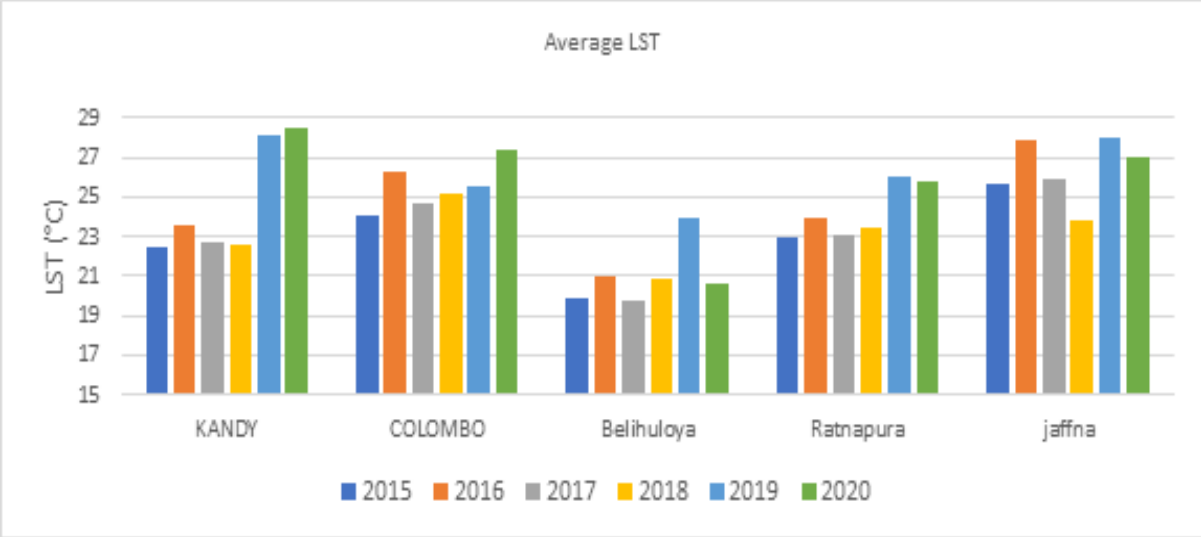

Figure 19. Average LST Graph for major cities (Colombo, Kandy, Belihuloya, Ratnapura and Jaffna) from 2015 to 2020.

Three national parks have been taken into consideration for the study to evaluate how the relationship between LST and LULC when the LCs are substantially vegetated, in addition to the major cities chosen for the study area. The Horton Plains, considered Sri Lanka's most significant watershed, a montane grassland ecosystem, exhibited the lowest average LST (17.93 °C), attributable to its high elevation, extensive vegetation, and minimal anthropogenic influence. The forest canopy rises to a height of 20 meters, and Horton Plain has the lowest impervious LC and the greatest soil LC of the other two forest sections.

potentially due to its mixed vegetation structure and seasonal dry conditions. These findings reinforce the conclusions of Sun et al. (2011) and Purevdorj et al. (2010), who emphasized that denser vegetation cover and soil moisture availability are key determinants of lower LST in forested landscapes.

Regression analyses confirmed a statistically significant relationship between LST and LC variations, particularly highlighting that the soil and impervious classes are dominant contributors to elevated LST values, while vegetation and cloud classes are associated with lower LST. The water class was found to moderate temperature, aligning with intermediate LST ranges. This classification-dependent temperature gradient supports the theoretical understanding of surface emissivity and albedo differences as described by Qin et al. (2001) and Sobrino et al. (2004). The model thus provides a practical basis for quantifying how land conversion processes, such as deforestation or urbanization, modify thermal conditions over time.

Table 3. Average LST for Wilpattu, Sinharaja and hortan planes forest areas in 2015,2017 and 2020.

Area	2015	2017	2020	Average
Wilpattu	21.7801	24.5391	23.4523	23.2572
Sinharaja	21.1882	20.2056	22.6790	21.3576
Hortan Planes	15.8388	15.8044	22.1362	17.9264

The model's outcome probability for each area demonstrates that LST is significantly impacted by LC changes, and that as vegetation cover shifts to other LCs such soil and impervious, LST increases with time. Each location underwent regression analysis to look into the relationship between LST and LC variations. It reveals how soil and impervious classes have a significant impact on the highest LST in forest areas while vegetation and cloud cover have an impact on the lowest LST. The middle LST values are affected by the water class.

While the Bayesian approach demonstrated robustness and interpretability, certain limitations should be acknowledged. The model's reliance on two sample datasets (8 x 8 matrices) and a fixed 3 x 3 moving window may have restricted spatial generalization. Moreover, the LST retrieval accuracy depends on atmospheric correction and emissivity estimation methods (e.g., Barsi et al., 2014; Avdan & Jovanovska, 2016), which could introduce uncertainty in highly heterogeneous surfaces. Future research could extend this framework using finer-resolution data, multi-seasonal imagery, and additional parameters such as NDVI, albedo, and soil moisture to improve prediction accuracy and applicability in complex urban–rural landscapes.

Overall, the findings emphasize that LULC change plays a decisive role in controlling spatial and temporal variations of LST. The integration of both parameters within a Bayesian framework provides a statistically consistent and spatially flexible method for monitoring environmental change. This approach can be applied to assess the thermal impacts of land transformation, aiding in sustainable land management, urban planning, and climate adaptation strategies across Sri Lanka and similar tropical regions.

CONCLUSION

The model can be used to find the conditional probability of each LC class with respect to the LST for each year. The model built in the study could be used to analyze relationships between parameters depending on their frequency distributions.

When comparing the regression analysis with this model, the regression analysis gives the best fitting value considering all the available data without considering the precision of the values from which it calculates the best estimate. Sometimes, there may be outliers. But this model is calculating the exact

conditional probability of each single event within the 3x3 moving window, and it is not affected by all the values in the dataset. The final output is taken with the most probable values, and if there were some outliers within the window, they will be neglected at the final output.

This model was developed only considering the effect of LC changes on LST changes. The LST changes can be affected by some other factors, such as surface soil moisture, urban heat island effect, wind speed, rainfall, and elevation. So, the model should be developed to include the other affecting parameters as well.

The study can be performed by excluding all the cloud cover effects, which have shown a highly negative relationship with LST with techniques such as the CF mask algorithm, the fog stability index, etc.

The image acquisition date may be subjected to LST variations in the trend analysis due to the dry and wet seasons, which can be highly affected by the vegetation cover and water bodies.

REFERENCES

Avdan, U., & Jovanovska, G. (2016). Algorithm for automated mapping of land surface temperature using LANDSAT 8 satellite data. Journal of Sensors, 2016, Article 1480307. https://doi.org/10.1155/2016/1480307

Barsi, J. A., Schott, J. R., Hook, S. J., Raqueno, N. G., Markham, B. L., & Radocinski, R. G. (2014). Landsat-8 thermal infrared sensor (TIRS) vicarious radiometric calibration. Remote Sensing, 6(11), 11607–11626. https://doi.org/10.3390/rs61111607

Das, S. S., & Angadi, D. P. (2021). Assessment of land surface temperature differential and its relationship with urban land use land cover change in Barrackpore Subdivision, West Bengal, India. Remote Sensing Applications: Society and Environment, 24, Article 100647. https://doi.org/10.1016/j.rsase.2021.100647

Fu, P., & Weng, Q. (2015). A time series analysis of urbanization induced land use and LC change and its impact on land surface temperature with Landsat imagery. Remote Sensing, 7(12), 16671–16698. https://doi.org/10.3390/rs71215844

Guha, S., Govil, H., Gill, N., & Dey, A. (2020). Analytical study on the relationship between land surface temperature and land use/land cover indices. Annals of GIS, 26(2), 201–216. https://doi.org/10.1080/19475683.2020.1754291

Markham, B. L., & Barker, J. L. (1985). Spectral characterization of the Landsat Thematic Mapper sensors. International Journal of Remote Sensing, 6(5), 697–716. https://doi.org/10.1080/01431168508948492

Purevdorj, T. S., Tateishi, R., Ishiyama, T., & Honda, Y. (1998). Relationships between percent vegetation cover and vegetation indices. International Journal of Remote Sensing, 19(18), 3519–3535. https://doi.org/10.1080/014311698213795

Qin, Z., Zhang, M., Karnieli, A., & Berliner, P. (2001). Estimation of land surface emissivity for Landsat TM6 data. Remote Sensing of Environment, 76(2), 229–239. https://doi.org/10.1016/S0034-4257(00)00183-1

Rhee, J., Park, S., & Lu, Z. (2014). Relationship between land cover patterns and surface temperature in urban areas. GIScience & Remote Sensing, 51(5), 521–536. https://doi.org/10.1080/15481603.2014.964455

Richards, J. A., & Jia, X. (2005). Remote sensing digital image analysis. Springer-Verlag.

Sobrino, J. A., Jimenez-Munoz, J. C., & Paolini, L. (2004). Land surface emissivity retrieval from different VNIR and TIR sensors. IEEE Transactions on Geoscience and Remote Sensing, 42(2), 316–321. https://doi.org/10.1109/TGRS.2003.821064

Sun, Q., Wu, Z., & Tan, J. (2012). The relationship between land surface temperature and land use/land cover in Guangzhou, China. Environmental Earth Sciences, 65(6), 1687–1694. https://doi.org/10.1007/s12665-011-1145-2

Tan, J., Yu, D., Li, Q., Tan, X., & Zhou, W. (2020). Spatial relationship between land-use/land-cover change and land surface temperature in the Dongting Lake area, China. Scientific Reports, 10(1), Article 9245. https://doi.org/10.1038/s41598-020-66168-6

Weng, Q., Lu, D., & Schubring, J. (2004). Estimation of land surface temperature–vegetation abundance relationship for urban heat island studies. Remote Sensing of Environment, 89(4), 467–483. https://doi.org/10.1016/j.rse.2003.11.005

Xu, H. Q., & Chen, B. Q. (2004). Remote sensing of the urban heat island and its changes in Xiamen City of SE China. Journal of Environmental Sciences, 16(2), 276–281.

ADVANCES IN GEOMATICS

VOLUME 04 • ISSUE 01 • APRIL 2026
e-ISSN: 3023-4980

ORIGINAL ARTICLE

Submission: 29/01/2026
Accepted: 23/04/2026

A REVIEW OF ASSESSING THE IMPACT OF UAV IMAGES FOR LAND COVER ANALYSIS

Srijit SHARMA[1]* Paul NOVAK[1]

[1] University College, University of Denver, CO, USA.

*Corresponding Author: S. Sharma, srijit.sharma@du.edu 0000-0002-1702-8304

ABSTRACT

Land cover maps are an important tool to understand global change and various landscape analyses. Accurate land cover maps are important for their precise application in forest conservation and snow-melt analysis. Satellite images are used as a data source for preparing land cover maps. This review evaluates the use of Unmanned Aerial Vehicles (UAV) as an alternative technology to produce a more accurate land cover map. Throughout the comparative study it is found that higher spatial resolution of the images generally leads to improved overall accuracy of the land cover product. UAV images are found to have the highest overall accuracy compared to other satellite imagery. The review also highlighted that UAV images are not feasible from an economic perspective if the land cover analysis needs to be carried out over a large area. Therefore, it is concluded that UAVs are a good alternative tool for high-precision, local-scale land cover mapping, but satellite imagery is suitable for regional and global monitoring.

Keywords: UAV, Land Cover, Remote Sensing, High Resolution Imagery, Spatial Resolution, Land Cover Classification.

Cited As: Sharma, S., & Novak, P. (2026). A Review of Assessing the Impact of UAV Images for Land Cover Analysis, Advances in Geomatics, 4(1), 35-63. https://doi.org/10.5281/zenodo.20545367

1. INTRODUCTION

Land cover maps are widely considered a tool to monitor global change (Verburg et al. 2011). The land cover map represents the region by forest, wetlands, impervious surfaces, agriculture, water, and other land types. A series of land cover maps over time can be used to monitor the various changes in the land. The changes in land cover are rapid and significantly impact people, the economy, and the environment (National Ocean Service 2024). Such land cover change data have many applications; they are mostly used in climate change modeling, flood modeling, agricultural drought analysis, monitoring environmental changes, and forest change detection (Mora et al. 2014).

Providing a highly accurate land cover map is still a challenge in today's world. So far, satellite images are being used to determine the land cover maps, whose resolution is very low compared to that of UAV images. The most used satellite image, Landsat 7, has a spatial resolution of 30m (Dewitz and USGS 2021), and MODIS imagery has a spatial resolution of 250m, 500m, and 1km according to data type (NASA 2026). The National Land Cover Database (NLCD), created by the US Geological Survey, used Landsat 30m resolution images (Dewitz and USGS 2021). The land cover output from these images may not provide an accurate result of the places where there are drastic changes in land cover types. Many components, such as the amount of glacier melt and change in river pattern, are subject to annual changes between a few inches and a few meters each year (Lindsey 2020). Landsat and MODIS imagery with a pixel spatial resolution of 30m and 250m will not be able to monitor the change of 1-2 meters. The understanding of change in river pattern is important to estimate the flood probability. Understanding the flood probability would help people prepare for land erosion and several other losses. Furthermore, approximately 1.2 trillion tons of ice are melting each year, resulting in rising sea levels (Mooney and Freedman 2021). An accurate land cover map can be used to correctly monitor such ice melt. To address such issues, it is important to determine land cover change using imagery with high spatial resolution.

Unmanned Aerial Vehicles (UAVs) are also capable of monitoring land cover change. The UAV images are captured at low elevation, which provides high-resolution images. Satellite image issues, such as cloud cover or lack of data on the desired date, can be addressed using UAV imagery (Jumaat et al. 2018). In recent days, the UAVs have advanced from the experimental phase to ultra-high resolution mapping, driven by the integration of diverse technologies such as radar, RF sensors, acoustic detectors, and optical imaging systems. The integration of Machine Learning and Artificial Intelligence in this technology has enabled more accurate and reliable systems (Semenyuk et al. 2025). The integration of LiDAR in airborne systems has allowed a new dimension toward the classification feature space, where distinguishing elevated features (such as buildings, trees) from ground features is not possible using a single satellite remote sensing image. Further, LiDAR intensity data collects the backscattered laser energy at the NIR wavelength, which allows for the differentiation of the land cover types. This allows for differentiating man-made features and ground features (Yan et al., 2015). Thus,

this review aims to use high-resolution UAV images over satellite images to provide a more accurate land cover map for forest conservation and various climate change analyses.

The accurate land cover map can be used as a key component to determine the global change (Ge et al. 2007). It can be used to analyze the change in land cover, hydrography, and snowmelt over time. The accurate map will help government bodies to engage in good land planning, determine the snowmelt, understand the pattern of land cover change, and predict the future landscape in a particular area. It helps the nation to control problems like rapid urbanization, uncontrolled development, loss of forest and wildlife, and decreases in agricultural land.

1.1. Problem Statement

While numerous studies have been carried out to study the use of UAVs for land cover analysis, the accuracy of UAVs, a comprehensive synthesis comparing UAV and satellite imagery in terms of their relative accuracy, cost, and scalability is still lacking. Previous studies have focused on generating accuracy assessments for UAVs through confusion matrices or have emphasized their applications. Others have concentrated on single case studies or specific sensor comparisons. Furthermore, the economic trade-off between these technologies has not been evaluated across different project scales.

2. APPROACH

A narrative literature review approach is adopted to understand the impact of UAVs on land cover classification. The existing literature on land cover mapping is highly heterogeneous in terms of classification methods, number of classes, sensor spectral/radiometric properties, and scale of the project. This makes it difficult to conduct a systematic review with standardized criteria and directly comparable quantitative metrics.

Literature was identified through targeted searches using the keywords “landcover”, “Remote Sensing”, “UAV”, and “Accuracy assessment”. Rather than cataloging all available studies, the available journal articles and conference papers were manually screened. Priority was given to papers that include classification accuracy metrics (e.g., overall accuracy, confusion matrices, and kappa index) and also discuss other constraints such as cost, processing time, and project scale, and studies after 2000 were given more preference.

3. LITERATURE REVIEW

3.1 Land Cover, Land Use, and Resolution

The Food and Agriculture Organization (FAO) defines land cover as the observed (bio) physical cover on the earth’s surface (Di Gregorio and Jansen 2000). The different types of physical coverage

could be forest, grassland, cropland, lakes, wetland, etc. Land use is the second important term that is mostly used together with land use. The ocean services describe land cover as the representation of the physical land type, such as forest or open water, whereas land use documents how people are using the land, whether for development, conservation, or mixed uses (National Ocean Service 2024). The report of Environment (ROE) published by the United States Environmental Protection Agency describes land use as the representation of economic and cultural activities such as agricultural, residential, industrial, mining, and recreational uses that are practiced in a given map (US Environmental Protection Agency 2008).

Land cover maps can be used for various purposes such as environmental monitoring, land management, and policy making. Land cover datasets are a tool for decision-making and shaping policies worldwide (Kovacic 2025). The land cover data and maps are also used by coastal managers to understand the current landscape. The land cover map helps coastal managers to assess urban growth, model water quality issues, predict and assess impacts from floods and surges, track wetland losses, determine impacts of sea level rise, prioritize areas for conservation, and compare the land cover changes (National Ocean Service 2024).

Resolution refers to the smallest size at which an object or detail can be represented in an image. Higher-resolution images have a smaller pixel size, which provides more details, while lower-resolution images have a larger pixel size, which provides fewer details (Setyawan, 2019). There are four types of resolutions for satellite imagery (Navulur 2006):

i. Spatial resolution: It represents the length of the side of the pixel. The greater spatial resolution allows precise identification of features. The use of spatial resolution can be considered depending on the application. For large area change detection, it is economical to use medium resolution imagery, and for planimetric applications, it is recommended to use imagery with the highest possible resolution that can be used to extract various features such as pavements, roads, etc.

ii. Spectral resolution: This represents the number of spectral bands of the given sensor. For most GIS applications where images are primarily used as a backdrop, three-band natural color imagery in RGB format is commonly used. For extracting information such as impervious surfaces and vegetation classification, visible and near-infrared (VNIR) bands are utilized, whereas applications like mineral exploration and forest species classification rely on multispectral or hyperspectral data.

iii. Radiometric resolution: This represents the number of gray levels that can be recorded for a given pixel. The higher radiometric resolution gives better discrimination of variations in reflectance.

iv. Temporal resolution: This represents the time frequency at which the sensors cover the same area of interest (AOI). Issues such as cloud cover can be minimized by using satellites with higher temporal resolution (Navulur 2006).

Table 1 briefly describes the representation and characteristics of the four types of resolutions discussed.

Table 1. Types of Resolution for satellite imagery (Navulur 2006).

Resolution Type	Representation	Characteristics
Spatial	Length of the side of a pixel	Spatial Resolution is defined by Ground Sampling Distance (GSD). Commonly, Low resolution is defined as pixels with a GSD of 30 m or greater resolution, medium resolution is GSD in the range of 2.0–30 m, high resolution is GSD 0.5–2.0m, and very high resolution is pixel sizes < 0.5m GSD. The smaller the pixels, the more details are visible.
Spectral	Number of bands of the given sensor	Multispectral sensors have fewer than ten bands, superspectral sensors have bands greater than ten, and hyperspectral sensors usually have bands in hundreds. With higher spectral resolution, one can extract better information, such as impervious surfaces, vegetation classification, etc.
Radiometric	Number of gray levels that can be recorded for a given pixel	A radiometric resolution of 8 bit radiometric resolution can capture DN values ranging from 0 to 255. The value can be calculated using the equation $N = 2^R$, where N is the range, and R is the radiometric depth.
Temporal	Time frequency at which the sensors cover the same AOI.	The sensor that visits the AOI every day has higher temporal resolution than the sensor that revisits the AOI monthly. Temporal resolution is important for change detection.

3.2 History of Land Cover Maps

The era of land cover mapping started in the early 1970s. Civil space-based remote sensing came into the age in the early 1970s. The 1970s are the foundational period for space-based land cover mapping. The 1970s era was influenced by two major events of the mid-1960s. First, William Pecora (Director of the US Geological Survey) proposed an idea about a civilian remote sensing satellite program to collect information about the natural resources of the Earth. Second, NASA conducted a series of remote sensing investigations using an image-capturing infrastructure mounted on an aircraft. These two events resulted in the launch of NASA's Earth Resources Technology Satellite in 1972, which is now known as Landsat. Later, a draft 'A Land Use and Land Cover Classification System for use with remote sensor data' was published in 1976, which provided a classification legend that defined land use and land cover categories to be derived from remote sensing images (Anderson et al. 1976). The

launch of Landsat and the framework for land cover mapping today serve as a framework for land cover mapping using satellite images, even though it was a manual approach rather than a computer-assisted method (Giri 2012).

The 1980s were the point where the rapid growth of land cover mapping methods and projects happened. Three major factors influenced this decade in land cover mapping. First, computer-assisted methods were developed for land cover mapping. Second, Landsat data quality was improved with the Thematic Mapper instrument, and Landsat was commercialized, which made a heavy impact on the land cover initiative. The spatial details obtained from Landsat needed some improvement to gain efficiencies through the digital imagery. Anderson from USGS recognized this need and led his team in the initial research of land cover classification. He tried to provide an accurate land cover map with Landsat data and developed an automated classification method (Anderson et al. 1976). In the late 1970s and early 1980s, many land cover mapping programs were initiated across the United States in Arizona, Kansas, Nebraska, North Dakota, South Dakota, and Texas. The land cover mapping again boosted in 1982 when Landsat launched a new sensor called 'Thematic Mapper (TM)', which improved the accuracy of the data with spatial and multispectral capabilities. The Landsat resolution was improved from 79 meters to 30 meters (Giri 2012).

The 1990's is when the start of national to global land cover mapping happened. The Advanced Very High-Resolution Radiometer (AVHRR) based land cover project was started in this global land cover mapping era. The 1990s can also be called the end of the commercial Landsat era, which contributed to the growth of national-scale Landsat-based land cover mapping and allowed investment in land cover programs. The use of the time-series dataset and derived seasonal metrics excluded the limited coarse-resolution imagery. The seamless dataset was available, which reduced the problem of scene boundaries. The use of ancillary data and stratification helped increase classification accuracy. The data were available for new satellite missions like the India Remote Sensing satellite, which increased the innovation in the land cover mapping (Giri 2012).

The first decade of the twenty-first century was when operational mapping became more mature, and researchers' emphasis on land cover change studies increased. The land cover monitoring matured in this period with the launch of NASA Terra and Aqua Terra with the Moderate Resolution Imaging Spectroradiometer (MODIS). The accuracy assessment was less common, but the accuracy standards for land cover products were established and matured significantly. Most land cover practices started to include validation as a standard practice (Giri 2012).

During the second decade of the twenty-first century, the European Space Agency's (ESA) Copernicus program introduced the launch of Sentinel Satellites. The first of the Sentinel series, Sentinel-1A, was launched on 3 April 2014, followed by Sentinel-1B on 25 April 2016. For land monitoring, Sentinel-2A was launched on 23 June 2015, followed by Sentinel-2B on 7 March 2017. Sentinel-2 is a

polar-orbiting, multispectral high-resolution imagery at spatial resolutions from 10m to 60m across 13 spectral bands, with its core applications including land cover classification and forest monitoring. On 5 September 2024, Sentinel-2C was launched into orbit to ensure the continuous provision of high-resolution data from the mission (ESA, n.d.).

Similarly, the use of Very High Resolution (VHR) satellite imagery has significantly advanced in land cover mapping. DigitalGlobe's QuickBird was launched on 18 October 2001, which was the first commercial satellite to offer sub-meter imagery, collecting data at 0.65m resolution. The QuickBird satellite was switched off on January 27, 2015, after completing 70,000 trips around the globe and capturing around 636 million sq km of high-resolution imagery. WorldView-1 was launched on 18 September 2007, with a resolution of 0.50 m and has a daily collection capacity of up to 750,000 square kilometres (Satellite Imaging Corporation, n.d.).

Under the French-Italian ORFEO programme, Pléiades-1A was launched on 17 December 2011, followed by Pléiades-1B on 2 December 2012, both operating at 0.5 m resolution with daily revisit capability over any point on Earth. (CNES, 2025) Concerning the history, it is assumed that the land cover technology will lead towards innovation in the future, and the remote sensing satellite imagery will be much cheaper (Giri 2012).

3.3 Accuracy in the land cover map

Unlike the satellite image, the land cover map is not the perfect representation of reality. In remote sensing, the term accuracy means the degree of correctness of the map. No map is 100% perfect, and to determine the degree of correctness, it is necessary to conduct an accuracy assessment. The result of the accuracy assessment gives the overall accuracy of the whole map as well as the accuracy of each class in the map (Horning 2004). There is no accepted standard method of accuracy assessment. However, the confusion matrix is the most popular method for accuracy assessment. The confusion matrix will determine the confusion between each class within the map. In the confusion matrix, commonly, the data is represented in percentage cases, as it is easy to interpret. The confusion matrix provides a summary of two types of thematic error present: omission error (producer's accuracy) and commission error (consumer's accuracy). Producer's accuracy determines how well the reference pixels from the ground are classified in the map, and consumer's accuracy determines how well the classified category in the map represents the ground. However, the non-thematic error is not represented in the confusion matrix, which may be large and could have a larger effect. The problems, like mixed pixels and misregistration of the data set, may not be incorporated (Foody 2002).

Liang et al. (2019) studied the accuracy evaluation and consistency analysis of different land cover products. The study was conducted in the Arctic Region. Land cover products from four different sensors - Climate Change Initiative Land Cover (CCI-LC), GlobeLand30, Global Land Cover by the National Mapping Organization (GLCNMO), and Moderate Resolution Imaging Spectroradiometer

(MODIS) were utilized. The land cover product was refined to nine different classes: Shrub, sparse vegetation, Wetland, Snow/Ice, Trees, Herbaceous, Cropland, Artificial Surface, and Water. For accuracy assessment, validation point data were collected, and a confusion matrix was prepared. The accuracy assessment proved CCI-LC to be the most accurate product with an overall accuracy of 63.5%. GlobeLand30 and GLCNMO were found to have an overall accuracy of 62.2% and 48.8%, respectively. The MODIS land cover product was found to have the lowest overall accuracy of 29.5%. The spatial resolution of Globe30 is highest at 30m, followed by CCI-LC and MODIS with 300m for both. GLCNMO has the lowest resolution of 1 km. CCI-LC was found to have the highest overall accuracy and has good accuracy for the forest, shrubs, sparse vegetation, snow/ice, and water bodies. GlobeLand30 and CCI-LC have a good output for the classification of the shrub. MODIS and GLCNMO product having a very low resolution are omitted for classification in the Arctic region. CCI-LC and GLCNMO have comparatively better accuracy, but the author believes the current land cover products are not ideal in terms of accuracy for classification studies in the Arctic Region (Liang et al. 2019). The comparison of accuracy of the selected land cover products in Arctic region is presented in Table 2, where CCI-LC with resolution of 300m demonstrates the highest overall accuracy among the datasets.

Table 2. Land Cover Products accuracy in the Arctic Region.

Study	Objective	Sensors	Resolution	Accuracy	Conclusion
Liang et al. (2019)	Accuracy evaluation and consistency analysis of different land cover products in the Arctic Region	CCI-LC	300m	63.5%	Land cover products are not ideal in terms of accuracy for classification studies in the Arctic Region
		GlobeLand30	30m	62.2 %	
		GLCNMO	1 km	48.8%	
		MODIS	300m	29.5%	

3.4 Impact of Spatial Resolution on Map Accuracy

The spatial resolution of the image is a basic characteristic of a remote sensing image, which makes a heavy impact on the accuracy of the image classification. The improper selection of spatial resolution may lead to an ambiguous interpretation of the products. Land use, land cover classification using a single sensor may result in limitations like low classification accuracy and adaptability. Mishra et al. (2016) evaluated the land use, land cover classification accuracy using 3 different sensors. LISS IV with 5.8 meters, Landsat 8 with 30 meters, and AWiFS with 56 meters spatial resolution were used for

the study. Images were imported to ENVI (remote sensing image processing software) for classification and were classified into seven different classes as Agriculture land, Dense vegetation, Sparse vegetation, fallow land, built-up, water bodies, and sand. For the accuracy assessment, 438 sample points with 30-43 points for the individual class were checked. The overall accuracy of 83.28%, 77.93%, and 74.61% was determined for LISS IV, Landsat 8, and AWiFS sensors. The result indicates a slight increase in overall accuracy with an increase in spatial resolution from 56m to 5.8m. The study concludes that better spatial resolution reduces mixed pixel problems, which helps in providing a greater extent of information from land use/land cover data sets. Thus, the increase in spatial resolution results in an increase in the overall accuracy of the land use/land cover map (Mishra et al. 2016).

Fisher et al. (2018) project has researched to determine the impact of satellite imagery resolution on land use classification to model the water quality. The objective of their study were:

To assess the influence of the spatial resolution of satellite images on the accuracy of the land cover classification and the estimated sediment load at the plank intake.

To evaluate the technical and economic trade-offs associated with using two images of different resolutions.

DigitalGlobe's Quickbird and Worldview 2 satellites of spatial resolution 0.6m and 0.5m, respectively, and Landsat of 30m were considered for the study. The DigitalGlobe images were resampled to 1m, as the DEM used for the study was 1 m. Land use classification was conducted via ArcGIS feature analyst and on the total suspended solids (TSS) load estimates from the Soil and Water Assessment Tool (SWAT). The study was conducted for the Camboriu watershed in southeastern Brazil. The land use accuracy from DigitalGlobe with 1m spatial resolution was determined 82.3%, and for Landsat data with 30m spatial resolution was calculated as 75.1%. For annual and peak TSS load in the whole study area, however, Landsat data with 30m resolution predicted better only in the sub-watershed. (Fisher et al. 2018)

There have been lots of investments to obtain the accuracy of land cover datasets. However, the accuracy may not hold the same importance when the products are on different scales. It is important to understand the relationship between map error, the scale of observation, and scene spatial structure to understand the scaling issues and their implication of accuracy in land cover data. Moody and Woodcock (1994) have tried to develop an understanding of the factor of scale in errors in the estimation of land cover proportions for the implications of the global land cover dataset. The authors tried to develop an understanding of the size and spatial pattern of vegetation classes, which influenced errors in estimating cover type proportions as the classified scene was progressively aggregated to coarser resolutions. The purpose of the study is to understand the relationship of the proportional error to scale or spatial resolution. The study focuses on the use of land cover data at various scales using remotely sensed data, and the subsequent use or further aggregation of the datasets. The study area was

in the western part of the Plumas National Forest in the Sierra Nevada, California. The images were collected from Landsat Thematic Mapper imagery, which is of 30m resolution, and an unsupervised image classification approach was used to produce a land cover map. The research deals with vegetation classes, so the land cover classes for the study include barren/grass, brush, hardwood, meadow, conifer, and water. The 30m resolution per pixel land cover map of the Plumas National Forest study was used as a base data to compare it with coarser resolution maps. Resolutions of 30, 90, 150, 240, 510, 1020, 3000, and 6000 meters were considered for the study. The 240-, 510-, and 1020- meter resolution is roughly close to the MODIS spatial resolution. Each resolution of interest was created using a polygon grid as a sampling frame. It was seen that the proportional errors in a forested area (such as conifer class) increased as the resolution exceeded 90 meters. Classes that are characterized by highly clumped distribution but small in size decreased in size as the resolution was increased. Small classes with fragmented units disappeared as they were dominated by large cover types through the aggregation procedure. The author considers that these errors may pose difficulties for the use of land cover products derived from coarse resolution sensors such as MODIS (Moody and Woodcock 1994). Table 3 summarizes the studies from Mishra et al. (2016), Fisher et al. (2018) and Woody and Woodcock (1994), highlighting imagery with higher spatial resolution has more accuracy.

Table 3. Impact of spatial resolution on map accuracy.

Study	Land Cover Classes	Imagery Source (Resolution)	Accuracy Result	Conclusion
Mishra et al. (2016)	7 classes (Agri, Dense/Sparse Veg, Fallow, Build-up, Water, Sand)	LISS IV (5.8m)	83.28%	Higher resolution reduces the "mixed pixel" problem, leading to better accuracy and more detailed information.
		Landsat 8 (30m)	77.93%	
		AWiFS (56m)	74.61%	
Fisher et al. (2018)	Not specified (used for TSS Load modeling)	DigitalGlobe - QuickBird (0.6m) and WorldView 2 (0.5m) Resampled to 1m	82.3%	High resolution is more accurate
		Landsat (30m)	75.1%	

Moody & Woodcock (1994)	6 classes (Barren/Grass, Brush, Hardwood, Meadow, Conifer, Water)	Landsat, Coarser Resolution Land Cover Map of Plumas National Forest (30m to 6000m aggregated)	Errors increased significantly once the resolution exceeded 90m.	Coarse resolution causes small or fragmented land classes to "disappear" as they are absorbed by larger, dominant cover types.

3.5 Operational and Technical aspects of Satellite Image and UAV

In Fisher et al. (2018)'s research, the authors determined that the cost of using 1m high-resolution data from DigitalGlobe is $6969, whereas there is no cost for a 30m resolution Landsat image. Using high-resolution images takes extra storage and a longer processing time. The author evaluates that it takes 4 times longer to process for land-use classification using the same hardware device. In terms of technical and economic tradeoff, it is beneficial to work on low-resolution images rather than high-resolution images (Fisher et al. 2018).

Foster et al. (2024) and team discuss the cost-effectiveness of remote sensing technology for spruce budworm monitoring in Maine, USA. The study analysed comparing remote sensing data and ground sampling techniques, with an integrated monitoring approach that combines remote sensing change detection with field sampling. For the remote sensing technique, Sentinel-2 imagery, PlanetScope imagery, and UAV images were taken. The study presented that Sentinel 2 is the most cost-effective option, with costs ranging from US $33 to $63 per sq km to accomplish the task. PlanetScope ranged from US $ 77 to US $ 241 per sq km, and UAV imagery had a great variation from US $9,220 to US $58,481 per sq km. The integrated approach ranges from $144 to $213. The integrated monitoring approach proposed in this study costs range from US $144 to US$213 per sq km. It was found that labour costs accounted for the highest for remote sensing analysis, making up about 30% of the total cost, while in field sampling, the labour cost accounts for nearly 80% of the total cost (Foster et al. 2024).

Sozzi et al. (2021) and team conducted an economic comparison of satellite, plane, and UAV-acquired NDVI images to define a decision-making process for site-specific nitrogen application. The study was carried out in Italy, where the price of satellite, plane, and UAV were considered to acquire vegetation indices. The result was compared to the economic benefit resulting from variable-rate nitrogen application. The results showed that the medium resolution satellite (10m to 15m) is profitable for a minimum field size of 2.52 ha. The high-resolution satellite imagery becomes profitable from 13.2 ha, while the very high-resolution satellite imagery becomes profitable after 76.8 ha. Similarly, an airplane-acquired NDVI is profitable after a field size of 66.4 ha. The UAV was not found economically

profitable for variable rate nitrogen fertilization of grains, as the average price per hectare was higher than the average economic benefits resulting from their use. The break-even costs were found at €83.1 for medium-resolution satellites, €434 for high-resolution satellites, €2,191 for aircraft imagery, and €2,536 for very high-resolution satellite imagery, while UAV imagery did not reach a profitable break-even point (Sozzi et al. 2021). Table 4 summarizes the studies from Fisher et al. (2018), Foster et al. (2024), and Sozzi et al. (2021), where UAVs are generally not economically viable, and satellite or aircraft imagery are found cost-effective only for larger field sizes.

Table 4. Economic aspect of Satellite imagery and UAV.

Study	Data used	Findings	Conclusion
Fisher et al. (2018)	DigitalGlobe's - QuickBird and WorldView 2, and Landsat	**Cost:** DigitalGlobe: $6,969 and Landsat: $0 **Processing:** High resolution image takes higher storage and 4 times more processing time than lower resolution images	Purchasing and processing high-resolution imagery is costly.
Foster et al. (2024)	Sentinel -2, PlanetScope, UAV imagery, and integrated monitoring with field sampling	Sentinel-2: $33-$63 per sq km PlanetScope: $77-$241 per sq km UAV: $9,220 - $58,481/ sq km Integrated approach: $144 - $213 per sq km	The operational cost of UAV is very high than using satellite imagery. Labour cost accounts 30% for remote sensing cost and 80% for field sampling cost

Sozzi et al. (2021)	Satellite (medium, high, very high resolution), aircraft imagery, and UAV	**Break-even costs:** Medium-resolution satellite: €83.1 High-resolution satellite:€434 Aircraft €2,191 Very high-resolution satellite €2,536 UAV: not profitable **Profitability on field size:** Medium-resolution satellites: 2.52 ha High-resolution: 13.2 ha Aircraft: 66.4 ha very high-resolution satellites: 76.8 ha UAV: not profitable	UAV imagery was not economically profitable

3.6 Comparing the satellite image and the UAV image

There are numerous benefits of using UAVs over satellite images for landscape analysis, such as the study of land use and land cover. The major disadvantage of using satellite data is cloud cover, which makes it difficult and sometimes impossible to detect and analyze the land under the cloud. Although numerous high-resolution satellites are available, such as GeoEye and WorldView, their output may contain less visible and analyzable scene due to cloud cover (Sanga et al. 2012).

Iizuka et al. (2018) conducted a study to demonstrate the advantage of drone photogrammetry for collecting more detailed and useful local landscape information than satellite data. The postmining site in Indonesia was selected as a study area considering its complex topography and landscape. For the UAV image, considering flying height regulations, the study area was further divided into two sites, where Site 1 is in the south-central part of the island, and Site 2 is in the eastern part of the island. The satellite remote sensing data were obtained from the Advanced Land Observation Satellite-2 (ALOS-2) Phased Array L-band Synthetic Aperture Radar-2 (PALSAR-2). SAR sensor data was used to avoid cloud cover. Another dataset used was drone-based aerial photos with a DJI Phantom 4 quadcopter. Two products of land use land cover maps were generated by Satellite image (SAR) based and UAV-based data. Then, a conventional accuracy assessment was conducted with random sample points. The result of the accuracy assessment of satellite images was found to be 78.1%. Further, for

UAV image processing, 655 drone images were captured in site 1 and 517 images in site 2. Photoscan Pro software was used to generate an orthophoto. The land cover map was then generated considering four land cover classes: water bodies, vegetation, bare soil, and houses. Accuracy assessment was carried out using the ground truth points collected through imagery. The overall accuracy result was 89.9% and 94.7% for site 1 and site 2, respectively. The land cover map generated from each source has a distinct difference. The spatial resolution is the main factor, as the SAR satellite image is 7.5 and the drone image is 0.05 m. The accuracy of SAR satellite data is specifically low due to the scattering mechanism of the microwave, depending on land objects, moisture content, topography, etc. Therefore, the author believes that conventional accuracy assessment does not make sense. To compare the two maps, the Kappa index of agreement (KIA) was computed to quantify the reliability of the SAR map to the drone map. The drone Land cover map was resampled to 7.5 m using the nearest neighbor algorithm with a 3x3 mode filter. The resulting KIA value was 0.42 and 0.33 for site 1 and site 2, respectively. According to the benchmarks established by Landis and Koch (1977), a value between 0.21 and 0.40 is classified as 'fair', while 0.41 to 0.60 is considered 'moderate'. The overall result of this study falls within a fair range. Consequently, Iizuka et al. (2018) conclude that drone technology serves as a superior alternative for high-resolution local landscape analysis. Hence, the author concludes by describing drone Technology as the alternative for local landscape analysis (Iizuka et al. 2018).

Jumaat et al. (2018) studied the capability of high-resolution satellite images and UAVs to study the change in land cover patterns in Cameron Highlands, Malaysia. Further, the land cover change pattern is also studied for the time frame of 12 years. Two satellite images from IKONOS imagery acquired in March 2001 and QuickBird imagery acquired in March 2007 were used for the study. 591 UAV images acquired in November 2013 were used to produce an orthophotography and hence for classification. The image classification was conducted in ArcGIS software with an object-based classification approach. A total of seven classes were defined as follows: agriculture, water body, forest, bare soil, grass, urban area, and landslide. After the classification, accuracy assessment was carried out in each class based on overall accuracy, kappa coefficient, commission errors, and omission errors. The overall accuracy has resulted as 86.67%, 83.89%, and 93.80% for the IKONOS satellite image, Quickbird satellite image, and UAV-developed orthophoto, respectively. The author concludes that all three images are an effective way for mapping land cover. However, the overall accuracy of the result from the UAV image is highest, so there is an advantage of flying UAVs for more accurate data. UAV images can collect precise information even in hilly terrains, which makes the overall accuracy higher (Jumaat et al. 2018).

Duke et al. (2022) studied the comparison of crop classification using UAV and SAR data using machine learning algorithms. The study was conducted in experimental plots using high-resolution multispectral 12cm UAV data (resampled to 50cm for efficient data handling) with the Sentinel 1A

SAR dataset. The Support Vector Machine (SVM) classifier produced an overall accuracy of 94.78% for the UAV and 81.72% for the SAR dataset. However, with Random Forest (RF), SAR performed 92.58% and became comparable to UAV 93.84%. The author suggests that this study would be useful in mapping small farm holdings and for precision agriculture. In contrast, SAR only data provides large area coverage, making it more suitable for larger fields. Further, the study also highlighted that spatial resolution has a strong influence on classification accuracy. The finer resolutions (50 cm) produced higher accuracies, while coarser resolutions (1–10 m) led to a decline in performance, although some classes, lake and mucuna, were less affected. Moderate resolutions (around 2–5 m) still provided acceptable results, but very coarse resolution significantly reduced classification accuracy (Duke et al. 2022). Table 5 summarizes studies by Iizuka et al. (2018), Jumaat et al. (2018), and Duke et al. (2022) that compare satellite imagery with UAV data, clearly showing that UAV imagery provides higher accuracy than satellite images.

Table 5. Comparing satellite imagery with UAV imagery.

Study	Objective	Data Source	Accuracy	Conclusion
Lizuka et al. (2018)	Compare Drone vs. Satellite (SAR) for local landscape analysis in complex topography.	UAV: DJI Phantom 4 (0.05 m)	Site 1: 89.9% (KIA: 0.42) Site 2: 94.7% (KIA: 0.33)	UAVs can be considered an alternative technology for local landscape analysis. Conventional accuracy assessment is flawed for SAR due to the scattering mechanism
		Satellite: ALOS-2 PALSAR-2 (SAR) (7.5m).	78.1%	
Jumaat et al. (2018)	Analyze LULC change over a 12-year timeframe using Satellite and UAV data.	UAV: Fixed wing Helang	93.80%	Overall accuracy of UAVs is highest, hence there is an advantage of flying UAVs for more accurate data.
		Satellite: IKONOS (1m)	86.67%	
		Satellite: QuickBird (0.65m)	83.89%	

Duke et al. (2022)	Comparison of UAV and SAR performance for Crop type classification using machine learning algorithms	UAV (12cm, resampled to 50cm)	RF Classifier: 93.84% SVM Classifier: 94.78%	UAV is more accurate due to finer resolution, but SAR can still achieve competitive accuracy with robust algorithms like RF
		Sentinel 1A SAR (10m)	RF Classifier: 92.58% SVM Classifier: 81.72%	

4. SYNTHESIS OF REVIEWED STUDIES

Land cover mapping technology has evolved from 1970 to the present day. In this time, various classification systems and satellite systems have been developed, which have helped to obtain great accuracy. With time, the availability of satellite images will be easier and less costly. With the help of a land cover map, one has been able to determine the change in the forest, agricultural, and urban land, which has helped the community to preserve the forest.

The spatial resolution of the image makes a great impact on the accuracy of land cover products. The higher spatial resolution makes it easy for a user to identify the object in the image, through which the user can provide a correct spectral signature for image classification. It is found that the increase in spatial resolution increases the overall accuracy of the land cover map. The classified image scale is equally important to maintain accuracy. For land cover classification using images from the coarse resolution satellites like MODIS, pose difficulties like the disappearance of small classes and an increase in proportional error in forested area classes. It is important to analyze the original spatial resolution of the image and the product scale of the classified image. The coarse satellite images should not be used to represent the large-scale classification maps.

The use of UAVs is becoming popular and can serve as an alternative technology for landscape analysis, including land cover classification. UAVs fly at a lower height and achieve a greater ground sampling distance, which enables the capture of finer details from the image. With UAVs, there are no issues with cloud cover, poor image quality, or difficulty collecting images on a desired date. Further, UAV image resolutions are very high compared to satellite images. UAVs are capable of capturing images in any landscape, which plays a great role in increasing the overall accuracy of the land cover product. The SAR sensor satellite omits the cloud cover issue, but its accuracy is found to be low compared to the UAV image. The accuracy of SAR images is highly sensitive to land objects, moisture contents, topography, and the scattering mechanism of the microwave, which can be avoided by UAV images.

High-resolution satellite images, like Quickbird and Worldview 2, can also be used to increase the

overall accuracy. Considering the technical and economic tradeoff, low-resolution satellite images can be considered much more reliable. The use of images from DigitalGlobe is very expensive compared to that of freely available, low-resolution, commonly used satellite images like Landsat and MODIS. Processing a high-resolution image requires additional processing time and hardware storage. The overall accuracy can be achieved with high-resolution images, but it is not reliable from the technical and economic points of view.

The economic tradeoff for using UAV images over satellite images depends on the scale of the project. The use of UAV images are found to be very costly for large-scale projects (eg, national-level land cover classification or state-level land cover classification) (Fisher et al., 2018; Foster et al., 2024; Sozzi et al., 2021). They are more economical for small projects covering a smaller area, such as local-level or municipal-level projects. UAV images require additional processing before classification. Initially, an orthomosaic must be developed using dedicated UAV processing software, which requires extra technical resources. Collecting UAV images demands extra fieldwork, skilled human resources and time. The UAV images are larger in size and need extra storage capacity. From a technical point of view, using high-resolution satellite images can be much more reliable compared to UAV images.

5. HYPOTHETICAL ACCURACY ANALYSIS

From the literature review, a large set of data was found, discussing accuracy across different study areas, sensors, classification methods, and the number of classes. A hypothetical accuracy analysis is carried out to address the lack of a unified quantitative comparison across the cited literature. The accuracy values compared here are drawn from studies with variation in numbers of classes, geographies, and classification algorithms. Across the cited literature, the geographies span tropical Indonesia, highland Malaysia, temperate Italy, and the Arctic, etc., and the classification algorithms include object-based, pixel-based, Support Vector Machine, and Random Forest approaches, etc. Each of these factors independently influences the overall accuracy. This analysis presents the descriptive summary in broad trends rather than a statistical benchmark, hence, the result should be interpreted considering these limitations.

5.1 Data Extraction

An overall accuracy across the sensors are collected from the cited literature. The sensors are then classified as per their category: Very High Resolution (≤1 m), High Resolution (> 1 m and ≤ 10 m), Medium Resolution (> 10 m and ≤ 30 m), Low Resolution (>30 m), SAR Satellites, and UAV. Table 6 consolidates the overall accuracy values found across various literature cited in this paper.

Table 6. Overall accuracy as per sensors from cited studies.

Study	Sensor	Resolution	Sensor Category	Accuracy
Liang et al. (2019)	CCI-LC	300m	Low resolution	63.5%
	GlobeLand30	30m	Medium resolution	62.2 %
	GLCNMO	1 km	Low resolution	48.8%
	MODIS	300m	Low resolution	29.5%
Mishra et al. (2016)	LISS IV (5.8m)	5.8m	High Resolution	83.28%
	Landsat 8 (30m)	30m	Medium resolution	77.93%
	AWiFS (56m)	56m	Low Resolution	74.61%
Fisher et al. (2018)	DigitalGlobe - QuickBird (0.6m) and WorldView 2 (0.5m) Resampled to 1m	1m	Very High Resolution	82.3%
	Landsat (30m)	30m	Medium Resolution	75.1%
Lizuka et al. (2018)	DJI Phantom 4 (Site 1)	0.05m	UAV	89.9
	DJI Phantom 4 (Site 2)	0.05m	UAV	94.7
	ALOS-2 PAL-SAR-2 (SAR)	7.5m	High Resolution / SAR	78.1
Jumaat et al. (2018)	Fixed wing Hel-ang	Not mentioned	UAV	93.80%
	IKONOS	1m	Very High Resolution	86.67%
	QuickBird	0.65m	Very High Resolution	83.89%

Duke et al. (2022)	UAV (Using SVM Classifier)	12cm	UAV	93.84%
	UAV (Using RF Classifier)	12cm	UAV	94.78%
	Sentinel 1A SAR (Using SVM Classifier)	10m	High Resolution / SAR	81.72%
	Sentinel 1A SAR (Using RF Classifier)	10m	High Resolution / SAR	92.58%

5.2 Hypothetical Analysis Summary

A group of 17 data were re-classified in Table 6 as per the sensor category, to provide a descriptive accuracy performance. Three observations were considered in SAR as well as high-resolution imagery. Table 7 presents the number of observations, minimum overall accuracy, maximum overall accuracy, and mean overall accuracy as per the sensor category.

Table 7. Hypothetical Analysis of Sensor Accuracy.

Sensor Category	No. of Observations	Minimum Overall Accuracy (%)	Maximum Overall Accuracy (%)	Mean Overall Accuracy (%)
UAV	5	89.9	94.78	93.40
SAR	3	78.1	92.58	84.13
Very High Resolution (≤1 m)	3	82.3	86.67	84.29
High Resolution (> 1 m to ≤ 10 m)	4	78.10	92.58	83.92
Medium Resolution (> 10 m to ≤ 30 m)	3	62.20	77.93	71.74
Low Resolution (> 30 m)	4	29.50	74.61	54.10

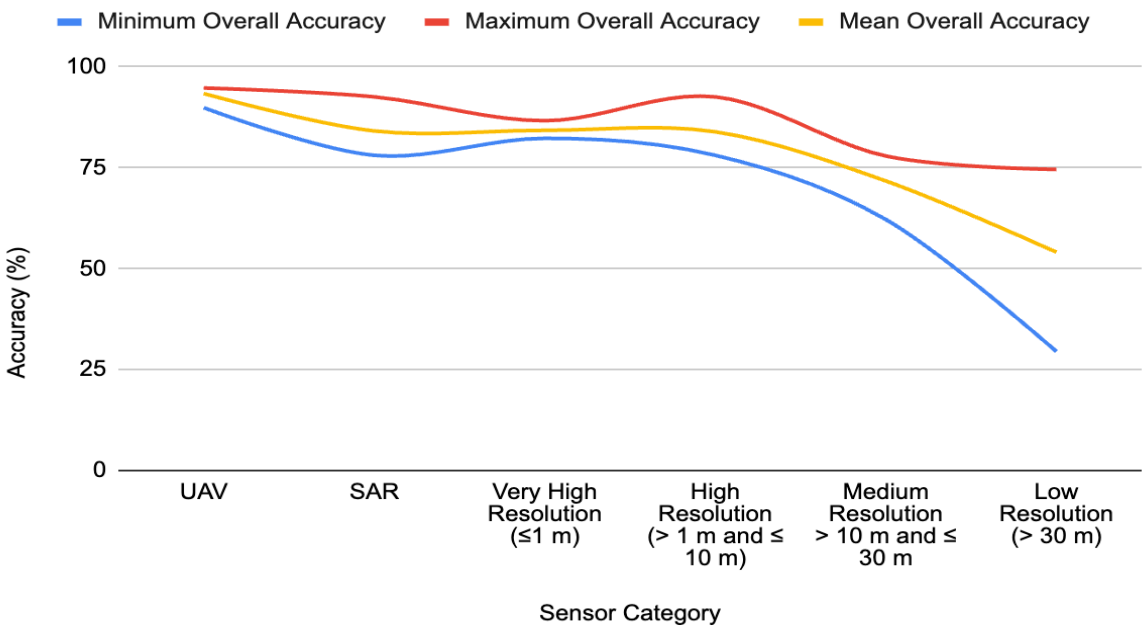

Figure 1. Hypothetical Analysis Chart of Sensor Accuracy.

The analysis presented represents the accuracy trend discussed from the literature review. Among all of the sensor types, UAV consistently achieved the highest mean overall score with 93.40%, followed by Very High resolution imagery with 84.29% and SAR imagery with 84.13%. The high resolution imagery was found with an overall accuracy of 83.92%, while medium resolution decreased to 71.74%, and low resolution with 54.10%. The SAR satellite category shows a wide range (78.10% to 92.58%), representing a wide range of sensitivity as per the classification algorithm choice (Duke et al. 2022).

The trend highlights that UAV has the highest overall accuracy, and it can be understood that the image resolution plays an important role in obtaining the overall accuracy. As UAV has the highest resolution, it can be considered as an alternative technology for high accuracy land cover classification. The 3 SAR imagery, which all being high resolution, the SAR imagery has higher mean overall accuracy than the accuracy of very high resolution imagery. It can be understood that SAR imagery can obtain higher

The trend indicates that UAV data achieves the highest overall accuracy, which can be understood as spatial resolution plays a crucial role in obtaining classification accuracy. Due to its very high resolution, UAV imagery can serve as an alternative technology to achieve highly accurate land cover maps. Among the three high-resolution SAR datasets, the mean overall accuracy is higher than that of very high resolution optical imagery. This implies that SAR imagery can provide comparatively strong classification performance; however, the hypothetical analysis shows that its overall accuracy still remains lower than that achieved by UAV data.

6. DISCUSSION

6.1 Impact of resolution and other factors on accuracy

The studies in the literature review gave in-depth information about the importance of spatial resolution and its impact on the accuracy of land cover classification products. Most literature highlighted that an increase in spatial resolution gives better accuracy; the UAV imagery was found to have the highest accuracy compared to that of satellite imagery. It is understood that with an increase in spatial resolution, one could identify the objects clearly in the image. With this, the user can provide a better spectral signature that would correctly classify the image.

However, studies from coarse resolution products in the Arctic Region indicate that spatial resolution cannot guarantee the accuracy of the classification. Liang and team (2019) showed that the accuracy of GlobeLand30, having 30m resolution, was lower than that of CCI-LC, having 300m resolution, in the Arctic. This suggests that landscape homogeneity, spectral signature, and sensor characteristics can outweigh the resolution advantage.

Further, the literature suggests that several factors—such as the number of classes selected, the choice of classification approach, the nature of the landscape, and data quality, also influence the overall accuracy. It is necessary to apply atmospheric correction to an image before classifying, as this will determine the true surface reflectance value, removing the atmospheric effect. (Themistocleous and Hadjimitsis 2008). A study has shown that there is a decrease in 0.77% of maps' overall accuracy with an increase in class (Thinh et al. 2019). There are two classification methods in remote sensing: Pixel-Based Image Analysis (PBIA) and Object-based image analysis (OBIA), with supervised and unsupervised classification approaches; these classification methods make a heavy impact on the overall accuracy of the product.

Spectral resolution also plays a vital role in classification accuracy. Navulur (2006) suggested that for most GIS applications where satellite images are used as a backdrop, three-band natural color imagery in RGB format is commonly used. For vegetation classification, visible and near - infrared can be used, and for more detailed applications such as mineral exploration and forest species classification, multispectral or hyperspectral data can be used. The finer the radiometric resolution, the more it can detect small features through the reflected or emitted energy. It can therefore be assumed that a finer radiometric resolution increases classification accuracy. However, a detailed study is necessary to understand the role of radiometric resolution for the overall accuracy of the land cover product.

6.2 Comparison of Sensors: Optical, SAR, and UAV

Optical sensors are considered a standard for monitoring global change; however, it is frequently compromised by atmospheric conditions. UAVs can be considered as an alternative technology to ad-

dress this gap, considering their capability of flying in lower elevations and avoiding the cloud cover, and their ability to integrate sensors. Using a UAV, one can collect images on the desired date, and there are no issues of cloud cover, weather, or bad image results. Fisher et al (2018) had to merge two images from different dates to eliminate the cloud cover in the image. Such issues can easily be omitted using UAVs. UAVs offer a greater ground sampling distance, which enables them to distinguish the smallest element in the image. With high resolution and greater ground resolving distance, it makes a great impact to increase the overall accuracy of the land cover classified image.

Synthetic Aperture Radar (SAR) sensors are capable of omitting cloud cover from the satellite images. However, the literature found their accuracy of land cover products from SAR sensors is still low compared to that of UAV imagery. Duke et al. (2022) found that SAR can still achieve competitive accuracy with robust algorithms like Random Forest, but its accuracy is still low compared to UAV images. The SAR sensors are not capable of interpreting the complex variable and are very sensitive to land objects, moisture contents, topography, and the scattering mechanism of the microwave. Iizuka et al. (2018) mentioned that SAR maps give an average KIA of 0.375, which is not a satisfying result for landscape analysis. UAV devices can capture an image in any type of landscape. The UAV is equipped with a 360-degree movable camera, this allows pilots to capture images from any angle. This capability enables effective imaging across diverse landscapes and topographies, while the integration of sensors further enhances accuracy.

6.3 Scalability, Technical and Economic Trade-off

The reviewed literature presents the idea on technical and economic tradeoff for using UAV over satellite images, where it is found that the decision factor is to be made by the scalability of the project (Fisher et al., 2018; Foster et al., 2024; Sozzi et al., 2021).

Image acquisition with UAV images in a small area would require less time and manpower, but in a large area, it would require many UAV devices, manpower, and powerful computers to process the images and prepare land cover maps. UAV images need additional processing before classifying an image. The orthomosaic needs to be developed from a separate UAV image processing software, which will later be used for land cover classification. Fisher et al (2018), determined that land use classification time for high-resolution images was 4 times longer than using a low-resolution image. The literature also evaluated the cost of using high-resolution satellite images with low-resolution images. The operational cost of UAV is much higher than the satellite imagery. It can be suggested that using UAVs over satellite images will require additional manpower and powerful computers, which is not economical.

Considering the technical tradeoff, to collect data from a UAV, a licensed UAV pilot is necessary to fly UAVs. Then, a separate processing software needs to be installed. Processing a UAV image is very time-consuming, which requires a hardware device with a better computer processor and RAM. The

image size is very large; this may require an additional storage device.

Therefore, from the technical and economic perspective, UAV-based land cover mapping is typically feasible for the local level project covering a small area. For a national or state-level project, the economic challenge, computational demands, and longer processing time make the satellite imagery a more practical choice.

6.4 UAV as an alternative technology

The literature suggests that UAV images can be used by local bodies to evaluate their landscape (Iizuka et al. 2018). Highly accurate, high-resolution land cover imagery would help to determine an accurate change in land pattern. It can be used to understand the change in the forest, agricultural land, and urbanization growth. The climate change researchers need to work on the accuracy of inches to determine the glacier melt, change in river pattern, etc. Even the high-resolution satellite will not be able to capture the images to determine the change in inches. The use of UAVs would be a great benefit for researchers to determine such a change.

To study climate change, determining the ice melt in the Arctic region, it is important to correctly assess the land cover of the Arctic Region. Liang et al. (2019) came up with a conclusion stating there is no ideal land cover product in terms of accuracy for studying land cover change in the Arctic Region. The issue with the Arctic region is its divided and unevenly distributed surface, which is difficult to analyze with satellite imagery. UAV is capable of capturing images on any landscape surface. UAV being able to capture an image, adjusting its flying height, and having a better ground sampling distance, UAV can be taken as an alternative technology to assess the land cover of the Arctic region. It is important to find out the capabilities of UAV images over satellite images to access the Arctic region.

The major threat of using UAV imagery over satellite imagery is the availability of old data. A series of old satellite imagery data can be found on the web, which is ready for analysis. UAV is capable of capturing data in the future date, but old data cannot be found. The change in landscape analysis for past years cannot be determined using UAV images. For example, there will be no data to analyze the glacier melt for the last 5 years, but the same analysis for the next 5 years can be conducted, with more accurate data. It is necessary to store the safe for a long time for later use. Satellites keep moving on their own, and no extra effort is necessary to capture data from the satellite. Using a UAV, one needs to go to the field on the desired date and should be able to collect data.

6.5 Application of an accurate land cover map

The review also highlights various purposes of an accurate land cover map. Dalle et al. (2006) used it to monitor the impact of forest conservation. Dalle's research is evidence of how the land cover map can be used to solve real-world challenges like the conservation of a forest. Dalle has an overall

accuracy of 81%. The research used a series of Landsat images from 1976, 1988, 1991, 1997, and 2000, whose spatial resolution is 30m. Regarding Varun Narayan Mishra et al. (2016) and Iizuka et al. (2018) research, we can understand that the use of high-resolution UAV images would produce more accurate land cover maps. Dalle's research, which monitors the change in the loss of forest land, can be analyzed using UAV images for more accurate results. This would increase the overall accuracy, and the result will help the community and conservationists to understand the impact and make necessary decisions.

Land cover classification technology has evolved with time. The accuracy of the land cover map and availability of the satellite imagery have been the things to be most important. The current trends indicate that the availability of data has been much easier, as most data can be ordered and downloaded from the web. The development of new sensors and high-resolution satellites has been able to provide good resolution imagery, which has made a great impact in improving the overall accuracy of the land cover products. With the end of commercialization of Landsat imagery in the 1990s, we can predict that satellite imagery will become much cheaper and eventually all satellite images will be freely available.

6.6 Limitations and Recommendations

This review is limited to a small number of manually selected literature; the findings of this review contain narrative analysis but are limited mostly to classification accuracy. Future research should prioritize a systematic review to statistically analyze classification methods, the number of land cover classes, and the choice of different sensors. Such an analysis would allow quantitative comparison and strengthen the review.

This review does not incorporate the temporal analysis and has limited information about the technological advancement of UAVs for land cover analysis. Future research can examine temporal resolution and determine how the accuracy of landcover analysis has been strengthened with the advancement of UAV technology.

While this review touches on the potential of SAR imagery, this does not prioritize the nuances of satellite imagery fusion, SAR fusion, and individual SAR bands. To strengthen the understanding of SAR alongside UAV imagery, incorporating these factors in future systematic reviews would provide a more definite roadmap for selecting accurate and cost-effective tools for landcover mapping.

7. CONCLUSION

This review analyzed the findings from various existing literature to understand the impact of UAV images for an accurate land cover map, with a focus on comparing UAV and satellite imagery on classification accuracy, operation cost, and scalability. The reviewed studies indicate that spatial res-

olution has a great impact on the accuracy. UAVs can achieve higher accuracy than most satellite imagery, with a mean overall accuracy of 93.40% in the hypothetical study. For comparison, very high-resolution satellite imagery reached a mean overall accuracy of 84.13%, high-resolution SAR imagery achieved 84.29%, high-resolution imagery reached 83.92%, and medium- and low-resolution imagery achieved 71.74% and 54.10%, respectively.

The reviewed literature also discusses the economic and technical tradeoff. UAVs offer high accuracy and are found flexible for local scale mapping, with advantages of their sensor's high resolution, sensor integration, and cloud cover constraints. However, UAVs are found most costly, which demands a licensed pilot, high processing time, and processing software. It is suggested that satellite imagery is indispensable for global applications due to its coverage, temporal continuity, and scalability of the project. Low-resolution satellite imagery is identified as the most cost-effective, but it has low classification accuracy. High-resolution commercial satellites bridge the accuracy gap, but the financial cost and processing time are high. In summary, it can be understood that UAVs can be preferred as an alternative technology for local-scale land cover mapping where great detail and accuracy are required, whereas satellite imagery remains the practical and economic solution for large-scale global monitoring.

This study is limited to a few manually selected literature sources, and the findings are limited to the selection criteria adopted. The future research should focus on a systematic review with defined inclusion and exclusion criteria, a comparative analysis that enables evaluation of sensor performance and classification accuracy. Further, examining temporal trends can provide insights into the technological advancement of landcover analysis with UAV technology.

This review also recommends an understanding of other factors like the number of classes, classification methods, and sensor types, which have an important impact on the accuracy of land cover classification.

REFERENCES

Anderson, J. R., Hardy, E. E., Roach, J. T., & Witmer, R. E. (1976). A land use and land cover classification system for use with remote sensor data (Geological Survey Professional Paper 964). U.S. Department of the Interior. https://doi.org/10.3133/pp964

CNES (Centre National d'Études Spatiales). (2025). Pléiades. Last modified September 19, 2025. https://cnes.fr/en/projects/pleiades

Dalle, S. P., de Blois, S., Caballero, J., & Johns, T. (2006). Integrating analyses of local land-use regulations, cultural perceptions and land-use/land cover data for assessing the success of community-based conservation. Forest Ecology and Management, 222(1–3), 370–383. https://doi.org/10.1016/j.foreco.2005.10.052

Dewitz, J., & USGS. (2021). National Land Cover Database (NLCD) 2019 products (ver. 3.0, February 2024). U.S. Geological Survey data release. https://doi.org/10.5066/P9KZCM54

Di Gregorio, A., & Jansen, L. J. M. (2000). Land cover classification system (LCCS): Classification concepts and user manual. Environment and Natural Resources Service, Africover–East Africa Project & Soil Resources, Management and Conservation Service.

Duke, O. P., Alabi, T., Neeti, N., & Adewopo, J. (2022). Comparison of UAV and SAR performance for crop type classification using machine learning algorithms: A case study of humid forest ecology experimental research site of West Africa. International Journal of Remote Sensing, 43(11), 4259–4286. https://doi.org/10.1080/01431161.2022.2109444

ESA. (n.d.). The Sentinel missions. European Space Agency. Retrieved March 1, 2026, from https://www.esa.int/Applications/Observing_the_Earth/Copernicus/The_Sentinel_missions

Fisher, J. R. B., Acosta, E. A., Dennedy-Frank, P. J., Kroeger, T., & Boucher, T. M. (2018). Impact of satellite imagery spatial resolution on land use classiŞcation accuracy and modeled water quality. Remote Sensing in Ecology and Conservation, 4(2), 137–149. http://doi.org/10.1002/rse2.61

Foody, G. M. (2002). Status of land cover classification accuracy assessment. Remote Sensing of Environment, 80(1), 185–201. https://doi.org/10.1016/S0034-4257(01)00295-4

Foster, A., Rahimzadeh-Bajgiran, P., Daigneault, A., & Weiskittel, A. (2024). Cost-effectiveness of remote sensing technology for spruce budworm monitoring in Maine, USA. Forests Monitor, 1(1), 66–98. https://doi.org/10.62320/fm.v1.i1.14

Fu, P., & Weng, Q. (2015). A time series analysis of urbanization induced land use and LC change and its impact on land surface temperature with Landsat imagery. Remote Sensing, 7(12), 16671–16698. https://doi.org/10.3390/rs71215844

Ge, J., Qi, J., Lofgren, B. M., Moore, N., Torbick, N., & Olson, J. M. (2007). Impacts of land use/cover classification accuracy on regional climate simulations. Journal of Geophysical Research: Atmospheres, 112(D5), Article D05120. https://doi.org/10.1029/2006JD007404

Giri, C. P. (2012). Remote sensing of land use and land cover: Principles and applications. CRC Press; Taylor & Francis Group.

Guha, S., Govil, H., Gill, N., & Dey, A. (2020). Analytical study on the relationship between land surface temperature and land use/land cover indices. Annals of GIS, 26(2), 201–216. https://doi.org/10.1080/19475683.2020.1754291

Horning, N. (2004). Overview of accuracy assessment of land cover products (Version 1.0). American Museum of Natural History, Center for Biodiversity and Conservation. Retrieved May 1, 2021, from http://biodiversityinformatics.amnh.org

Iizuka, K., Itoh, M., Shiodera, S., Matsubara, T., Dohar, M., Watanabe, K., & Bhardwaj, A. (2018). Advantages of unmanned aerial vehicle (UAV) photogrammetry for landscape analysis compared with satellite data: A case study of postmining sites in Indonesia. Cogent Geoscience, 4(1), Article 1498180. https://doi.org/10.1080/23312041.2018.1498180

Jumaat, N. F. H., Ahmad, B., & Dutsenwai, H. S. (2018). Land cover change mapping using high resolution satellites and unmanned aerial vehicle. IOP Conference Series: Earth and Environmental Science, 169(1), Article 012076. https://doi.org/10.1088/1755-1315/169/1/012076

Kovacic, L. (2025). Open land cover maps – Validation from the user perspective (Master's thesis, University of Zagreb). https://urn.nsk.hr/urn:nbn:hr:256:657876

Landis, J. R., & Koch, G. G. (1977). The measurement of observer agreement for categorical data. Biometrics, 33(1), 159–174.

Liang, L., Liu, Q., Liu, G., Le, H., & Huang, C. (2019). Accuracy evaluation and consistency analysis of four global land cover products in the Arctic region. Remote Sensing, 11(12), Article 1396. https://doi.org/10.3390/rs11121396

Lindsey, R. (2020). Climate change: Glacier mass balance. Climate.gov. Retrieved April 4, 2021, from https://www.climate.gov/news-features/understanding-climate/climate-change-glacier-mass-balance

Markham, B. L., & Barker, J. L. (1985). Spectral characterization of the Landsat Thematic Mapper sensors. International Journal of Remote Sensing, 6(5), 697–716. https://doi.org/10.1080/01431168508948492

Mishra, V., Rai, P. K., Kumar, P., & Prasad, R. (2016). Evaluation of land use/land cover classification accuracy using multi-resolution remote sensing images. Forum Geografic, 15(1), 45–53. https://doi.org/10.5775/fg.2016.137.i

Moody, A., & Woodcock, C. E. (1994). Scale-dependent errors in the estimation of land-cover proportions: Implications for global land-cover datasets. Photogrammetric Engineering and Remote Sensing, 60(5), 585–594.

Mooney, C., & Freedman, A. (2021, January 25). Earth is now losing 1.2 trillion tons of ice each year. And it's going to get worse. The Washington Post. https://www.washingtonpost.com/climate-environment/2021/01/25/ice-melt-quickens-greenland-glaciers/

Mora, B., Tsendbazar, N. E., Herold, M., & Arino, O. (2014). Global land cover mapping: Current status and future trends. In I. Manakos & M. Braun (Eds.), Land use and land cover mapping in Europe (Remote Sensing and Digital Image Processing, Vol. 18, pp. 11–23). Springer. https://doi.org/10.1007/978-94-007-7969-3_2

NASA. (2026). MODIS specifications. MODIS Web. Retrieved January 9, 2026, from https://modis.gsfc.nasa.gov/about/specifications.php

National Ocean Service. (2024). What is the difference between land cover and land use? National Oceanic and Atmospheric Administration. Retrieved January 12, 2025, from https://oceanservice.noaa.gov/facts/lclu.html

Navulur, K. (2006). Multispectral image analysis using the object-oriented paradigm. CRC Press. https://doi.org/10.1201/9781420043075

Purevdorj, T. S., Tateishi, R., Ishiyama, T., & Honda, Y. (1998). Relationships between percent vegetation cover and vegetation indices. International Journal of Remote Sensing, 19(18), 3519–3535. https://doi.org/10.1080/014311698213795

Sanga-Ngoie, K., Iizuka, K., & Kobayashi, S. (2012). Estimating CO2 sequestration by forests in Oita Prefecture, Japan, by combining LANDSAT ETM+ and ALOS satellite remote sensing data. Remote Sensing, 4(11), 3544–3570. https://doi.org/10.3390/rs4113544

Satellite Imaging Corporation. (n.d.). QuickBird satellite sensor. Retrieved March 8, 2026, from https://www.satimagingcorp.com/satellite-sensors/quickbird/

Semenyuk, V., Kurmashev, I., Lupidi, A., Alyoshin, D., Kurmasheva, L., & Cantelli-Forti, A. (2025). Advances in UAV detection: Integrating multi-sensor systems and AI for enhanced accuracy and efficiency. International Journal of Critical Infrastructure Protection, 49, Article 100744. https://doi.org/10.1016/j.ijcip.2025.100744

Setyawan, E. (2019, May 25). Satellite imagery: Resolution vs. accuracy. Intermap Blog. https://www.intermap.com/blog/satellite-imagery-resolution-vs.-accuracy

Sozzi, M., Kayad, A., Gobbo, S., Cogato, A., Sartori, L., & Marinello, F. (2021). Economic comparison of satellite, plane and UAV-acquired NDVI images for site-specific nitrogen application: Observations from Italy. Agronomy, 11(11), Article 2098. https://doi.org/10.3390/agronomy11112098

Themistocleous, K., & Hadjimitsis, D. G. (2008). The importance of considering atmospheric correction in the pre-processing of satellite remote sensing data intended for the management and detection of cultural sites: A case study of the Cyprus area. 14th International Conference on Virtual Systems and Multimedia (VSMM 2008), 125–132.

Thinh, T. V., Duong, P. C., Nasahara, K. N., & Tadono, T. (2019). How does land use/land cover map's accuracy depend on number of classification classes? SOLA, 15, 28–31. https://doi.org/10.2151/sola.2019-006

U.S. Environmental Protection Agency. (2008). EPA's 2008 report on the environment (Report No. EPA/600/R-07/045F). National Center for Environmental Assessment. http://www.epa.gov/roe

Verburg, P. H., Neumann, K., & Nol, L. (2011). Challenges in using land use and land cover data for global change studies. Global Change Biology, 17(2), 974–989. https://doi.org/10.1111/j.1365-2486.2010.02307.x

Yan, W. Y., Shaker, A., & El-Ashmawy, N. (2015). Urban land cover classification using airborne LiDAR data: A review. Remote Sensing of Environment, 158, 295–310. https://doi.org/10.1016/j.rse.2014.11.001

ADVANCES IN GEOMATICS

VOLUME 04 • ISSUE 01 • APRIL 2026
e-ISSN: 3023-4980

ORIGINAL ARTICLE

Submission: 11/02/2026
Accepted: 23/04/2026

IMPACT OF BUILDING MATERIALS ON WI-FI SIGNAL PROPAGATION AND POSITIONING ACCURACY

Madhuwantha A.T.N.M[1]*, Prasanna H.M.I[1]

[1] Department of Surveying and Geodesy, Faculty of Geomatics, Sabaragamuwa University, Sri Lanka.

* Corresponding Author: Madhuwantha A.T.N.M, atnmmadhuwantha369@gmail.com 0009-0000-3581-9612

ABSTRACT

Indoor Positioning Systems (IPS) are essential for reliable navigation and location-based services inside buildings. However, construction materials introduce signal attenuation that reduces the accuracy of these systems. This study investigates the propagation of Wi-Fi signals through five different wall materials: concrete, drywall, glass, white-faced hardboard, and wood. The research introduces the Wall Attenuation Factor (WAF) to quantify signal loss and integrates it into Wi-Fi-based localization algorithms. Experimental results demonstrate that incorporating WAF significantly enhances positioning accuracy, reducing errors from 1–2.5 m to 20–50 cm. Coordinate accuracy improved from 0.5–6 m (X) and 1–4 m (Y) to 10–65 cm (X) and 20–30 cm (Y). Concrete walls caused the greatest signal attenuation, while wood and white-faced hardboard allowed signals to pass with minimal degradation. Optimal router placement, within 4 meters of the receiver and with proper alignment, further enhances performance. Future research will explore three-dimensional positioning and test the impact of environmental variables such as humidity and air density.

Keywords: Indoor positioning systems, Signal attenuation, Wall Attenuation Factor (WAF), Wi-Fi localization, Wireless communication.

Cited As:

Madhuwantha, A.T.N.M., & Prasanna, H.M.I. (2026). Impact of Building Materials on Wi-Fi Signal Propagation and Positioning Accuracy, Advances in Geomatics, 4(1), 64-82. https://doi.org/10.5281/zenodo.20546777

1. INTRODUCTION

A positioning system is a decision-making tool that determines the location of an object within an environment. Currently, positioning systems can be categorized into three main types: Global Navigation Satellite System (GNSS), LiDAR Positioning System (LPS), and Hybrid Positioning System (HPS). These systems are useful in both outdoor and indoor applications. GNSS, a satellite-based system, is commonly used for outdoor tasks including positioning (Dow et al., 2009), navigation, vehicle tracking (Abulude & Akinnusotu, 2015), and other spatial science applications. However, GNSS is ineffective for indoor localization due to severe signal attenuation and Non-Line-of-Sight (NLoS) propagation, resulting in positioning accuracies typically limited to approximately 2 to 6 meters (J, Wahab et al. 2022). Indoor localization is further complicated by the presence of barriers that obstruct line of sight, causing signal interference. Although mobile signals are often available indoors, Wi-Fi offers a better opportunity for accurate indoor localization (Aileen, Suwardi et al. 2021, Ekahau 2024).

Wi-Fi–based indoor positioning techniques can be broadly categorised into model-based approaches (e.g., Received Signal Strength Indication (RSSI) path-loss modelling and trilateration), fingerprinting-based methods, probabilistic frameworks, and learning-based approaches such as convolutional neural networks (CNNs) and recurrent neural networks (RNNs). Among these, Wi-Fi fingerprinting and deep learning–based indoor positioning systems (IPS) have demonstrated improved accuracy under certain conditions, often achieving sub-meter performance in controlled environments. However, this accuracy is typically obtained at the expense of extensive site surveys, dense labelled datasets, and periodic retraining to maintain performance as indoor environments evolve (Lymberopoulos et al., 2015; Zafari et al., 2019; Hernández et al., 2021).

Fingerprinting-based IPS methods rely on the construction of a radio map during an offline phase, followed by online matching during operation. Although effective, their performance degrades significantly when access point configurations, building layouts, or human occupancy patterns change, necessitating costly and time-consuming recalibration (He & Chan, 2015). Similarly, learning-based approaches including CNN and Long Short-Term Memory (LSTM)-based localization techniques require large training datasets and substantial computational resources, which limits their applicability in small-scale deployments and resource-constrained environments (Hernández et al., 2021).

Indoor environments, however, typically contain structural elements such as walls, floors, windows, doors, and corridors that obstruct Wi-Fi signal propagation. Path-loss models are commonly employed to account for these obstructions by estimating the attenuation introduced by each barrier along the signal path (Farid et al., 2013; Hernández et al., 2021). In such models, signal degradation is represented using loss factors associated with walls or floors that interfere with the direct line-of-sight between the transmitter and receiver.

Moreover, Wi-Fi signal propagation is strongly influenced by the type of building materials encoun-

tered, as different materials attenuate signals to varying degrees. Numerous studies have examined the effects of materials such as concrete, drywall, glass, and wood on Wi-Fi signal attenuation and transmission characteristics (Dao et al., 2014; Latif & Memon, 2011). Consequently, the impact of building elements and their material properties must be carefully considered when designing and deploying Wi-Fi-based indoor positioning systems, as they can significantly affect system accuracy and reliability.

The Wall Attenuation Factor (WAF)-enhanced trilateration approach is proposed in this study which adopts a lightweight, model-based strategy that avoids fingerprint databases, training datasets, and probabilistic inference. Instead, it explicitly incorporates material-specific signal attenuation into the RSSI path-loss model, thereby improving distance estimation accuracy while preserving the simplicity and interpretability of traditional RSSI-based positioning. Table 1 presents a quantitative comparison between representative IPS techniques reported in the literature and the proposed approach.

Table 1. Comparison of Wi-Fi–Based Indoor Positioning Approaches.

Method	Typical Accuracy (m)	Training/Survey required	Computational cost
RSSI Trilateration (Path-loss) (Farid et al. (2013); Pahlavan (1998)	1 – 3	No	Low
Wi-Fi Fingerprinting (He & Chan (2015); Liu et al. (2007)	1 – 3	Yes	Medium
Models (Bayesian, Kalman) (Zafari et al. (2019)	0.8 – 1.0	Partial	Medium
Deep Learning (CNN / LSTM) (Hernández et al. (2021); Lymberopoulos et al. (2015)	0.3 – 1.0	Yes	High
Proposed WAF-Based Trilateration	0.2 – 0.5	No	Low

Under controlled indoor conditions, the proposed approach achieved distance and positional accuracies in the range of 0.2–0.5 m, which is comparable to or better than many reported fingerprinting-based and learning-based methods, while maintaining significantly lower deployment complexity and computational overhead. These results indicate that the proposed method is particularly well suited to rapid-deployment scenarios, environments where site surveys are impractical, and applications that require transparent and easily interpretable positioning models.

In this context, the present study focuses on quantifying the impact of various building elements and materials on Wi-Fi signal propagation. By integrating a WAF into the Wi-Fi localisation process, the proposed approach enhances positioning accuracy and robustness while retaining the advantages of a simple and interpretable model-based framework.

2. STUDY AREA AND DATA COLLECTION

2.1 Study Area

The study was conducted at the Faculty of Geomatics, Sabaragamuwa University of Sri Lanka, which consists of various building elements constructed from materials such as concrete, drywall, glass, wood, etc. This variety provides an ideal setting to analyze the impact of different materials on Wi-Fi signal propagation.

Figure 1. The study area is composed of different building elements and materials.

This experiment was intentionally conducted in a controlled indoor environment to isolate the effect of building materials on Wi-Fi signal attenuation. Variables such as building layout, access point configuration, and receiver geometry were kept fixed to ensure that observed variations in signal strength could be primarily attributed to material-specific attenuation rather than environmental randomness.

2.2 Data Collection

Received Signal Strength Indication (RSSI) in Wi-Fi signal was measured at known distances in both open and obstructed indoor environments. Three Access Points (APs) were used, and signal strength was recorded at nine receiver points. Measurements were taken for each wall material, both inside and outside, to determine the Wall Attenuation Factor (WAF).

To address short-term signal variability and ensure repeatability, RSSI measurements at each observation point were recorded with different router angles continuously over a 20-second interval and averaged. This procedure was repeated independently three times at each location and for each wall material, with the router and receiver repositioned to the same surveyed coordinates. The reported RSSI values and derived WAFs therefore represent the mean of multiple independent trials.

3. METHODOLOGY

During data collection, measurements were taken during low-occupancy periods to minimize the influence of human movement and dynamic multipath effects. While this improves internal consistency, it also implies that the reported accuracy represents best-case performance under steady-state conditions.

The flow chart below illustrates the Methodology used in this study.

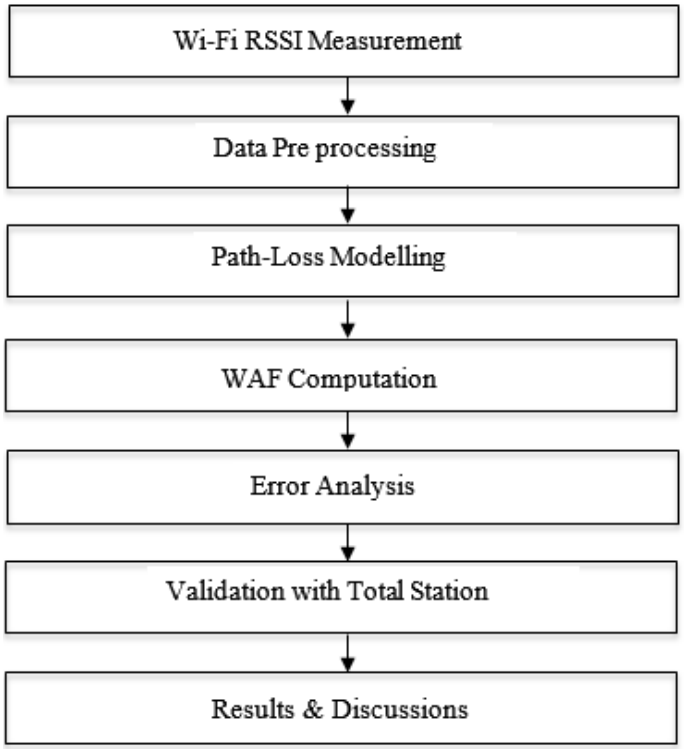

Figure 2. Workflow of the research process showing data acquisition, WAF computation, and positioning accuracy evaluation.

The methodology involved several key steps as follows:

Establishing Observation Points and Access Points (APs) Using a Total Station

Three indoor locations within the faculty were selected, each comprising three Wi-Fi access points and three observation points situated around various wall materials. A closed traverse was conducted from a known reference point to determine precise coordinates. All access points and observation points were accurately positioned using a Total Station to ensure high spatial precision.

Measuring Wi-Fi Signal Strength

Wi-Fi signal strength was measured using the AirPort Utility App in an obstacle-free environment to evaluate the basic signal attenuation characteristics. Signal readings were recorded at six known distances as 1 m, 2 m, 3 m, 4 m, 5 m, and 6 m from each router. These measurements were used to calculate the path loss exponent. Additionally, the orientation of the router antenna was varied to assess its impact on signal strength.

The path loss equation

The distance between observation points and each Wi-Fi access point (AP) was calculated using the path-loss equation (Dao et al., 2014): accuracy assessment of D model

$$P(d)[dB] = P(d_0)[dB] - 10n\log_{10}\left(\frac{d}{d_0}\right) - n_w WAF(p) \quad (1)$$

Where: P(d) is the esteemed signal strength at distance d, $P(d_0)$ is the reference path-loss at distance d_0 and n is the path losss exponent that depends on the indoor parameters, type of building, room size and other factors. n_w is the number of walls WAF is the wall attenuation factor.

To calculate the WAF for different wall materials, the router was positioned 4 meters away from the observation point with a wall in between, minimizing the influence of free-space signal fluctuations (Figure 3). The signal strength was recorded on both sides of the wall:

AVG1: Average signal strength inside the wall (before penetration),

AVG2: Average signal strength outside the wall (after penetration).

Then WAF is calculated as:

$$WAF = |AVG2 - AVG1| \text{ (dB)} \quad (2)$$

In which RSSI is measured in decibel-milliwatts (dBm). In this analysis, the values of WAF are expressed in the form of positive attenuation losses (dB). In this case, the values of WAF represent the contribution of each material to the reduction of the signal power. For example, a decrease of -40 dBm to -50 dBm is equivalent to a +10 dB WAF. There can be easy comparison of materials under this convention, whereby the higher the WAF values, the higher the attenuation. The attenuation of

concrete was the greatest, and that of wood and hardboard the least.

Determining and Comparing Locations

The trilateration method was applied to estimate positioning coordinates based on the measured distances from the receiver point to three access points (Farid et al., 2013; Elashry et al., 2019). The positioning accuracy was assessed by comparing these calculated coordinates with reference coordinates obtained using a Total Station. For data processing and accuracy evaluation, Wi-Fi-based location estimates were analyzed with the WAF model. Accuracy was evaluated by comparing the calculated distances and coordinates while incorporating the WAF values of individual wall materials. The impact of each wall's WAF on signal attenuation was analyzed to determine the most suitable WAF values for accurately modelling distance calculations in environments with mixed wall materials.

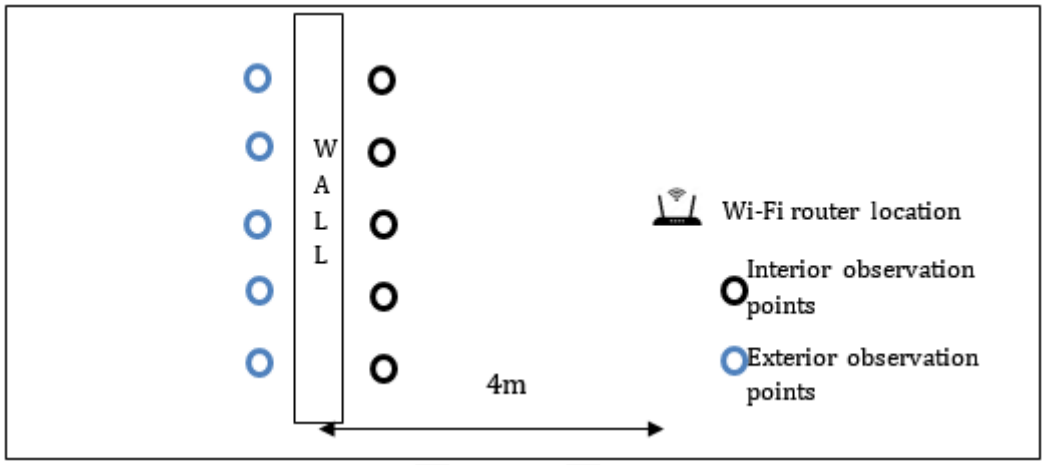

Figure 3. The setup of measuring WAF of wall materials.

4. RESULTS AND DISCUSSION

This section presents the results of Wi-Fi signal propagation analysis with a focus on positioning accuracy. It includes WAF measurements and evaluates the impact of various building materials on the accuracy of indoor positioning. The findings demonstrate the relationship between Wi-Fi signal strength at different distances and the signal attenuation caused by different wall materials, emphasizing how construction elements influence the overall performance of Wi-Fi-based positioning systems. Figure 4 shows the signal strength and distance relationship in an obstacle-free environment.

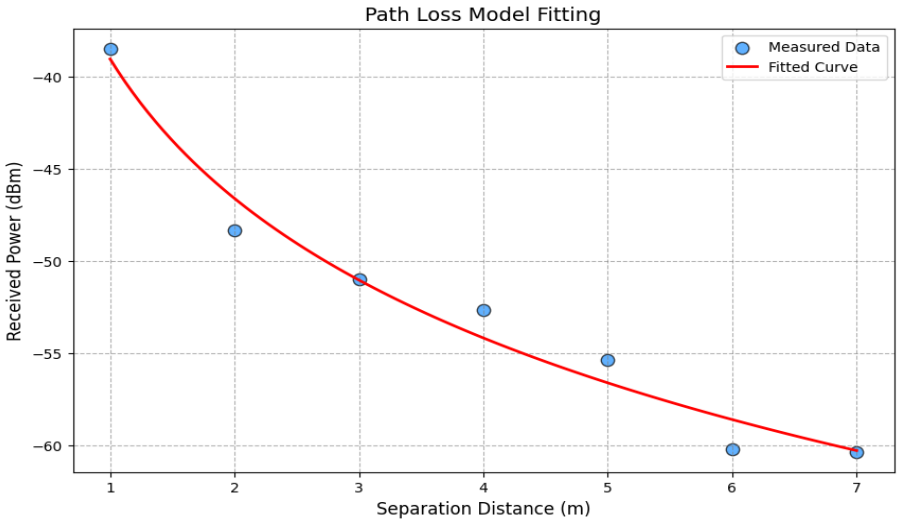

Figure 4. Represents the relationship between Wi-Fi signal strength and range from the Wi-Fi router. The estimated path loss exponent(n)= 2.51.

4.1 Accuracy analysis for distance calculation using Wi-Fi RSSI with and without applying WAF

Table 2 presents the statistical analysis of distance accuracy for Wi-Fi-based indoor positioning, both with and without considering wall materials. When wall materials are not accounted for, the positioning accuracy ranges from 1 to 2.5 meters, based on a 95% confidence interval for the mean received signal strength. In contrast, when WAFs are applied, the mean distance error decreased from 1.77 m to 0.37 m, with a corresponding reduction in standard deviation from 1.37 m to 0.31 m. The non-overlapping 95% confidence intervals confirm that the observed improvement is statistically significant across independent measurements. These results highlight the importance of considering building materials in enhancing the precision of Wi-Fi-based indoor positioning systems.

Table 2. Statistical results of distance calculation without and with applying WAF.

		Without Applying WAF	Applying WAF
Mean(m)		1.771	0.3729
Std. Deviation(m)		1.368	0.3148
95% Confidence Interval for Mean(m)	**Lower Bound**	1.2298	0.2484
	Upper Bound	2.3122	0.4975
Range(m)		5.67	1.31

4.2 Positional accuracy analysis with and without considering WAF

Table 3 and Figure 5 illustrate the differences in calculated coordinates with and without the application of WAFs. These comparisons clearly demonstrate the improvement in positioning accuracy achieved when WAF is integrated into the distance estimation model, emphasizing the effectiveness of incorporating material-specific attenuation in Wi-Fi-based indoor positioning systems.

Table 3. Displacements of coordinates with and without applying WAF.

	Without applying WAF		Applying WAF	
Observation Points	dx (m)	dy (m)	dx (m)	dy (m)
1	1.081	6.317	0.119	0.320
2	1.036	0.624	0.167	0.321
3	10.429	3.449	0.481	0.312
4	6.677	4.223	0.036	0.141
5	1.925	1.808	0.530	0.214
6	0.229	2.427	0.364	0.368
7	4.836	1.484	0.448	0.307
8	1.693	0.932	0.246	0.380
9	0.641	2.268	1.108	0.264

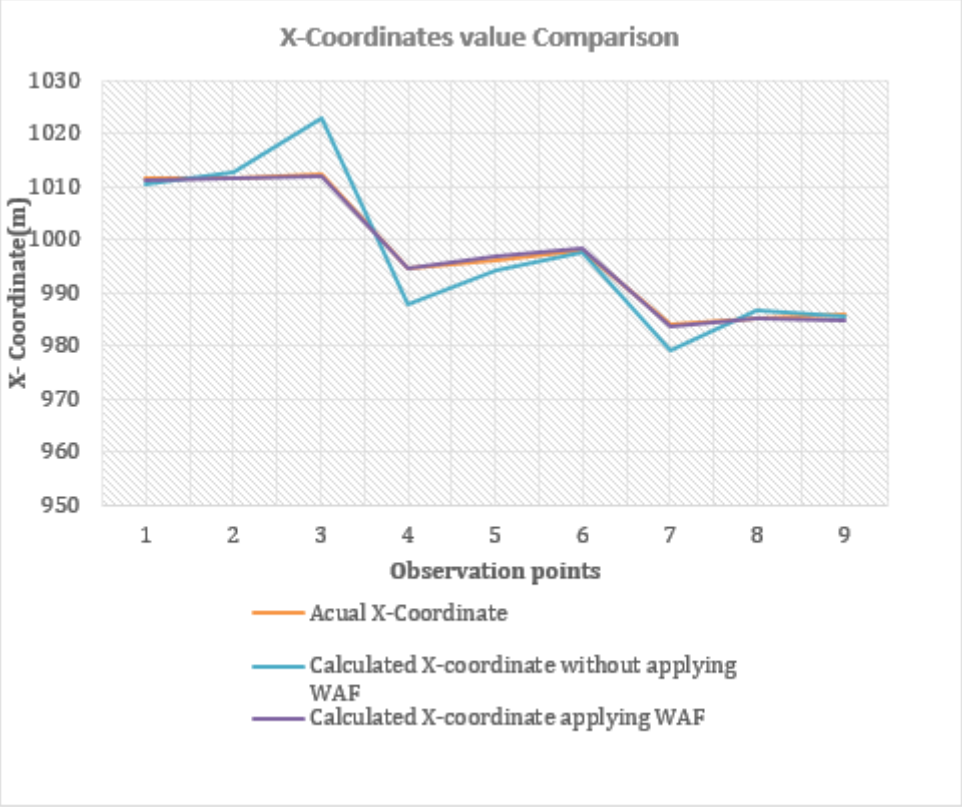

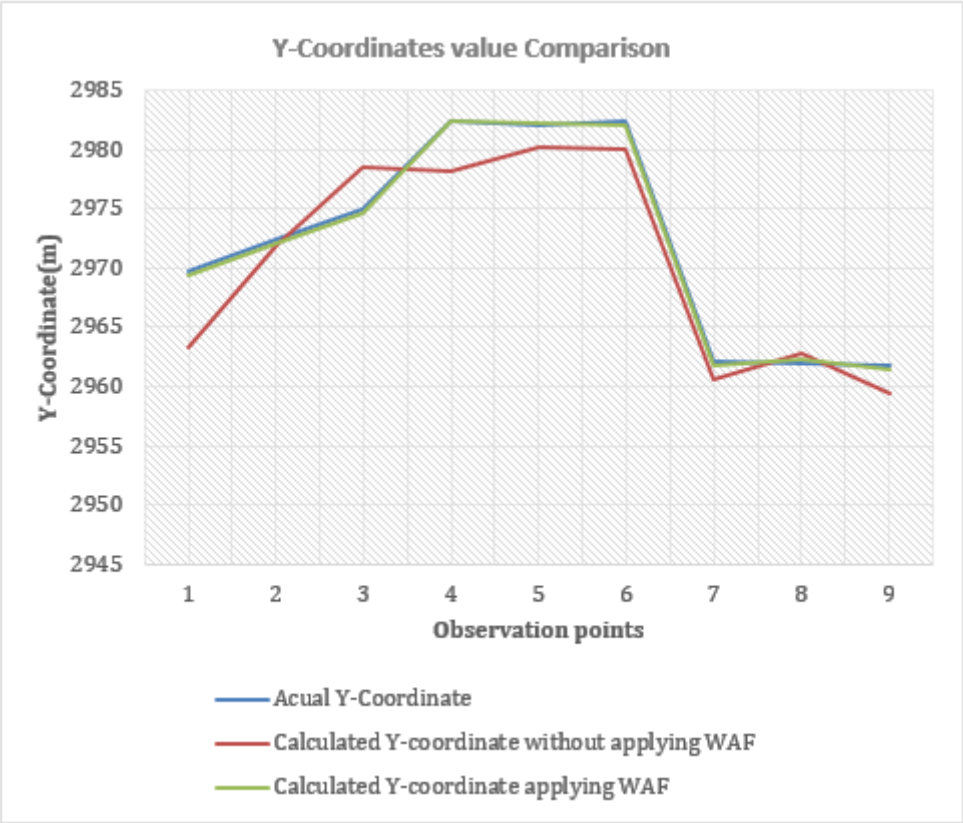

Figure 5. Position variation with and without applying WAF.

Table 4 shows the statistics of the above differences. It shows the clear enhancement of positional accuracy when applying the specific WAF.

Table 4. Statistical information for position calculations with and without WAF.

		Without applying WAF		Applying WAF	
		X Coordinate	Y Coordinate	X Coordinate	Y Coordinate
Mean(m)		3.1719	2.6147	0.3888	0.2919
Std. Deviation(m)		3.4543	1.7982	0.3197	0.0753
95% Confidence Interval for Mean(m)	Lower Bound	0.5166	1.2324	0.1430	0.2340
	Upper Bound	5.8272	3.9969	0.6346	0.3498
Range(m)		10.20	5.69	1.07	0.24

4.3 Distance accuracy analysis in a mixed environment

An actual indoor environment consists of various structural elements made from multiple construction materials. Therefore, it is important to evaluate the positioning accuracy with respect to different building materials prior to deploying a Wi-Fi-based indoor positioning system. In this study, three locations (A, B, and C) featuring diverse building elements: glass, white-faced hardboard, concrete, and wood, were selected within the study area. The corresponding Wall Attenuation Factor (WAF) values for these materials were calculated and are presented in Table 5. Three receivers were positioned behind different building elements relative to the Wi-Fi access points to compare the resulting distance estimations, as illustrated in Figure 6.

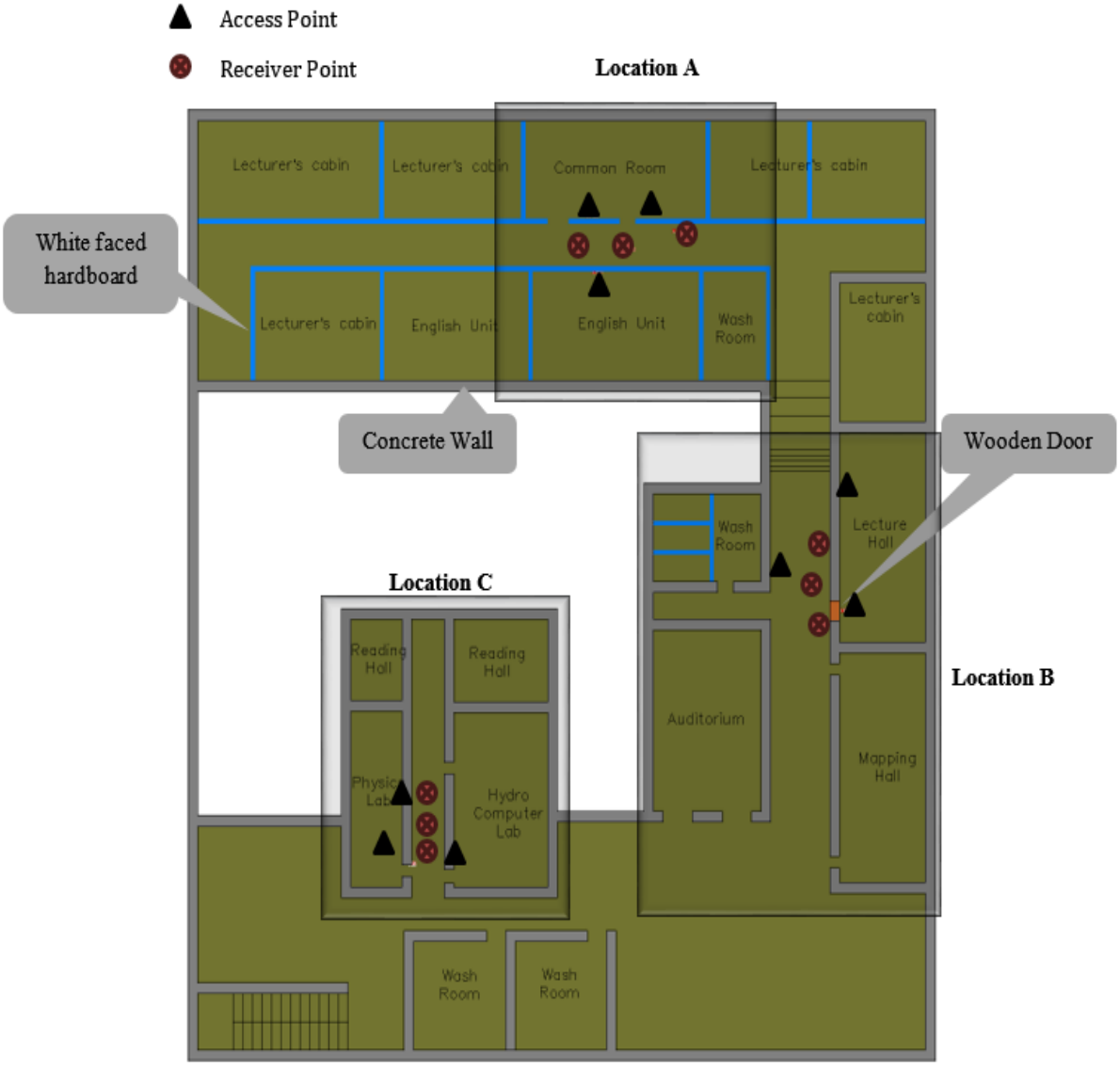

Figure 6. The experimental layout illustrates the faculty floor plan, the placement of different materials at relevant locations, and the positions of access points and receiver points at each location.

Table 5. Calculated WAF values of materials.

Materials	WAF
White Faced Hardboard	-10.4
Concrete wall	-5.1
Glass	-0.4
Wooden Door	-2.8

Initially, the distances were calculated by applying the actual Wall Attenuation Factors (WAF) corresponding to the specific materials encountered along the signal path. For example, at Location A, the WAF for signals from AP1 to R1, R2, and R3 was based on white-faced hardboard, while the WAF for AP2 and AP3 to the same receivers was based on concrete, as illustrated in Figure 6. This approach resulted in a total of nine distance estimations (3 access points x 3 receivers), each utilizing the appropriate WAF for the material in question. The differences between these estimated distances and the actual measured distances were calculated, and the statistical analysis is presented in Table 6. The results demonstrate that the method is capable of achieving sub-meter level accuracy in distance estimation, highlighting the importance of incorporating material-specific WAF values in indoor positioning models.

Table 6. Statistical analysis of the displacement in distance between the Access Point and Receiver after applying the WAF of the material present between them.

		Location A	Location B	Location C
Mean(m)		0.5640	0.2940	0.4213
Std. Deviation(m)		0.6352	0.2510	0.3510
95% Confidence Interval for mean(m)	Lower Bound	0.1490	0.1300	0.1920
	Upper Bound	0.9790	0.4580	0.6510
Range(m)		2.0533	0.6725	1.0287

Subsequently, distances were calculated using a variety of WAF values for each material, regardless of the actual material present along the signal path. This mixing of WAF values simulates arbitrary conditions and demonstrates how distance accuracy varies when incorrect or generalized attenuation factors are used, as illustrated in Figure 6. The estimated distances were then compared with the actual measured distances, and the degree of matching was expressed as a percentage, presented in Table 7. The results reveal that the highest matching percentages occur when the actual WAF values of the

materials are used in the calculations. This confirms that accurate positioning in Wi-Fi-based indoor systems strongly depends on applying the correct material-specific WAF values.

Table 7. The matching percentage between estimated and actual distance values after applying different WAF values. Negative values indicate that the calculated distances are greater than the actual distances.

		From AP1 to (%)			From AP2 to (%)			From AP3 to (%)		
		R1	R2	R3	R1	R2	R3	R1	R2	R3
Location A	Glass	97.3	18.5	-17.3	-25.6	49.6	44.7	73.9	75.8	43.3
	White Faced Hardboard	41	72.5	86.8	90.2	60.1	61.1	50.4	49.6	62.6
	Concrete Wall	66.7	82.1	58.8	53.4	97.7	99.3	81.9	80.7	98.2
	Wooden Door	82.4	54.4	25.7	18.9	79.3	77.4	98.8	99.7	74.3
	Without applying WAF	93.5	11.7	-25.4	22.2	43.9	41.5	69.1	71.1	37.5
Location B	Glass	92.3	93	87.2	66.3	60.5	48.83	31.7	52.2	9.2
	White Faced Hardboard	36.9	42.8	45.1	53.4	55.7	60.4	67.2	59.1	76.2
	Concrete Wall	61.1	70.8	74.7	88.5	92.3	99.9	88.6	97.8	73.7
	Wooden Door	74	85.9	90.5	92.7	88.1	78.7	64.9	81.4	46.9
	Without applying WAF	95.7	89	82.9	61.3	55.3	43.2	25.4	46.6	2.1

Location C	Glass	-62.1	-27.8	-5.5	74.4	-16.6	70.4	-14.3	15.9	-80.3
	White Faced Hardboard	95.3	91	82.1	29.7	86.5	51.8	85.6	73.6	87.9
	Concrete Wall	69.5	86.5	97.6	37	92.2	64.5	93.3	91.7	60.4
	Wooden Door	-10.3	17.3	35.1	59.7	26.2	96	28.1	52.3	-24.9
	Without applying WAF	-12.2	15.5	33.6	77.1	-24.7	65.5	-22.3	9	-90.8

4.4 Repeatability and Robustness of the WAF Model

To evaluate repeatability, WAF-derived distance and position estimates were analyzed across multiple observation points and material configurations. Consistent reductions in both mean error and variance were observed for all tested materials when WAF was applied, indicating that the improvement is not limited to a single access point–receiver geometry. Although the experiments were conducted within a single building, the consistent performance across different materials and spatial configurations suggests that the proposed WAF-based correction is robust under controlled indoor conditions.

4.5 Suitable angle of the antenna

The orientation of the Wi-Fi router can significantly influence the received Wi-Fi signal strength. To identify the most suitable angle that maintains a clear line-of-sight connection to the receiver, an experiment was conducted to observe signal strength variations at different router orientations. The instrumental setup used for this test is shown in Figure 7, while Figure 8 illustrates the variation in signal strength with respect to both distance and router orientation angle. These observations help in determining the optimal router alignment for improved signal reception and positioning accuracy. θ: the angle measured from perpendicular to the router and the angle increased towards the receiver direction. d: Distance from receiver to Wi-Fi router. The figure represents router antenna angle change towards the signal receiver device.

Figure 7. Instrumental setup for finding Signal Strength variation with distances and receiver angle.

To determine the influence of antenna orientation on the signal strength, the transmitting antenna of the router was turned about the vertical axis in set angular steps. The point at which the antenna was facing the receiver perpendicularly (in the direction of the receiver) was set as the reference direction.

The antenna was tilted in 10-degree increments forward and backwards, with the horizontal orientation held constant using a digital protractor (or manually marked angle scale on a rotating stand). Receivable Signal Strength Indicator (RSSI) was measured at the following distances: 1 m, 2 m, 3 m, 4 m, 5 m, and 6 m at every orientation.

This was done in order to make sure that any variation in signal level was only attributed to the radiation pattern and polarization of the antenna and not to the distance or environmental differences. The received RSSI data was then plotted against the angle and distance to determine the most appropriate antenna orientation that was optimal for receiving the maximum signal. The findings (Figure 8) showed that the signal strength was highest at around 60 degrees, which means that at this angle, there was the most preferable propagation path in indoor settings.

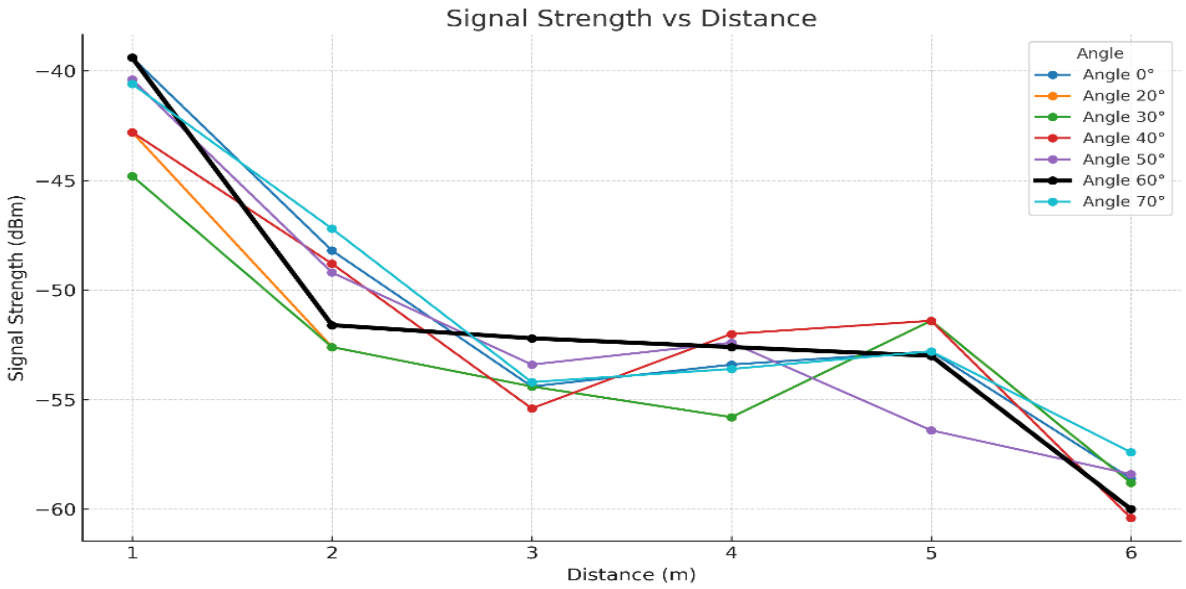

Figure 8. Signal strength changes with the various distances and angles.

According to Figure 8, a clear deviation in signal strength is observed at an angle of 60 degrees. At this orientation, the signal strength remains more stable across varying distances compared to other angles. Therefore, it can be concluded that the optimal angle for the router antenna, in relation to the signal strength measuring device, is 60 degrees from the vertical axis. This orientation provides more consistent signal reception, which is beneficial for accurate distance estimation in Wi-Fi-based positioning systems.

5. LIMITATIONS AND FUTURE WORK

Although this study has been able to show the influence of building materials on the propagation of Wi-Fi signals and positioning accuracy, it has a number of constraints. To begin with, the experiments were performed in one building design and on one floor in an indoor environment. As a result, quantitative evaluation of factors like multi-floor signal propagation and vertical attenuation was not done. Second, the analysis has been conducted with a single type of Wi-Fi router on a fixed transmission power and antenna properties. Various router types, antenna gain, or frequencies (e.g., 5 GHz and 6 GHz bands) might affect the attenuation characteristics and positioning characteristics. Third, the experiments were carried out under a controlled environment, where there was no substantial human movement. In practice, human presence, body blockages and dynamic obstacles may introduce the short-term variations of the signal and multipath effects that were not explicitly modelled in this work. This analysis should be further generalized and confirmed by extending it to multi-floor contexts, mixed router setups, and dynamic conditions with human interactions to achieve further generalization of the suggested WAF-enhanced positioning model.

Direct experimental benchmarking against fingerprinting or deep learning–based IPS methods was not conducted in this study, as such techniques require extensive labeled datasets and site-specific training, which was beyond the scope of this controlled experimental investigation. However, a quantitative comparison with representative results reported in the literature has been included to contextualize the proposed method within the broader IPS research landscape.

6. CONCLUSIONS

This study examined how different building materials affect Wi-Fi signal propagation and indoor positioning accuracy using an LTE wireless router (ZLT S10) and the Airport Utility application. Experiments were conducted in nine locations across three scenarios involving concrete walls, white-faced hardboard, glass, and wooden doors. Signals were measured at 2.5 GHz to reduce reflection errors and improve penetration through barriers.

The Wall Attenuation Factor (WAF) was calculated for each material and position. Without applying WAF, distance accuracy ranged from 1 to 2.5 m. After applying WAF, accuracy improved significantly to 20-50 cm. Coordinate accuracy also improved from X = 0.5-6 m, Y = 1-4 m to X = 10-65 cm, Y =

20-30 cm after applying WAF.

The results clearly show that building materials significantly affect Wi-Fi performance, with concrete walls causing the most attenuation. In contrast, white-faced hardboard and wooden doors had minimal impact. This study demonstrates that incorporating material-specific WAFs can significantly improve Wi-Fi-based distance and position estimation in controlled indoor environments.

Additional experiments were conducted to evaluate the significance of incorporating actual WAF values and ensuring proper router orientation for achieving precise indoor positioning. The results, expressed as matching percentages, clearly indicate that selecting the correct WAF for each building material is crucial for accurate distance estimation. Furthermore, a router orientation of 60 degrees was found to provide optimal and consistent signal strength, reinforcing its importance in enhancing the reliability and performance of Wi-Fi-based indoor positioning systems. However, some errors were caused by signal reflection and interference from nearby people during data recording. The best signal propagation angle was 60 degrees, and optimal accuracy was achieved when the receiver was within 4 meters of the router.

While learning-based IPS techniques may achieve comparable accuracy, they incur significantly higher deployment and maintenance costs. The proposed WAF-based trilateration approach offers a practical trade-off between accuracy, complexity, and deployability, making it well suited for real-world indoor environments where rapid setup and interpretability are required. Finally, this study provides quantitative evidence of the impact of building materials on Wi-Fi signal propagation and positioning accuracy. Future work could explore more materials, higher frequencies, and environmental conditions such as humidity and air density.

REFERENCES

Abulude, F., & Akinnusotu, A. (2015). Global positioning system and it's wide applications. Continental Journal of Information Technology, 9(1), 22–32. https://doi.org/10.5707/cjit.2015.9.1.22.32

Aileen, A., Suwardi, A. D., & Prawiranata, F. (2021). WiFi signal strength degradation over different building materials. Engineering, Mathematics and Computer Science (EMACS) Journal, 3(3), 109–113. https://doi.org/10.21512/emacsjournal.v3i3.7455

Dao, T. K., Nguyen, H. L., Pham, T. T., Castelli, E., Nguyen, V. T., & Nguyen, D. V. (2014). User localization in complex environments by multimodal combination of GPS, WiFi, RFID, and pedometer technologies. The Scientific World Journal, 2014, Article 814538. https://doi.org/10.1155/2014/814538

Dow, J. M., Neilan, R. E., & Rizos, C. (2009). The International GNSS Service in a changing landscape of Global Navigation Satellite Systems. Journal of Geodesy, 83(3–4), 191–198.

Ekahau. (2022, January 12). Wi-Fi design best practices [2022 Guide]. Ekahau. https://www.ekahau.com/blog/wi-fi-design-best-practices/

El Ashry, A. E. M., & Sheta, B. I. (2019). Wi-Fi based indoor localization using trilateration and fingerprinting methods. IOP Conference Series: Materials Science and Engineering, 610(1), Article 012072. https://doi.org/10.1088/1757-899X/610/1/012072

Farid, Z., Nordin, R., & Ismail, M. (2013). Recent advances in wireless indoor localization techniques and system. Journal of Computer Networks and Communications, 2013, Article 185138. https://doi.org/10.1155/2013/185138

He, S., & Chan, S. H. G. (2015). Wi-Fi fingerprint-based indoor positioning: Recent advances and comparisons. IEEE Communications Surveys & Tutorials, 17(1), 466–490.

Hernández, N., Parra, I., Corrales, H., Izquierdo, R., Ballardini, A. L., Salinas, C., & García, I. (2021). WiFiNet: WiFi-based indoor localisation using CNNs. Expert Systems with Applications, 177, Article 114906. https://doi.org/10.1016/j.eswa.2021.114906

Jumaat, N. S. C., Wahab, N. H. A., Sunar, N., Ariffin, S. H. S., Wong, K. Y., & Aun, Y. (2022). Indoor positioning system: A review. International Journal of Advanced Computer Science and Applications, 13(6), 949–960. https://doi.org/10.14569/ijacsa.2022.0130659

Kang, W., Nam, S., Han, Y., & Lee, S. (2012). Improved heading estimation for smartphone-based indoor positioning systems. 2012 IEEE 23rd International Symposium on Personal, Indoor and Mobile Radio Communications (PIMRC), 2449–2453. https://doi.org/10.1109/PIMRC.2012.6362768

Latif, S., Li, B., & Memon, A. (2011). D-Model: A new perspective for modeling radio signal propagation in indoor environment. Australian Journal of Basic and Applied Sciences, 5(7), 405–413.

Liu, H., Darabi, H., Banerjee, P., & Liu, J. (2007). Survey of wireless indoor positioning techniques and systems. IEEE Transactions on Systems, Man, and Cybernetics, Part C (Applications and Reviews), 37(6), 1067–1080. https://doi.org/10.1109/TSMCC.2007.905750

Lymberopoulos, D., Liu, J., Yang, X., Choudhury, R. R., Handziski, V., & Sen, S. (2015). A realistic evaluation and comparison of indoor location technologies. Proceedings of the 14th International Conference on Information Processing in Sensor Networks, 178–189. https://doi.org/10.1145/2737095.2737726

Md Din, M., Jamil, N., Maniam, J., & Afendee Mohamed, M. (2018). Indoor positioning: Technology comparison analysis. International Journal of Engineering & Technology, 7(2.14), 133–137. https://doi.org/10.14419/ijet.v7i2.14.12813

Noertjahyana, A., Wijayanto, I. A., & Andjarwirawan, J. (2017). Development of mobile indoor positioning system application using Android and Bluetooth Low Energy with trilateration method. 2017 International Conference on Soft Computing, Intelligent System and Information Technology (ICSIIT), 185–189. https://doi.org/10.1109/ICSIIT.2017.64

Pahlavan, K., Krishnamurthy, P., Hatami, A., Ylianttila, M., Makela, J. P., Pichna, R., & Vallstrom, J. (1998). Handoff in hybrid mobile data networks. IEEE Personal Communications, 5(2), 39–47. https://doi.org/10.1109/98.667414

Pahlavan, K., Li, X., & Mäkelä, J. P. (2002). Indoor geolocation science and technology. IEEE Communications Magazine, 40(2), 112–118. https://doi.org/10.1109/35.983917

Seidel, S. Y., & Rappaport, T. S. (1992). 914 MHz path loss prediction models for indoor wireless communications in multifloored buildings. IEEE Transactions on Antennas and Propagation, 40(2), 207–217. https://doi.org/10.1109/8.127405

Shaji, A., & Sasi, P. (2022). Localized positioning systems using trilateration algorithm. Journal of Pharmaceutical Negative Results, 13(S01), 434–440. https://doi.org/10.47750/pnr.2022.13.s01.62

Siwiak, K. (2001). Ultra-wide band radio: Introducing a new technology. 2001 IEEE Radio and Wireless Conference (RAWCON), 213–216.

Zafari, F., Gkelias, A., & Leung, K. K. (2019). A survey of indoor localization systems and technologies. IEEE Communications Surveys & Tutorials, 21(3), 2568–2599. https://doi.org/10.1109/COMST.2019.2911558

ADVANCES IN GEOMATICS

VOLUME 04 • ISSUE 01 • APRIL 2026
e-ISSN: 3023-4980

ORIGINAL ARTICLE

Submission: 08/01/2026
Accepted: 25/03/2026

ANALYSIS OF SPATIAL AND TEMPORAL CHANGES IN LAND COVER AND LAND USE: THE CASE STUDY OF KOCAELI-KANDIRA

Erhan YILDIRIM[1]* **Özer AKYÜREK[1]**

[1] Department of Geomatics, Engineering Faculty, Kocaeli University, Türkiye.

* Corresponding Author: E. Yıldırım, erhanteias@gmail.com 0009-0002-8055-2229

ABSTRACT

The ability to accurately determine land cover change and the direction of change provides the scientific basis for policy implementation and predictable urban planning, and is one of the most reliable sources of data. The utilisation of cloud-based platforms, such as Google Earth Engine (GEE), facilitates the acquisition of all satellite data monitoring our planet, thereby offering substantial advantages. This facilitates specific or global analyses of each region, enabling such studies to be conducted with minimal effort. This study examines the district of Kandıra in Kocaeli province, which has undergone significant land use transformation in recent years due to increasing pressure from transport, urbanisation, industrialisation for food production and tourism. The amount and spatial character of the transformation in question were analyzed between 2017 and 2024. In this regard, the Random Forest classifier executed on Sentinel-2 satellite images on the Google Earth Engine platform was cross-validated with the Landsat-based LandTrendr time series algorithm. The analysis revealed that 2,503 hectares of agricultural land in the study area had been converted to artificial land. When comparing the results of two different algorithms, the spatial overlap between the methods was calculated as 0.1041 using the Jaccard Similarity Index; the parcel-based details of the classification method and the complementary role of LandTrendr in capturing vegetation damage were revealed. When examining the spatial characteristics of the change, it was determined that new developments were concentrated at an average distance of 727 meters from the Rural Housing Areas designated in the 1/25,000 scale Master Development Plan. This finding proves that the transformation in Kandıra is not a random scattering (leap-frog/outlying), but rather follows a spread model defined in the literature as Edge Expansion, which extends beyond the boundaries of planned rural settlements, and that the pressure of unplanned construction is concentrated on agricultural lands.

Keywords: Land Use/Land Cover Change, LandTrendr, Google Earth Engine, Edge-Expansion, Plan Incompatibility.

Cited As:

Yıldırım, E. & Akyürek, Ö. (2026). Analysis of Spatial and Temporal Changes in Land Cover and Land Use: The Case Study of Kocaeli-Kandıra, Advances in Geomatics, 4(1), 83-105. https://doi.org/10.5281/zenodo.20558376

1. INTRODUCTION

A significant challenge confronting Türkiye in the 21st century pertains to the interplay between demographic mobility and spatial planning, a dynamic that has contributed to the proliferation of unsustainable urbanisation practices. The process defined as the ruralization of cities rather than the urbanization of villagers in the sociological perspective manifests itself in the spatial dimension as infrastructure deficiencies, lack of disaster resilience, and crises in resource management (Kongar, 2002). Especially in metropolitan areas such as Kocaeli, where industry and agriculture are intertwined, this phenomenon manifests itself in the form of distorted urbanization and urban sprawl, with the pressure of unplanned expansion irreversibly intensifying on productive agricultural land. Since traditional mapping methods are insufficient for monitoring the scale of this rapid transformation and the damage to agricultural land, Remote Sensing (RS) technologies and Geographic Information Systems (GIS) have become indispensable tools for accurately detecting large-scale changes in land cover and land use. Indeed, the literature emphasizes that changes in land cover trigger environmental risks associated with rapid urbanization and deforestation (Drummond & Loveland, 2010; Agaton et al., 2016), leading to ecological degradation such as loss of biodiversity (Butt et al., 2015).

Nowadays, satellite imagery, and especially multispectral images that capture data across various electromagnetic spectrum bands, have made it possible to map land cover in great detail on a large scale (Tırmanoğlu et al., 2023; Rogan & Chen, 2004). Satellite imagery reveals surface characteristics that are crucial for numerous studies, including agricultural monitoring, urban planning, and environmental research (Li et al., 2020; Gu et al., 2021). On the other hand, understanding not only the extent of land change but also its formation process (trend) is vital for sustainable planning. Time series algorithms based on the Landsat remote sensing system have been developed to determine whether the pressure on agricultural and forest areas is a sudden break or a gradual deterioration over time. Among these algorithms, Landsat-based Detection of Trends in Disturbance and Recovery (LandTrendr) can model vegetation loss and recovery processes with high accuracy through its annual pixel-based analysis capability (Kennedy et al., 2010).

Traditional remote sensing methods are generally based on comparing images from two different dates and may be insufficient in fully reflecting the historical process and dynamics of change. To overcome this limitation and process large volumes of satellite data more quickly, the cloud-based computing platform Google Earth Engine (GEE) has become a revolutionary tool for researchers in recent years (Gorelick et al., 2017). GEE allows for high-accuracy land cover classification and change detection across large areas thanks to the integration of machine learning algorithms (such as Random Forest) (Ghorbanian et al., 2020).

The literature contains a large number of studies that look at changes in land cover. Griffiths et al. (2013), used the LandTrendr algorithm with high accuracy to determine the transition of all land

cover changes, as well as the change in agricultural land across Europe, in addition to the issue of abandoned deforestation. Huang et al. (2017), used the entire Landsat archive on the GEE platform to map land cover dynamics in a complex metropolitan area such as Beijing, demonstrating the high success and speed of cloud-based algorithms in tracking urban sprawl. Kennedy et al. (2018), used GEE modules developed for the implementation of the LandTrendr algorithm in a cloud-based architecture and for fast execution on large datasets. Nguyen (2020), analyzed land cover change in Vietnam's northwestern region between 2003 and 2010 using Landsat imagery on the GEE platform. In his study, he used the Classification and Regression Tree (CART) classification method to determine land cover classes and provided useful information about land cover change in Dien Bien province and the mechanisms of this change. Chen et al. (2021), examined land use changes in China's Bohai Rim coastal region using long-term time series analyses on the GEE platform. Their analyses highlighted that the greatest loss occurred in agricultural areas. They found that the land cover lost from agricultural areas was mostly converted into residential areas, cities, and port structures. Pande (2022), analyzed land use/cover changes in India's Rahuri watershed area using GEE. Using Landsat and Sentinel satellite imagery, he analyzed land use/land cover values for the years 2010, 2015, and 2020 on the GEE platform using the Random Forest classification method. As a result of his analyses, he determined the amount of change for each land cover/land use class. Teja et al. (2024), studied changes in land cover/use in India's Telangana state between 2002 and 2015 using Landsat-7 and Sentinel-2 imagery via the GEE cloud platform. Okoduwa and Amaechi (2024), used the GIS and GEE platform to analyze land cover changes in Nigeria's Abuja region. Using Landsat-8 remote sensing images, they classified land classes with 92% overall accuracy using a Random Forest classification algorithm, identifying land cover/use changes between 2014 and 2023.

This study aims to examine the loss of forest and agricultural land in the Kandıra district of Kocaeli province using a multidimensional approach. The study primarily aims to analyze remote sensing images and the LandTrendr algorithm to determine the temporal change in forest and agricultural areas within the Kandıra district. Afterwards, based on the principle that the spatial distribution of land change is not random, but rather that nearby objects are more related, as stated in Tobler's First Law of Geography, the spatial dependency of change on distance from existing settlement centers was analyzed. In this context, whether urban growth exhibits the characteristic of Edge Expansion has been tested using the approaches proposed by Li and Yeh (2004). In order to systematically characterize this spatial dependency, the urban growth typology proposed by Li and Yeh (2004) provides a foundational framework. Li and Yeh (2004) proposed a conceptual framework for understanding urban expansion, distinguishing between three distinct spatial patterns: infilling, edge-expansion, and leapfrog development. These patterns were based on the topological relationship between newly developed patches and existing urban boundaries. The integration of this conceptual approach is of crucial importance to the present study, since it formally determines whether the loss of agricultural land in Kandıra is driven by contiguous outward growth from existing villages (edge-expansion) or

by fragmented, disconnected sprawl (leapfrog). The study aims to reveal the spatial and temporal dynamics of rural-urban transformation in the case of Kandıra by using Sentinel-2 and Landsat data with a hybrid methodology.

2. MATERIALS AND METHODS

The materials and methods used in the study are described in this section. The workflow methodology created for the implementation of all these methods is shown in Figure 1.

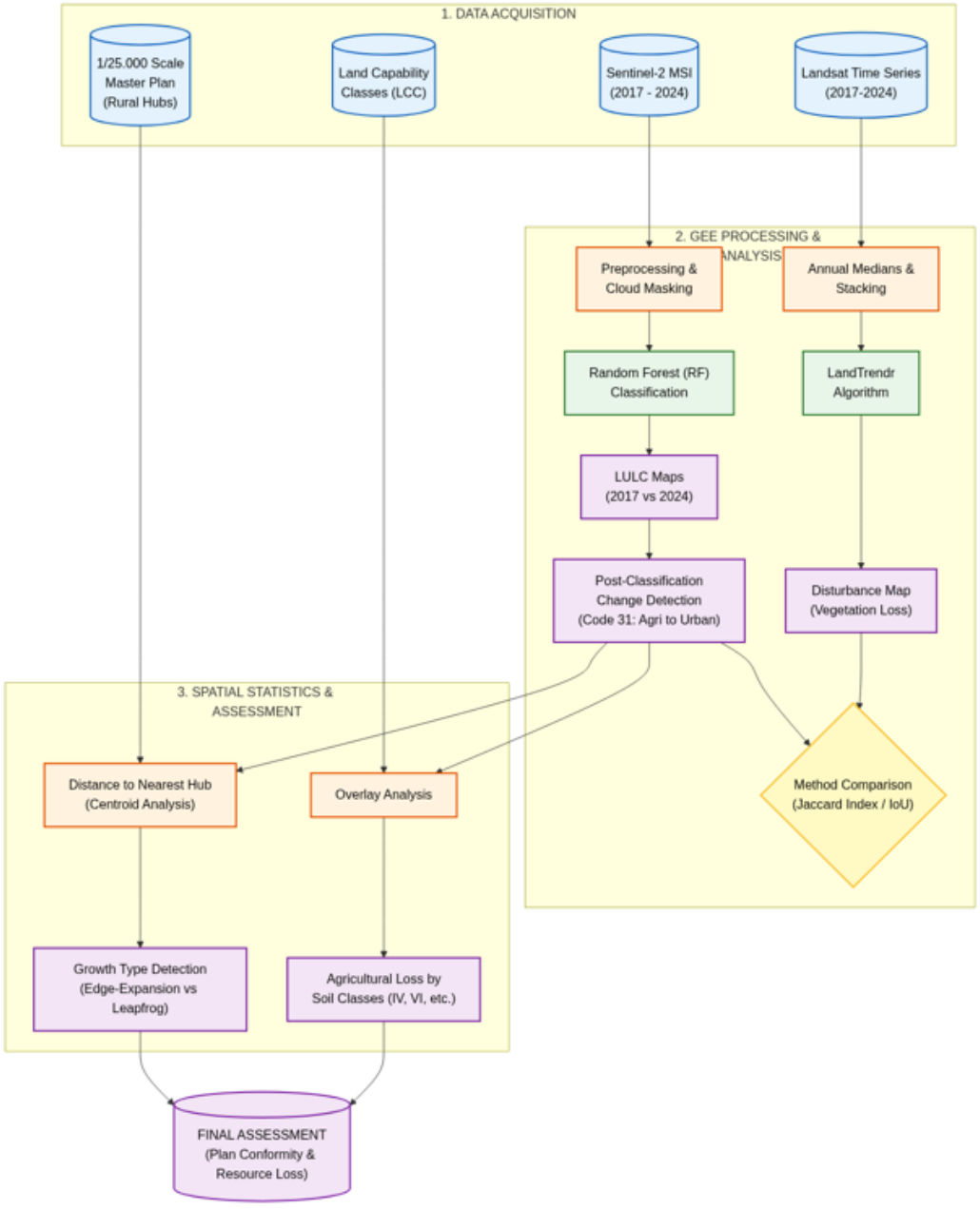

Figure 1. Workflow methodology for the study.

2.1 Study Area

Kandıra, the district with the largest agricultural area in Kocaeli Province, was selected as the study area for this study (Figure 2). Kandıra is located in the northeast of Kocaeli and is the largest district in the province with an area of 933 km2. The district, located on the Black Sea coast, stands out for its fertile agricultural lands and natural beauty. The district's geographical coordinates range between 41° 04' N and 30° 09' E. The elevation of the district center above sea level is 75 meters. The district's climate is impacted by the climate of the Western Black Sea and Marmara regions. While it does not have a stable climate, it exhibits transitional climate characteristics. Rainfall in summer is generally irregular. Winters are generally not very cold, with rainfall mostly in the form of rain and little snowfall. Forests stretching along the coastline cover a significant area of the district (Kandıra District Governor's Office, 2025).

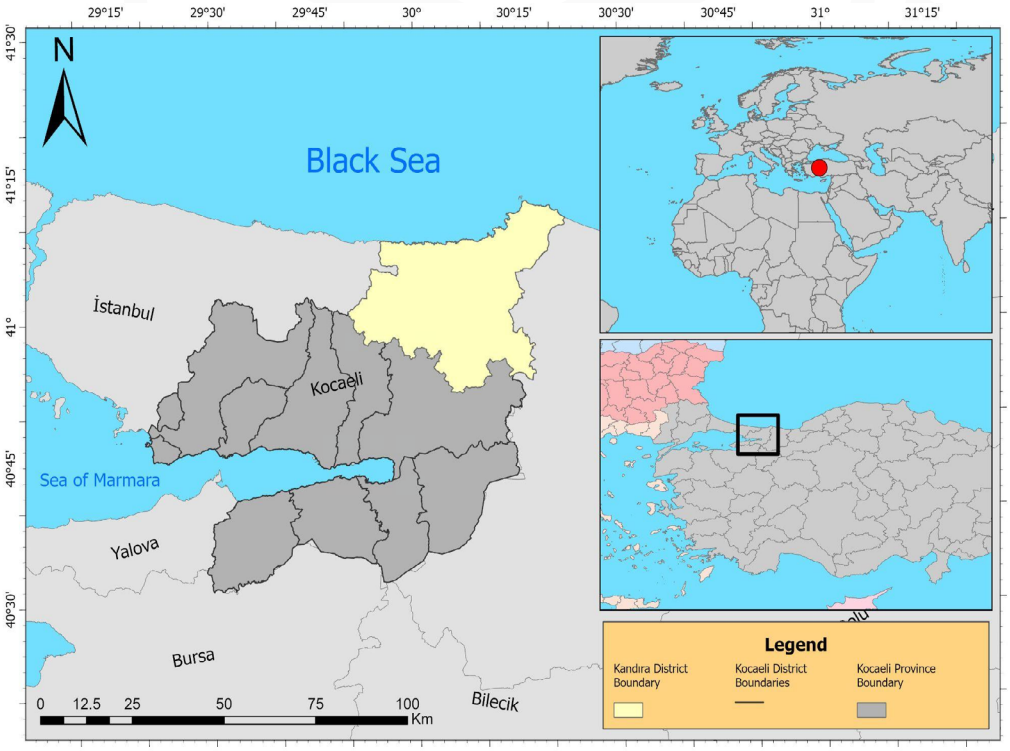

Figure 2. Study area.

2.2 Datasets

In this study, remote sensing data and spatial planning data were integrated to monitor land use dynamics in the Kandıra district and analyze trends in unplanned construction. European Space Agency (ESA) Sentinel-2 MSI satellite multispectral image bands ('B2', 'B3', 'B4', 'B8', 'B11', 'B12' and three widely used spectral indices were calculated and added to the model as independent variables: NDVI, NDWI, NDBI; spatial texture metrics were not included) were used to monitor changes in the study area during the 2017–2024 period. These data, with a spatial resolution of 10 meters, were processed

on the GEE platform and formed the basis for Random Forest classification. Images were filtered for the summer season and cloud masking was applied using the QA60 band. Landsat 8 satellite images were used to verify land change trends from a long-term perspective. These data were evaluated using the LandTrendr algorithm to model the historical process of vegetation loss. To determine the agricultural nature of areas undergoing transformation, Land Capability Classes (LCC) maps were obtained from the Ministry of Agriculture and Forestry database. This dataset has been used to determine whether areas removed from agriculture are absolute agricultural land. The 1/25,000 scale Master Development Plan data, approved by the Kocaeli Metropolitan Municipality, was also used to define the legal and planned settlements in the working area. The boundaries designated as Rural Residential Areas under the plan have been accepted as Reference Centers (Hubs) in spatial analyses. Any development identified outside these boundaries has been assessed as potential Degradation/ Unplanned Development.

2.3 Methods

A multi-stage methodology was followed to identify changes in land cover/use in the study area and to analyze the spatial dynamics driving these changes. The first stage involved GEE-based image processing and time series analysis, followed by change detection and validation, spatial statistical analyses, and finally land suitability/proximity analyses. The processing of large-scale Sentinel-2 and Landsat satellite image collections, the creation of annual image composites, and the execution of the LandTrendr algorithm were carried out using the cloud-based Google Earth Engine (GEE) platform and ArcGIS Pro software, respectively. To ensure a rigorous accuracy assessment, reference validation samples were collected completely independent of the training dataset, preventing any potential data leakage. Ground truth reference data for both training and validation areas were derived from high-resolution orthophotos for the year 2017, and from high-resolution Google Earth imagery for the year 2024. This multi-source verification confirms the high reliability of the classification results. The final adjustments to the change maps, spatial statistical calculations, and map designs were performed using QGIS v3.40 desktop software. All spatial data and analysis outputs have been standardized in the WGS84 / UTM Zone 35N (EPSG: 32635) coordinate system for areal and positional accuracy, in accordance with the geographical location of Kocaeli province.

A Distance to Nearest Hub analysis was applied to determine the spatial pattern of land conversion. In this context, the Euclidean distance between each pixel converted from agriculture to artificial land between 2017 and 2024 and the centroid of the nearest village or neighborhood settlement area was calculated. The frequency distribution (histogram) and measures of central tendency (mean and median) of the obtained distance values were used to determine whether the growth type was Leapfrog or Edge-Expansion.

The Jaccard Similarity Index (Intersection over Union - IoU) was used to determine the spatial overlap

level between the results of the Sentinel-2-based classification (Random Forest) and the Landsat-based time series (LandTrendr) analyses applied in the study. In computer vision and image processing literature, IoU is preferred as a standard metric for measuring object detection and segmentation performance, particularly because it does not include unchanged background areas (True Negatives) in the success criterion (Szeliski, 2022).

$$IoU = \frac{Area\ of\ Intersection}{Area\ of\ Union} \quad (1)$$

In this regard, the index calculated by dividing the intersection area of the change maps produced by two different algorithms using Equation (1) by the union area was used to reveal the extent to which the methods validate or complement each other.

2.3.1. Remote Sensing and Time Series Analysis

The analysis process was initiated by processing Sentinel-2 satellite images on the GEE cloud platform. Cloud masking and atmospheric correction processes were applied to the image collection covering the 7-year period between 2017 and 2024, and median composite images best representing the study area for each year were produced.

The processing of Sentinel-2 satellite imagery is a rigorous workflow designed to transform raw Top-Of-Atmosphere (TOA) data into scientifically viable Surface Reflectance (SR) products, which is a fundamental step for ensuring that temporal analyses are based on actual land surface changes rather than atmospheric artifacts. The primary objective of atmospheric correction is to eliminate the scattering and absorption effects caused by atmospheric gases and aerosols, typically achieved through the Sen2Cor processor. This process utilizes the libRadtran radiative transfer model to create Look-Up Tables (LUTs) that account for varying conditions of water vapor, ozone, and aerosol optical depth. By applying these corrections, the imagery is converted from Level-1C (TOA) to Level-2A (Bottom-of-Atmosphere) reflectance, ensuring the data represents the true physical properties of the Earth's surface, while also utilizing the 1.375μm band to compensate for thin cirrus clouds that often elude standard detection methods. Accurate cloud and shadow detection serves as a critical prerequisite for any automated remote sensing pipeline, primarily managed through the Scene Classification Algorithm (SCA). This algorithm categorizes pixels based on multi-spectral thresholds, particularly focusing on high reflectance in the blue and short-wave infrared (SWIR) regions, while simultaneously projecting cloud shadows geometrically based on solar azimuth and elevation angles to generate high-quality Quality Indicators. While the standard SCL provides robust baseline classifications, researchers frequently augment this process with advanced machine learning approaches, such as the s2cloudless algorithm, which utilizes gradient-boosted trees to achieve superior precision in complex or heterogeneous landscapes.

To improve classification accuracy and eliminate erroneous change signals caused by phenological

changes, the LandTrendr algorithm, which performs pixel-based spectral trend analysis, was adapted and applied to the dataset created from Landsat satellite images. This algorithm examined the thirteen-year spectral trajectories of pixels, considering only areas showing statistically significant disturbance as real changes.

LandTrendr (Kennedy et al., 2010) is a remote sensing-based spectral-temporal segmentation algorithm designed to detect both abrupt and gradual land cover changes by analyzing Landsat satellite image time series through piecewise linear models. The operational mechanism begins with the generation of annual spectral index composites, such as NBR or NDVI, followed by a despiking process to filter noise and the identification of key vertices that represent significant breakpoints in the spectral trajectory. Mathematically, the algorithm fits an optimal piecewise continuous linear regression to the time series, defined as

$$\hat{y}_t = \beta_{0,j} + \beta_{1,j} t + \varepsilon_t \quad (2)$$

for each segment j, while maintaining a continuity constraint at each intersection point (tv) such that $\beta_{0,j} + \beta_{1,j} t_y = \beta_{0,j+1} + \beta_{1,j+1} t_y$. By utilizing Ordinary Least Squares (OLS) to minimize the Sum of Squared Errors (SSE), LandTrendr iteratively simplifies complex models by removing weak vertices and evaluating statistical significance via an F-statistic. This reduction process adheres to the principle of Occam's Razor, ultimately selecting the simplest model that meets user-defined p-value thresholds to accurately represent the temporal evolution of the landscape.

Table 1. The key control parameters used for the Landtrendr algorithm.

Parameter	Value
Maximum Number of Segments	5
Vertex Count Overshoot Threshold	2
Spike Threshold	0.9
Recovery Threshold	0.25
P–Value Threshold	0.01
Best Model Proportion	1.25
Minimum Number of Obsevation	6

In order to guarantee complete transparency and the possibility of reproduction of the time-series analysis, the specific control parameters configured for the LandTrendr algorithm are detailed in Table 1. Furthermore, the temporal segmentation process is illustrated by Figure 7, which provides a schematic representation of a pixel's spectral trajectory. This demonstration shows how the algorithm filters out inter-annual noise (cloud masking and phenology differences) in order to identify permanent structural disturbances (breakpoints).

2.3.2. Change Detection

The study identified land cover transitions between 2017 and 2024 by applying the Raster Differencing method to time series data created from remote sensing images. Using the transition matrix created at this stage, the conversion from agricultural to urban areas, the loss of forest areas, and changes in water surfaces were calculated spatially and proportionally. In the Post-Classification Comparison phase, the Pixel-Based Coding method was applied to determine the direction and character of transitions between classes.

In this method, a new Change Raster was generated using the following formula, where the T2017 class values for the starting year are represented in the tens place and the T2024 class values for the ending year are represented in the ones place.

$$D_{pixel} = (S_{2017} * 10) + S_{2024} \quad (3)$$

Here, S_{2017} defines the land cover class value for 2017 (Class code: 3 (Agricultural Areas)), while S_{2024} defines the land cover class value for 2024 (Class code: 1 (Artificial Areas)). The matrix values obtained as a result of this process indicate that a pixel with code '31', which was Agriculture (3) in 2017, has been converted to Artificial Area (1) in 2024. Since the focus of the study is agricultural land loss, the analyses were specifically conducted on pixels with code '31'.

2.3.3. Spatial Characteristics and Edge Expansion Analysis

In classifying expansion types, the conceptual framework of the Landscape Expansion Index (LEI) developed by Liu et al. (2010), which is accepted as the fundamental reference in the literature, has been applied. A Distance to Nearest Hub analysis was performed using the QGIS program to determine the spatial distribution pattern and type of expansion of the identified urban transformation and land losses.

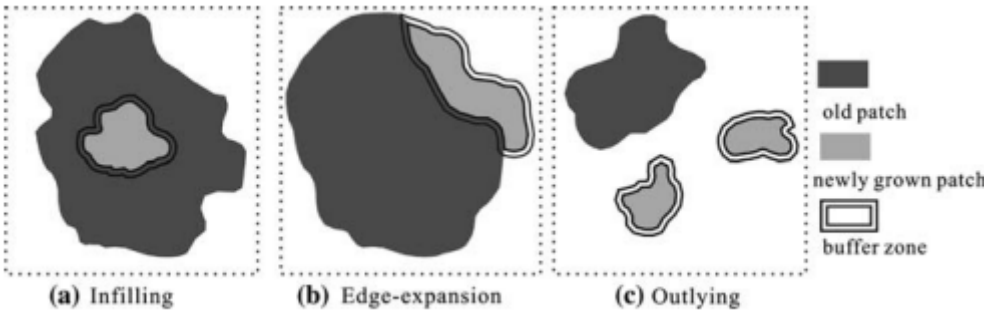

Figure 3. Types of land cover growth (Liu et al., 2010).

In this analysis, unlike traditional methods, the aim is to measure plan-discrepancy. Within this scope, the geometric centers (centroids) of polygons designated as Rural Residential Areas in the 1:25000 scale Master Development Plan data have been accepted as reference points (hubs). If the new de-

velopment area shares more than 50% of its boundary with the existing urban fabric, it is defined as infill development. If it shares between 0% and 50%, it is defined as edge expansion. If there is no shared boundary and the development is isolated, it is defined as leapfrog or outlying development.

In this study, the topological relationships in question were interpreted using a distance-based approach, and statistics (mean and median distance) were obtained by calculating the Euclidean distances of each pixel converted from agricultural to artificial land to these reference points. These statistics were used to determine whether the dominant growth characteristic in the region indicated a theoretically defined Jumping structure or Edge Expansion adjacent to existing plan boundaries (Figure 3). The threshold values used in the study were set as follows: infilling if the LEI index value is between $50 < LEI \leq 100$, Edge-Expansion if $0 < LEI \leq 50$, and Outlying (or leapfrog) if the LEI value is equal to 0.

2.3.4. Land Capability and Quality Analysis

Overlay analyses were performed to examine the physical nature of the change and the extent of agricultural loss. The productivity status of areas converted from agricultural use was determined by analyzing a change raster. This was done by overlaying it with digital data showing the Land Capability Classes belonging to the Ministry of Agriculture and Forestry. The pixels where loss or conversion occurred were then identified. As a result of this process, the proportion and area of land converted to Absolute Agricultural Land (Class I and II) and Marginal Agricultural Land have been calculated.

3. RESULTS

This section presents the results of hybrid analysis obtained using Sentinel-2 and Landsat satellite images under the headings of spatial change amount, comparison of methods, spatial characteristics of change, and relationship with land capability classes.

3.1. Basic Change Statistics and Method Comparison

The Random Forest classification method on the GEE platform with 100 decision trees was used to classify Sentinel-2 images from 2017 and 2024. The classification process was analyzed for accuracy, and the overall accuracy was determined to be 99.01%, 95.04%, and the kappa statistic was 0.98 and 0.89, respectively. The image difference detection method was used to identify changing classes within the time period, and areas that changed over the years were detected based on pixel changes. The difference image obtained as a result of the change detection process is shown in Figure 4.

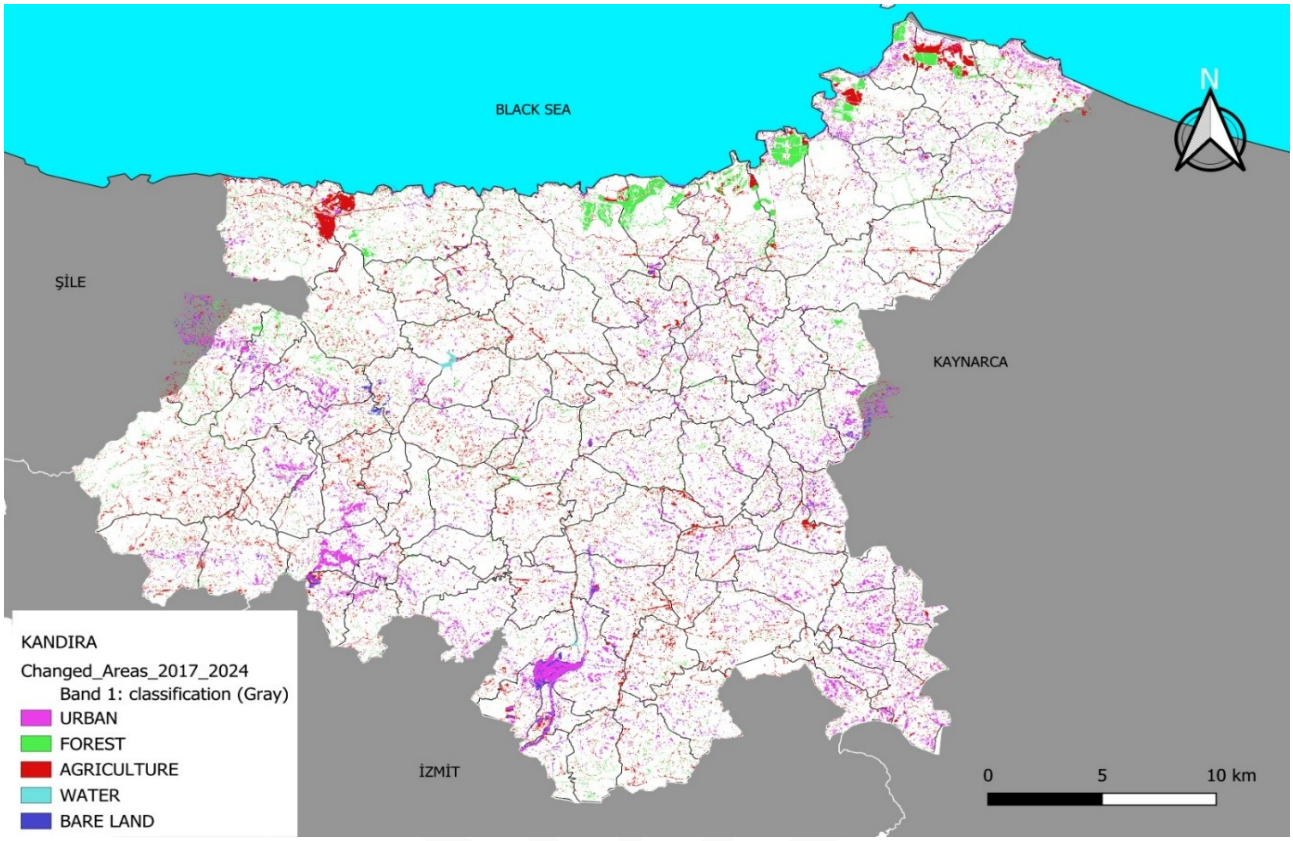

Figure 4. Changes in land cover/land use between 2017 and 2024.

Analyses covering the period 2017-2024 revealed that a total of 2,503 hectares (approximately 250,300 pixels) of agricultural land in the study area lost its character and was converted into artificial surfaces. This amount corresponds to approximately 2.6% of the agricultural land in the Kandıra district. When examining the soil quality of the 2,503 hectares of land converted to non-agricultural use, it was observed that urban pressure was concentrated on low-yield agricultural land and medium-quality land. Distribution of change according to Land Capability classes the Marginal Agricultural Land class accounted for 50.7% of the total loss, making it the class that experienced the most intense conversion. This situation shows that development is shifting to the least resistant areas, taking into account the cost/efficiency balance. The Medium-Quality Land class accounts for 25.0% of the total loss. The uncertainty surrounding their protection status has left these lands vulnerable to development pressure. The share of Absolute Agricultural Land in the total conversion rate remained at 9.7% (Class I: 2.9%, Class II: 6.8%). This low rate indicates that the protective measures under Law No. 5403 have had a partial effect on absolute agricultural lands.

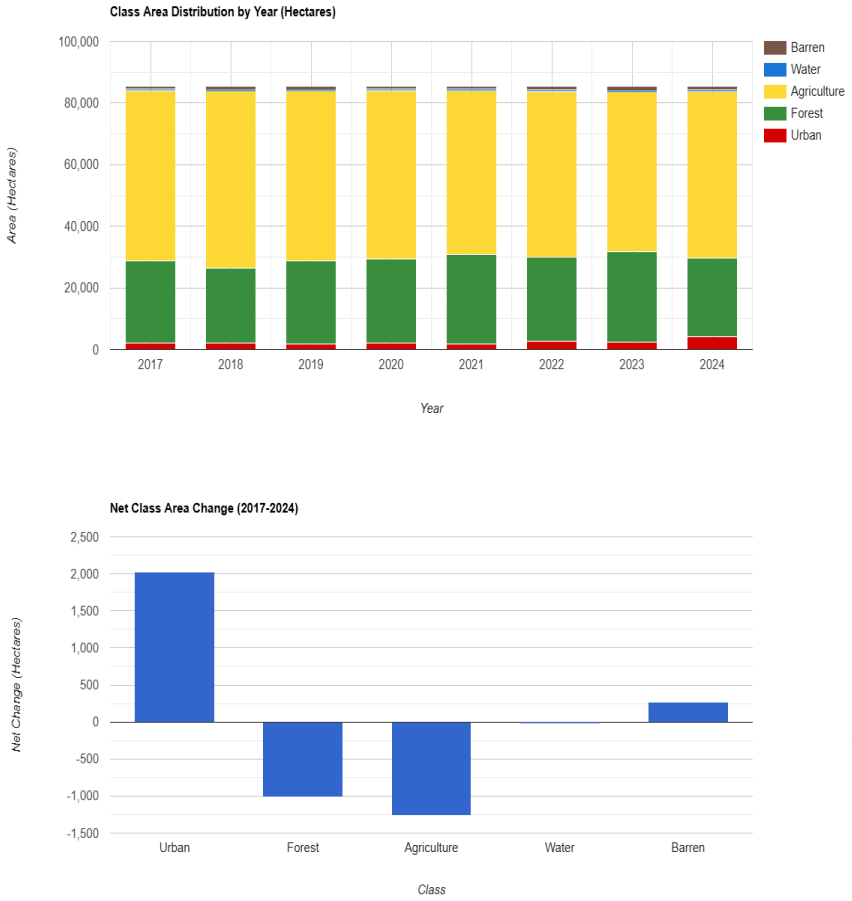

Figure 5. Changes in class area by year (top) and net changes in class area within years (bottom).

Figure 5 shows the significant changes between land cover classes in the study area during the 2017-2024 period. According to statistical calculations, the urban area, which was 2,065 hectares at the beginning of 2017, reached 4,179 hectares by 2024, indicating a net increase of 2,114 hectares (102.3%) in urban areas over a 7-year period. When examining the agricultural areas that form the main character of the region, it is seen that the agricultural land, which was 55,357 hectares in 2017, decreased to 53,897 hectares in 2024, resulting in a net loss of 1,459 hectares. Figure 4 also clearly shows that urbanization pressure is particularly evident in certain areas, especially in relation to the expansion of the Food Specialized Industrial Zone and the Kandıra-İzmit transportation route. Similarly, a decrease of approximately 970 hectares was observed in forest areas, with forest cover falling from 26,577 hectares to 25,607 hectares. However, interpreting changes in land cover solely based on net differences does not fully reflect the actual transformation parameters in the area. Analysis of the transition matrix created as a result of the classification reveals that the pressure of urbanization on agricultural areas is greater than the net change statistics indicate. The analysis results show that the 2,503-hectare area classified as agricultural land in 2017 will be converted into artificial areas by the end of 2024. According to these findings, the reason why the net agricultural loss reflected in the

statistics (1,459 ha) appears lower is understood to be a result of it being offset by partial transitions to agriculture from other classes (especially forest areas). Furthermore, the transition matrix created as a result of classification and change analysis demonstrates that the permanent conversion resulted in a gross loss of 2,503 hectares from agriculture to construction.

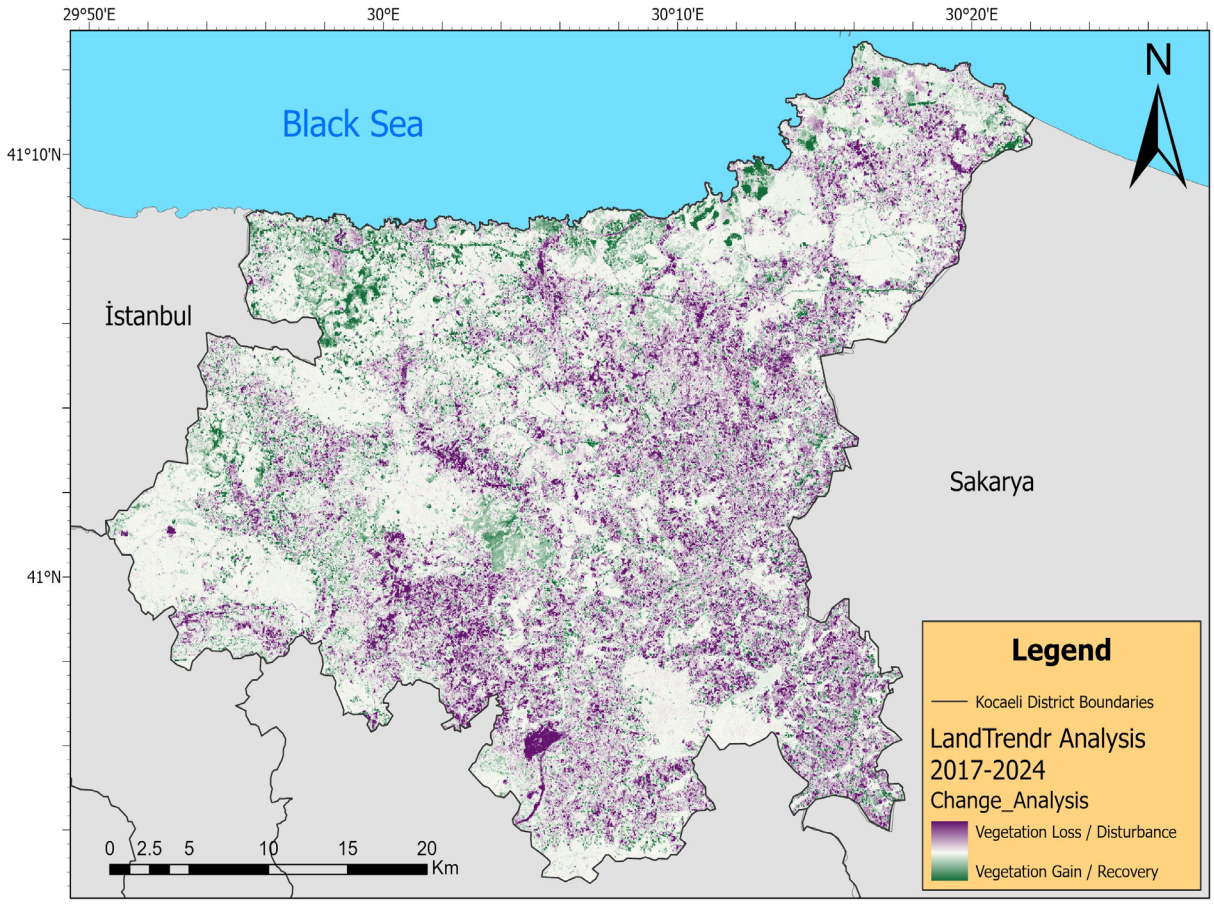

Figure 6. 2017 - 2024 Landtrendr analysis results for the study area.

The displayed values represent the spectral index difference (magnitude of change) and are unitless. Negative values (green areas) indicate vegetation growth or recovery, while positive values (purple areas) indicate a decrease in vegetation cover (disturbance or conversion to artificial surfaces).

The image obtained using the Landtrendr algorithm with Landsat 8 images from 2017 to 2024 is shown in Figure 6. The areas shown in purple in the figure represent the areas that have undergone change over time. Figure 7 shows the changes and graph related to the Food Organized Industrial Zone and highway construction carried out within the Kandıra district in more detail. Figure 7 shows that a steady change in area has occurred over the years due to construction in the area shown in the black frame. It can be seen that the land cover areas in this region have changed over time and turned into urban areas. The descriptive outputs of LandTrendr are quantitatively supported by the

Random Forest post-classification transition matrix (Table 2). According to the cross-tabulation results between 2017 and 2024, exactly 2,503 hectares of agricultural land were directly converted into artificial surfaces, verifying the observed spectral disturbances.

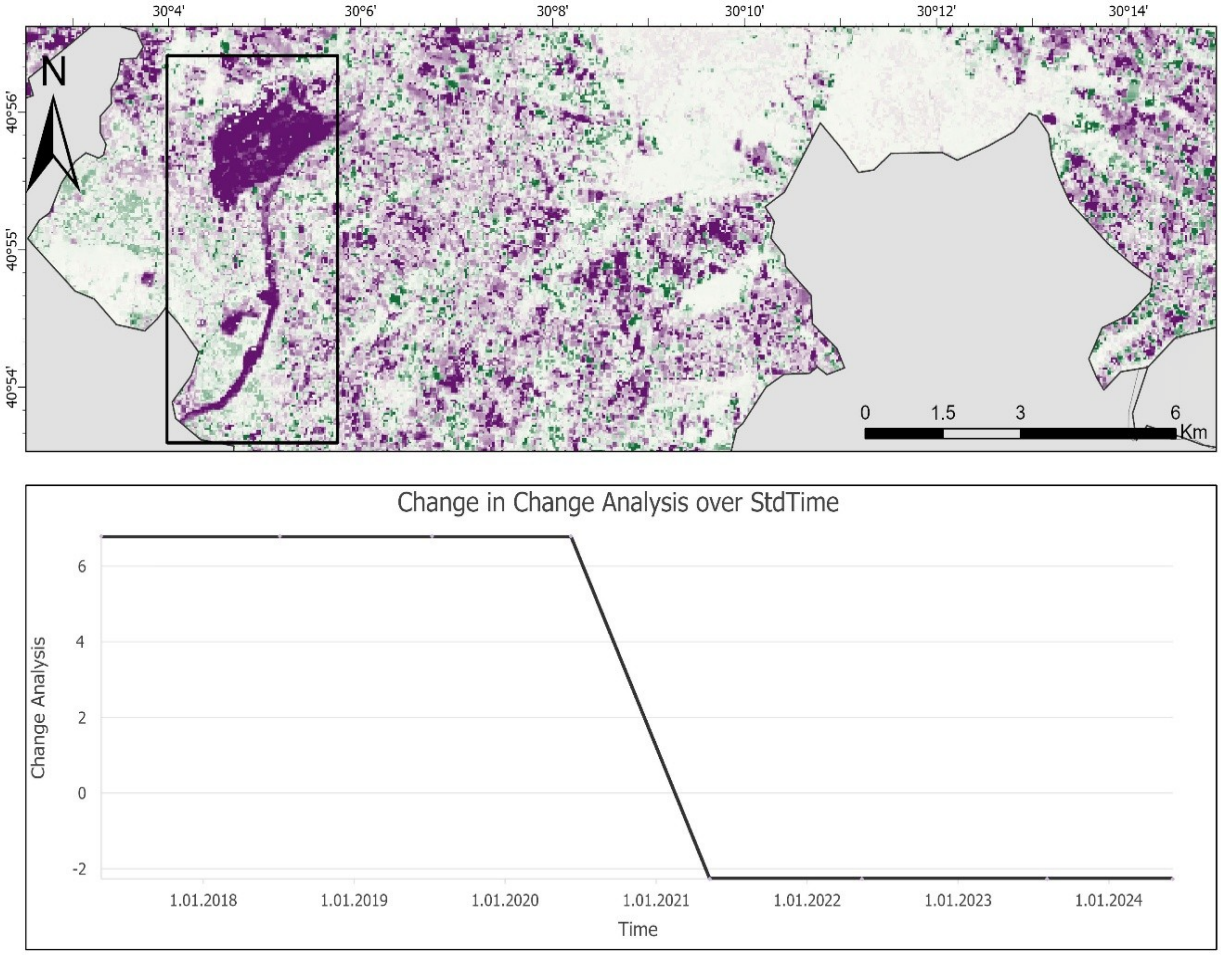

Figure 7. The change in a region within the study area over the years (transition from forest cover to urban).

Rather than establishing direct causality, a strong spatiotemporal correlation is observed. The breakpoints detected heavily after 2021 spatially and temporally coincide with the accelerated construction phases of major regional transportation infrastructures, such as the Izmit-Kandıra highway project and Kandıra Food Organized Industrial Zone (Güneş, 2022; KGM, 2022; Oktay, 2019).

When examining the annual change graphs (trajectory analysis) obtained with the LandTrendr algorithm, it was observed that vegetation loss (disturbance) did not follow a linear trajectory. The increase in breakpoints identified particularly in 2021 and beyond shows a temporal overlap with the construction processes of transportation projects (road widening and connecting roads) in the region. This finding reveals that land cover change is accelerated not only by housing demand but also by the triggering effect of large-scale infrastructure investments. When comparing the performance of

two different algorithms, Random Forest and LandTrendr, the spatial overlap level between Sentinel-2-based classification and Landsat-based time series analysis was calculated as a Jaccard Similarity Index of 10.41%. This coefficient reveals the spatial complexity of the transformation.

Table 2. Transition matrix of Random Forest classification.

2017 Class (From) \ 2024 Class (To)	Artificial Surfaces	Forest	Agriculture	Water Bodies	Barren Land	Total 2017
Artificial Surfaces	1,261.93	18.80	547.58	5.40	119.76	1,953.46
Forest	38.26	23,290.97	3,087.99	3.59	37.85	26,458.70
Agriculture	2,503.02	2,104.01	50,505.73	28.26	576.89	55,717.90
Water Bodies	19.96	10.34	27.05	428.36	8.46	494.17
Barren Land	217.78	1.69	302.73	2.44	333.92	858.57
Total 2024	4,040.96	25,425.80	54,471.10	468.05	1,076.88	85,482.80

3.2. Spatial Distribution and Edge-Expansion

Secondly, the study analyzed the spatial distribution of changes in land cover. This analysis used LEI index values. When examining the spatial distribution pattern of areas transformed from agriculture to urban areas, it has been determined that the change does not exhibit random sprawl. The distances of conversion pixels to rural settlement centers (Hubs) were analyzed in the 1/25,000 scale Master Development Plan. The average distance was found to be 727 meters, while the median distance was 605 meters. The median value being lower than the average and the histogram clustering in the 0-1000 meter band statistically proves that new developments are not disconnected (leap-frog) from existing planned settlement areas, but rather spread by attaching to the peripheries of existing villages through the Edge-Expansion model.

The primary objective of the analysis is to determine whether the transformation occurred as leap-frog development independent of existing settlement areas, or as edge expansion adjacent to the existing fabric. First, the centroid of each pixel in the areas converted from agricultural land was created. Areas designated as rural residential areas in the 1/25000 scale Master Development Plan were also assumed to be hubs, and their centers of weight were determined pointwise and assigned as hub references. The Euclidean distance of each pixel converted from agriculture to urban was calculated to the nearest center (hub), and the median and mean of each distance total were calculated to find the central tendency, and the spread characteristic of the change was interpreted (Figure 8).

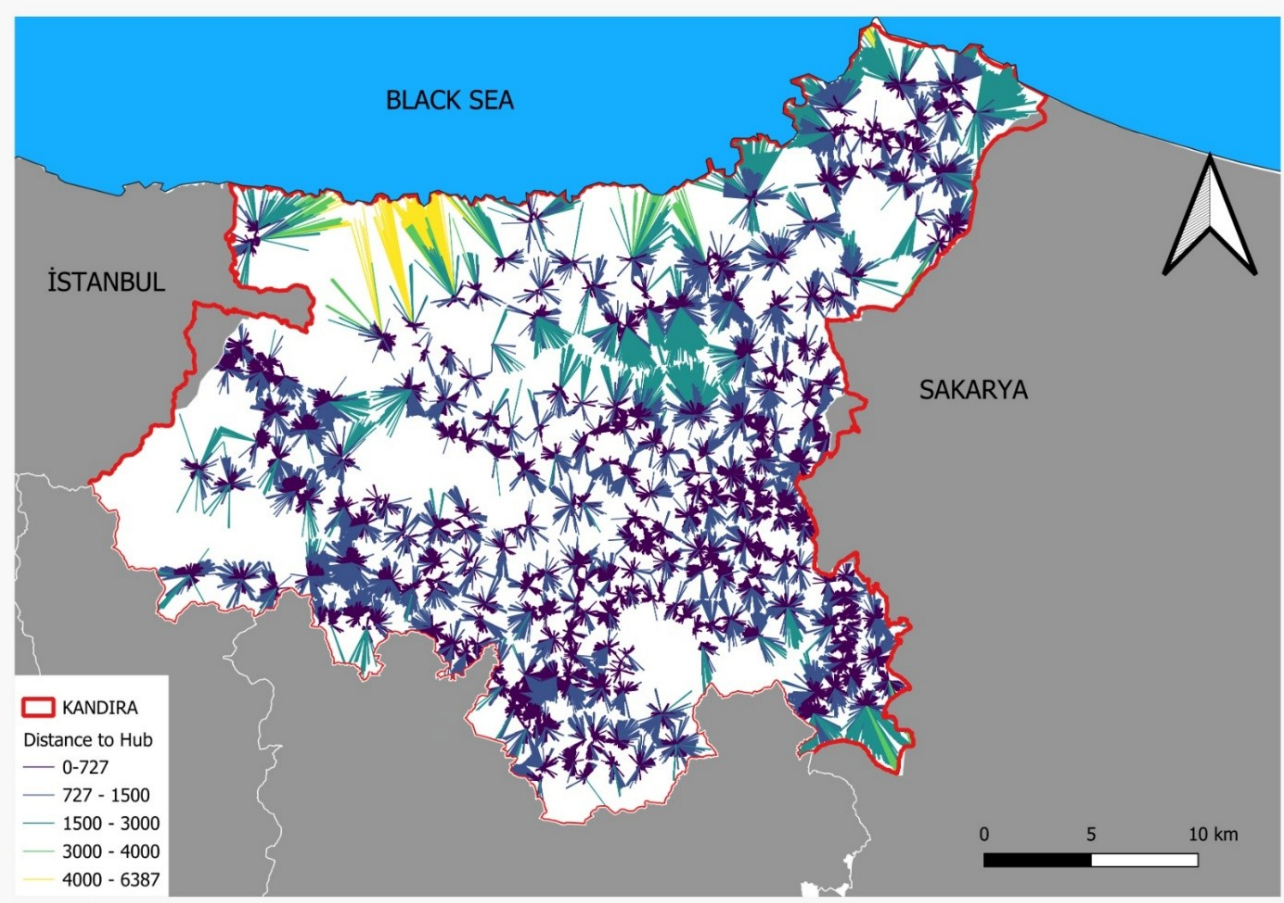

Figure 8. Land use/cover changes' spatial distribution.

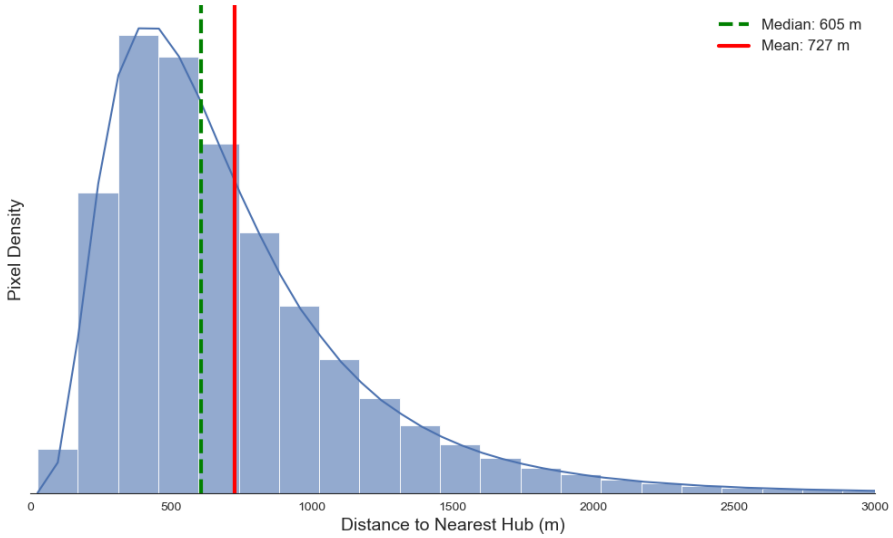

Figure 9. Distribution of distance from settlement centers to areas converted from agriculture to artificial land.

When examining Figure 8, it can be seen that the transition points indicated in dark blue (0-727 m) are particularly concentrated around residential areas. Examining the resulting histogram (Figure 9) revealed that the turning points accumulated around 605 meters and remained below the overall average value. The histogram in Figure 9 also supports this visual observation, showing that more than 60% of the conversion took place within a perimeter of 600-700 meters, which can be considered walking distance to the settlement center. It has been concluded that this loss of agricultural land has occurred in accessible agricultural areas immediately adjacent to planned rural settlements, and that urbanization tends to spread organically outward from existing centers.

The study examined the spatial distribution of areas converted from agricultural land to urban areas using the Landscape Expansion Index (LEI) as a reference (Figure 10). The topological computation revealed a highly fragmented transition pattern across the total 2,549.09 hectares of converted land. Edge-Expansion represents the largest proportion by area, accounting for 1,299.49 hectares (10,548 patches), indicating that a significant portion of the growth physically attaches to existing settlements and infrastructure. However, the Leapfrog expansion exhibits a striking pattern of rural fragmentation: although it covers slightly less area (1,098.05 hectares), it comprises the vast majority of individual patches (21,766 patches). This overwhelmingly high number of isolated leapfrog patches quantitatively proves that urbanization dynamics also manifest as thousands of disconnected, dispersed developments scattered across agricultural fields, indicating severe urban sprawl. Infilling represents the smallest proportion (151.55 hectares; 7,214 patches).

Integration of the Topological Landscape Expansion Index (LEI) with analyses of distance from the center demonstrates that significant agricultural loss in the designated area is attributable to the severe and uncontrolled nature of urban sprawl in the region. The findings indicate that Edge Expansion, encompassing 1,299 hectares, is the most predominant growth type in terms of area, suggesting that existing settlements are expanding in an outward direction. Nonetheless, in spite of its extensive coverage of 1,098 hectares, Leapfrog development encountered a substantial number of 21,766 isolated patches, thereby unveiling a pervasive degree of spatial fragmentation that has profoundly penetrated the underlying rural infrastructure. The evidence suggests that the distribution of these isolated artificial surfaces is not random but follows a systematic pattern, with a mean distance from official settlement centers of 727 meters (and a maximum of 6.3 kilometers). This pattern indicates that the phenomenon of leapfrog growth extends far beyond the planned boundaries of urban development. Consequently, the findings of the two analyses indicate with a high degree of clarity that the transformation of land in Kandıra is not limited to the expansion of legal boundaries; on the contrary, this transformation directly threatens the sustainability of agriculture through unplanned urban sprawl that spreads across a multitude of disconnected fragments in the middle of agricultural land.

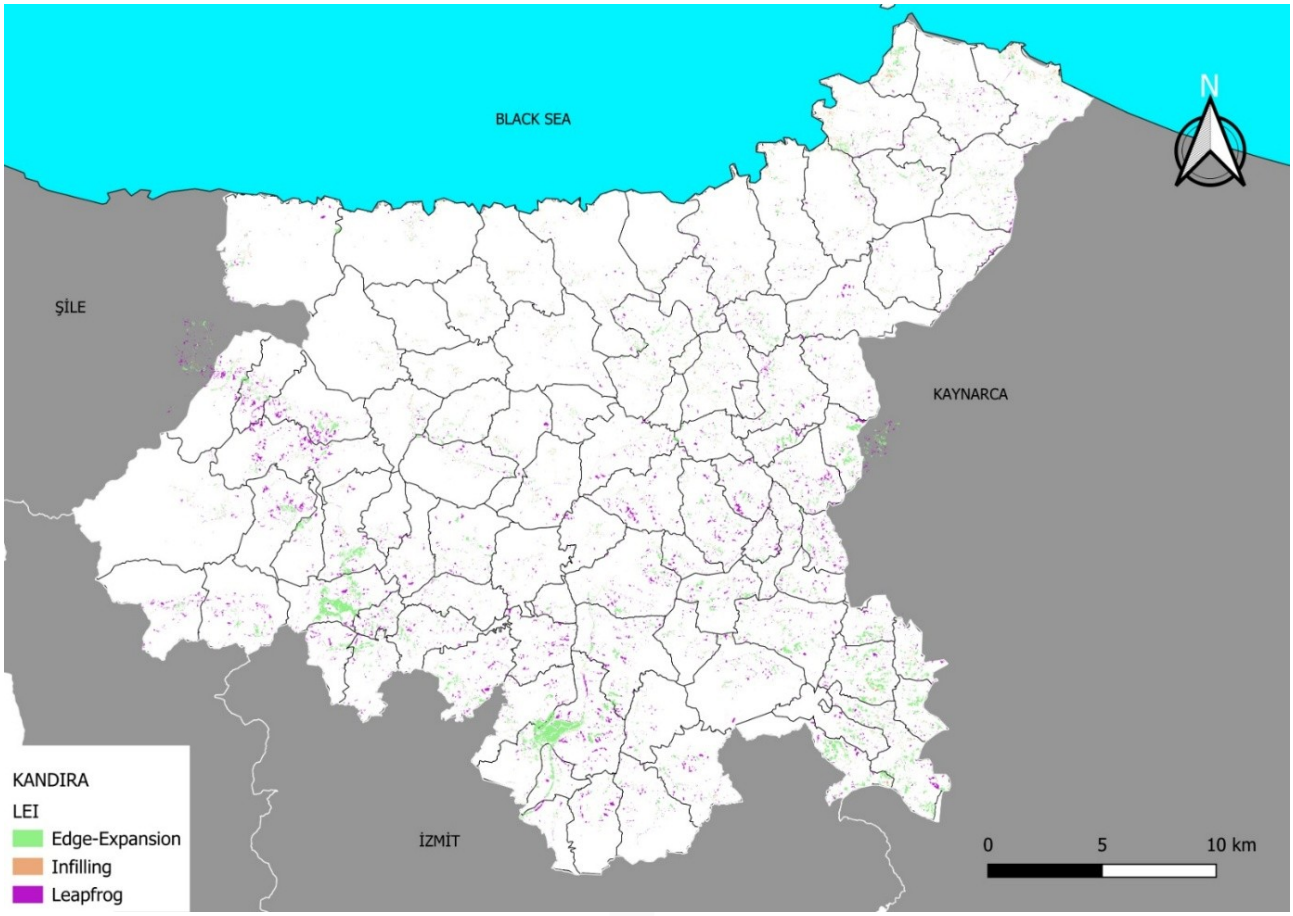

Figure 10. Landscape Expansion Index (LEI) analysis results.

4. DISCUSSION

The concept of resilience, which is increasingly being discussed in urban literature and urban policies, has begun to be expressed under several main headings. When the concept of resilience is evaluated specifically for the district of Kandıra in the province of Kocaeli, which is the study area, analyses have revealed that it is fragile in terms of ecological resilience. The fact that Kandıra district is relatively distant from major fault lines and more resilient to other disaster risks, as well as being adjacent to a megacity like Istanbul, has made the analyses conducted in this study indicative for the concrete calculation of the rapidly increasing urban pressure on rural areas following the pandemic. The Random Forest algorithm and Landtrendr analyses used in the study are understood to play a critical role in detecting changes in the spatial characteristics of the region and to be viable approaches for determining growth trends. Griffiths et al. (2013), used the LandTrendr algorithm with high accuracy in detecting abandoned deforestation as well as agricultural land. The findings obtained in this study also support the use of the algorithm in this direction. The spatial distribution of areas undergoing conversion from agriculture to artificial land in the study was found to be non-random when the spatial statistics were examined. The concentration of pixels undergoing transformation at an average distance of 727 meters from rural settlement centers identified in the 1/25,000 scale Mas-

ter Land Use Plan demonstrates that the urbanization dynamics in Kandıra exhibit the Edge-Expansion characteristic defined by Liu et al. (2010). This situation indicates a process in which agricultural land on the outskirts of existing villages is gradually incorporated into settlement areas, rather than the scattered leap-frog/outlying growth mentioned in the literature. Although this spatial dependency appears advantageous in terms of infrastructure costs, it demonstrates that planned settlement boundaries (village settlement areas) have effectively expanded at the expense of agricultural land and that the rural fabric is under pressure from urban sprawl. Furthermore, changes in land cover, as revealed by overlay analyses conducted using Land Capacity Classes, show partial alignment with the urban growth pattern described by Forman (1995) using the Path of Least Resistance approach. The fact that the conversion rate in Class I and II absolute agricultural lands, as stipulated by the Soil Conservation and Land Use Law No. 5403, remains at 9.7% suggests that deterrence measures for soil conservation in our country are functioning at a certain level. However, the high conversion rates of 50.7% in Class VI (marginal) lands and 25% in Class IV lands indicate that conservation pressure is shifting to weaker links. Given the current trend, this points to a gap in urban policy whereby, rather than rational and planned land selection taking place, agricultural land with potential (particularly Class IV) is left vulnerable or less resistant to urban pressure. The 2,503 hectares of land identified as having been converted from agriculture to artificial areas should not be viewed merely as a loss of vegetation. By increasing the cumulative heat load of these changing areas, it is also likely to have potential effects on the climate in the region. Indeed, studies conducted specifically in the province of Kocaeli (Akyürek, 2020) have clearly demonstrated a linear relationship between the increase in artificial surfaces and Land Surface Temperature (LST). This study also found that urban areas form distinct heat islands compared to rural environments. In this context, the areas identified in the study that have transitioned from agriculture to urban areas can be considered potential Hot Spots carrying the risk of thermal degradation, as indicated by Akyürek (2020). This transformation in an area that feeds Istanbul's climate corridor and water basin, such as Kandıra, is thought to accelerate regional ecological vulnerability in the long term, paving the way for ecological imbalance.

In this study, the high-resolution detections of the Sentinel-2 based Random Forest (RF) model were cross-validated using the Landsat-based Landtrendr time-series algorithm. The spatial agreement between the two algorithms was analyzed through a class-specific spatial masking technique. To achieve this, the continuous SWIR change magnitude values generated by the Landtrendr algorithm were thresholded and converted into a binary change mask. This binary mask was then multiplied pixel-by-pixel with the categorical RF map, which contained five distinct change classes (Urban, Forest, Agriculture, Water, Bare Land). Through this raster multiplication, only the pixels confirmed by Landtrendr in the time-series retained their original RF class values, allowing for the independent calculation of recall rates for each land cover category. The results demonstrated that the two methods exhibited a high rate of agreement (60%) in large-scale and permanent structural transformations, such as the Food Specialized Organized Industrial Zone. The spatial agreement between the the-

matic change map (RF) and the structural disturbance map (Landtrendr) was evaluated using the Jaccard Similarity Index, yielding a value of 0.104 (10.41%). While seemingly low for traditional single-sensor land cover comparisons, this value is highly expected and algorithmically justifiable in cross-methodological change detection frameworks (e.g., Cohen et al., 2018). This low spatial overlap stems from two fundamental disparities. First, the spatial mismatch between the 10-meter Sentinel-2 pixels and 30-meter Landsat pixels inherently reduces pixel-to-pixel intersection. Second, and more importantly, the two algorithms measure entirely different physical phenomena. Random Forest detects thematic land-cover conversion, whereas LandTrendr detects abrupt spectral structural disturbances. Therefore, rather than expecting a perfect spatial overlap, this study utilizes these two algorithms to capture different dimensions of the change: RF delineates the spatial typology and total area of urban expansion, while LandTrendr highlights the temporal trajectory and onset years of the vegetation disturbance.

5. CONCLUSION AND RECOMMENDATIONS

In our century, factors such as increasing migration due to globalization and global warming, the depletion of water resources, major fluctuations in agricultural production, and loss of biodiversity have made the sustainability of cities and the conservation of resources even more important. Undoubtedly, efforts to make cities sustainable and more resilient, as well as methods for measuring the effectiveness of these efforts, encompass many areas and methodologies. This study attempts to examine changes in rural land cover during the 2017-2024 period from an integrated perspective, combining cloud-based remote sensing technologies and spatial statistical methods. The spatial characteristics of the transformation were examined, determining the direction of the loss and the type of land cover affected, as well as identifying which agricultural lands experienced the greatest transformation in terms of agricultural productivity.

According to the findings of this study, it is important that conservation policies for sustainable land management be revised to include not only absolute agricultural lands but also Class IV lands, which have low resistance to urbanization and serve as buffer zones under urban pressure. In planning practice, rather than allowing the uncontrolled expansion of village settlement boundaries in response to the identified trend of Edge Expansion, it is necessary to implement Green Belt strategies that prioritize the preservation of the existing fabric and prevent sprawl. In addition, local governments or institutions responsible for spatial planning under the Ministry of Agriculture and Forestry can use LandTrendr, Sentinel and other high-resolution satellite images, or remote sensing systems with even higher resolution as an early warning system. This system can be used to detect and intervene in the destruction of agricultural areas before it reaches the stage of concretisation. This is important in terms of the effectiveness of rural planning, the protection of resources, and the prevention of vegetation loss.

REFERENCES

Agaton, M., Setiawan, Y., & Effendi, H. (2016). Land use/land cover change detection in an urban watershed: a case study of upper Citarum Watershed, West Java Province, Indonesia. Procedia Environmental Sciences, 33, 654–660. https://doi.org/10.1016/j.proenv.2016.03.120

Akyürek, Ö. (2020). Termal uzaktan algılama görüntüleri ile yüzey sıcaklıklarının belirlenmesi: Kocaeli örneği [Determination of surface temperatures with thermal remote sensing imagery: Kocaeli case]. Doğal Afetler ve Çevre Dergisi, 6(2), 377–390. https://doi.org/10.21324/dacd.667594

Butt, A., Shabbir, R., Ahmad, S. S., & Aziz, N. (2015). Land use change mapping and analysis using Remote Sensing and GIS: A case study of Simly watershed, Islamabad, Pakistan. The Egyptian Journal of Remote Sensing and Space Sciences, 18(2), 251–259. https://doi.org/10.1016/j.ejrs.2015.07.003

Chen, D., Wang, Y., Shen, Z., Liao, J., Chen, J., & Sun, S. (2021). Long time-series mapping and change detection of coastal zone land use based on Google Earth Engine and multi-source data fusion. Remote Sensing, 14(1), Article 1. https://doi.org/10.3390/rs14010001

Cohen, W. B., Healey, S. P., Yang, Z., Stehman, S., Brewer, C., Brooks, E. B., Gorelick, N., Huang, C., Hughes, M. J., & Zhu, Z. (2017). How similar are forest disturbance maps derived from different Landsat time series algorithms? Forests, 8(4), Article 98. https://doi.org/10.3390/f8040098

Drummond, M. A., & Loveland, T. R. (2010). Land-use pressure and a transition to forest-cover loss in the eastern United States. BioScience, 60(4), 286–298. https://doi.org/10.1525/bio.2010.60.4.7

Forman, R. T. T. (1995). Land mosaics: The ecology of landscapes and regions. Cambridge University Press.

Ghorbanian, A., Kakooei, M., Amani, M., Mahdavi, S., Mohammadzadeh, A., & Hasanlou, M. (2020). Improved land cover map of Iran using Sentinel imagery within Google Earth Engine and a novel automatic workflow for land cover classification using migrated training samples. ISPRS Journal of Photogrammetry and Remote Sensing, 167, 276–288. https://doi.org/10.1016/j.isprsjprs.2020.07.013

Gorelick, N., Hancher, M., Dixon, M., Ilyushchenko, S., Thau, D., & Moore, R. (2017). Goog-le Earth Engine: Planetary-scale geospatial analysis for everyone. Remote Sensing of Environ-ment, 202, 18–27. https://doi.org/10.1016/j.rse.2017.06.031

Griffiths, P., Müller, D., Kuemmerle, T., & Hostert, P. (2013). Agricultural land change in the Carpathian ecoregion after the breakdown of socialism and expansion of the European Union. Environmental Research Letters, 8(4), Article 045024. https://doi.org/10.1088/1748-9326/8/4/045024

Gu, Y., Liu, T., Gao, G., Ren, G., Ma, Y., Chanussot, J., & Jia, X. (2021). Multimodal hyperspectral remote sensing: an overview and perspective. Science China Information Sciences, 64(12), Article 121301. https://doi.org/10.1007/s11432-020-3084-1

Güneş, S. (2022, February 25). Kandıra İzmit yolunun 7 kilometrelik kısmı açıldı. Kocaeli Gazetesi. https://www.kocaeligazetesi.com.tr/haber/9480672/kandira-izmit-yolunun-7-kilometrelik-kismi-acildi

Huang, H., Chen, Y., Clinton, N., Wang, J., Wang, X., Liu, C., Gong, P., Yang, J., Bai, Y., Zheng, Y., & Zhu, Z. (2017). Mapping major land cover dynamics in Beijing using all Landsat images in Google Earth Engine. Remote Sensing of Environment, 202, 166–176. https://doi.org/10.1016/j.rse.2017.05.034

Kandıra District Governor's Office. (2025, December). Geographical location and landforms of Kandıra. T.C. Kandıra Kaymakamlığı. https://www.kandira.gov.tr/cografi-konumu-ve-yeryz-sekilleri

Karayolları Genel Müdürlüğü. (2022, June). İzmit-Kandıra-Kaynarca Yolu, Çubuklubala-Çubuklu Osmaniye Varyantı ile Cezaevi Varyantı. T.C. Ulaştırma ve Altyapı Bakanlığı. https://www.kgm.gov.tr/Sayfalar/KGM/SiteTr/Projeler/ProjelerDetay.aspx?q=87

Kennedy, R. E., Yang, Z., & Cohen, W. B. (2010). Detecting trends in forest disturbance and recovery using yearly Landsat time series: 1. LandTrendr—Temporal segmentation algorithms. Remote Sensing of Environment, 114(12), 2897–2910. https://doi.org/10.1016/j.rse.2010.07.008

Kennedy, R. E., Yang, Z., Gorelick, N., Braaten, J., Cavalcante, L., & Cohen, W. B. (2018). Implementation of the LandTrendr algorithm on Google Earth Engine. Remote Sensing, 10(5), Article 691. https://doi.org/10.3390/rs10050691

Kongar, E. (2002). 21. Yüzyılda Türkiye: 2000'li yıllarda Türkiye'nin toplumsal yapısı. Remzi Kitabevi.

Li, X., & Yeh, A. G. O. (2004). Analyzing spatial restructuring of land use patterns in a fast growing region using remote sensing and GIS. Landscape and Urban Planning, 69(4), 335–354. https://doi.org/10.1016/j.landurbplan.2003.10.033

Li, Y., Liu, C., Zhao, W., & Huang, Y. (2020). Multi-spectral remote sensing images feature coverage classification based on improved convolutional neural network. Mathematical Biosciences and Engineering, 17(5), 4443–4456. https://doi.org/10.3390/mbe.2020245

Liu, X., Li, X., Chen, Y., Tan, Z., Li, S., & Ai, B. (2010). A new landscape index for quantifying urban expansion using multi-temporal remotely sensed data. Landscape Ecology, 25(5), 671–682. https://doi.org/10.1007/s10980-010-9454-5

Nguyen, L. B. (2020). Land cover change detection in northwestern Vietnam using Landsat images and Google Earth Engine. Journal of Water and Land Development, 46, 162–169. https://doi.org/10.24425/jwld.2020.134209

Okoduwa, A. K., & Amaechi, C. F. (2024). Exploring Google Earth Engine, Machine Learning, and GIS for Land Use and Land Cover Change Detection in the Federal Capital Territory, Abuja, between 2014 and 2023. Applied Environmental Research, 46(2), Article 029. https://doi.org/10.35762/AER.2024029

Oktay, Ş. (2019, September 22). Kandıra Gıda İhtisas OSB binlerce kişiye ekmek kapısı olacak. Anadolu Ajansı. https://www.aa.com.tr/tr/ekonomi/kandira-gida-ihtisas-osb-binlerce-kisiye-ekmek-kapisi-olacak/1590579

Pande, B. C. (2022). Land use/land cover and change detection mapping in Rahuri watershed area (MS), India using the Google Earth Engine and machine learning approach. Geocarto International, 37(26), 13860–13880. https://doi.org/10.1080/10106049.2022.2086622

Rogan, J., & Chen, D. M. (2004). Remote sensing technology for mapping and monitoring land-cover and land-use change. Progress in Planning, 61(4), 301–325. https://doi.org/10.1016/S0305-9006(03)00066-7

Szeliski, R. (2022). Computer vision: Algorithms and applications (2nd ed.). Springer. https://doi.org/10.1007/978-3-030-34372-9

Teja, J., Vaddi, R., Lakshmika, K., & Nirupama, P. (2024, April 24–26). Land use and land cover change detection using Google Earth Engine [Paper presentation]. 7th International Conference on Inventive Computation Technologies (ICICT 2024), Lalitpur, Nepal.

Tırmanoğlu, B., İsmailoğlu, İ., Kokal, A. T., & Musaoğlu, N. (2023). Yeni nesil multispektral ve hiperspektral uydu görüntülerinin arazi örtüsü/arazi kullanımı sınıflandırma performanslarının karşılaştırılması: Sentinel-2 ve PRISMA Uydusu [Comparison of land cover/land use clas-sification performances of next-generation multispectral and hyperspectral satellite imagery: Sentinel-2 and PRISMA Satellite]. Geomatik, 8(1), 79–90. https://doi.org/10.29128/geomatik.1126685

Tobler, W. R. (1970). A computer movie simulating urban growth in the Detroit region. Economic Geography, 46, 234–240. https://doi.org/10.2307/143141

ADVANCES IN GEOMATICS

VOLUME 04 • ISSUE 01 • APRIL 2026
e-ISSN: 3023-4980

ORIGINAL ARTICLE

Submission: 02/02/2026
Accepted: 27/04/2026

MACHINE LEARNING-BASED TRAFFIC PREDICTION AND TRAFFIC-AWARE VEHICLE ROUTING OPTIMIZATION

Gökçe TEMEL[1]*

[1] Department of Geomatics, Engineering Faculty, Kocaeli University, Kocaeli, Türkiye.

* Corresponding Author: G. Temel, gokce.temel.142@gmail.com 0009-0002-5996-8043

ABSTRACT

Fixed-speed planning approaches widely used in urban logistics operations lead to unreliable delivery commitments by disregarding the dynamic traffic conditions of large cities. This study aims to develop an integrated pipeline that connects traffic speed prediction directly to road network cost calculation and vehicle routing optimization. A CatBoost gradient boosting algorithm was trained using approximately 19 million rows of 2024 traffic data obtained from the Istanbul Metropolitan Municipality Open Data Portal. The developed M2 model achieved R^2=0.856 in temporal testing, while in the spatial holdout test — where the baseline model collapsed with R^2=–0.340 — it maintained functionality with R^2=0.418, demonstrating that geographic features contributed +0.758 to spatial generalization capacity. Consistent performance in the range of R^2=0.863–0.884 was achieved in independent external validation conducted with data from January 2025. Model predictions were transferred to the Istanbul road network of 506,667 edges via Dijkstra's algorithm and provided as input to the Vehicle Routing Problem with Time Windows solved using OR-Tools. The dynamic validation analysis revealed a critical finding: while the static model predicted reaching 28 out of 30 points on time, simulation of this plan with traffic predictions showed that only 19 points could be reached. This 32% error rate concretely demonstrates that traffic-aware planning is indispensable for operational reliability.

Keywords: Vehicle Routing Problem, Vehicle Routing Problem with Time Windows, Traffic Speed Prediction, CatBoost, Machine Learning, Spatial Generalization.

Cited As:

Temel, G. (2026). Machine Learning-Based Traffic Prediction and Traffic-Aware Vehicle Routing Optimization, Advances in Geomatics, 4(1), 106-122. https://doi.org/10.5281/zenodo.20561364

1. INTRODUCTION

The growing global e-commerce volume and increasing urban population density are transforming city logistics operations into an increasingly complex planning problem. The Vehicle Routing Problem (VRP) constitutes the mathematical framework of this complexity and has remained one of the central research topics in combinatorial optimization literature for decades (Dantzig and Ramser, 1959; Cordeau et al., 2002). However, the majority of existing routing approaches rely on fixed travel time assumptions. This assumption deviates significantly from reality in megacities such as Istanbul, where traffic density varies dramatically on an hourly and regional basis.

Istanbul has a unique transportation dynamic with a population exceeding 15 million and a geographical structure divided in two by the Bosphorus. Systematic congestion at bridge crossings can double travel times during morning peak hours compared to nighttime conditions. Routing systems that exclude this level of variability from the planning process not only produce inefficient routes but also systematically violate delivery commitments made to customers.

In recent years, significant advances have been made in traffic speed prediction with the development of machine learning methods. Boukerche and Wang (2020) systematically reviewed machine learning-based traffic prediction models, while Bratsas et al. (2020) comparatively evaluated the contribution of different algorithms to urban traffic prediction. In the Turkish context, Subaşı (2025) demonstrated that the GWO-XGBoost combination achieves high prediction accuracy on Istanbul traffic data. In the vehicle routing literature, Ichoua et al. (2003) and Figliozzi (2012) examined the effect of time-dependent travel times on routing decisions; however, these studies relied on synthetic speed profiles rather than real data. Among studies directly combining machine learning with VRP, Shahbazian et al. (2024) demonstrated that hybrid systems produce more realistic results compared to static approaches.

Three fundamental gaps are evident when the literature is evaluated. First, traffic prediction studies focus on model accuracy without addressing the conversion of predictions into route cost functions. Second, routing studies largely rely on fixed travel time assumptions or synthetic speed profiles not derived from real data. Third, an integrated pipeline approach combining traffic prediction and vehicle routing within a single decision process remains quite limited in the literature.

This study addresses these gaps with the following contributions. A CatBoost model trained on approximately 19 million rows of real Istanbul traffic data was used as input to route cost calculation. Predictions were transferred to the Istanbul road network of 506,667 edges. A spatial holdout test conducted with geographic features measured the model's generalization capacity at locations it had never seen and demonstrated the operational significance of this capacity. Through dynamic validation, the performance of static plans under traffic conditions was simulated and the operational cost of planning that disregards traffic information was concretely measured.

2. METHODOLOGY

2.1 Data Sources

Three different data sources were utilized in this study. Hourly traffic speed data for 2024 was obtained from the Istanbul Metropolitan Municipality Open Data Portal (IMM, 2024). This dataset consists of approximately 19 million rows containing geographic coordinates, timestamps, and average speed information. January 2025 traffic data was reserved as an external validation set to test the model's generalizability to an independent time period. The Istanbul road network was obtained from OpenStreetMap data through the OSMnx library developed by Boeing (2017), and road type and legal speed limit information were compiled for each road segment in this network consisting of 192,716 nodes and 506,667 edges (OpenStreetMap Contributors, 2024). Hourly average temperature and precipitation data were obtained by averaging the three nearest meteorological stations to Istanbul through the Meteostat library (Meteostat, 2024).

2.2 Traffic Speed Prediction Model

The variable predicted by the model was defined as speed ratio rather than raw speed: SPEED_RATIO = Average Speed / Speed Limit.The ratio was bounded between 0.05 and 2.0. The lower bound of 0.05 prevents division-by-zero errors and eliminates physically implausible near-zero speed recordings likely caused by sensor noise. The upper bound of 2.0 reflects the empirical observation that vehicles rarely exceed twice the posted speed limit under any real-world conditions; values above this threshold were treated as sensor anomalies. In the 2024 dataset, only 0.3% of raw observations exceeded this upper bound, confirming that the clipping operation has negligible impact on the data distribution while eliminating outliers that would otherwise distort model training.

Four categories of features were used. Within temporal features, hour and month variables were encoded using sine-cosine transformation to preserve cyclical continuity (Bratsas et al., 2020). Within geographic features, Haversine distances from each geohash cell to Taksim, Kadıköy, and the nearest Bosphorus bridge were calculated. Within road features, road type obtained from OSM and speed limit information derived through a hybrid strategy were used. Within weather features, hourly temperature and precipitation amounts were incorporated into the model.

Traffic data was encoded using the geohash method developed by Niemeyer (2008) at precision=6 level, corresponding to cells of approximately 1.2 km x 0.6 km. A total of 2,463 unique geohash cells were observed across Istanbul in the 2024 dataset.

Four different models were developed using the CatBoost gradient boosting algorithm developed by Prokhorenkova et al. (2018). CatBoost prevents target leakage by processing categorical variables through the ordered target statistics method and eliminates prediction shift through the ordered

boosting mechanism. The M1 baseline model contains only temporal, road, and GEOHASH identity features. The M2 model was constructed by adding geographic distance features to M1. The M3 model was developed by adding weekly lagged observations inspired by Ichoua et al. (2003) and Figliozzi (2012), while the M4 model incorporated hourly lagged observations. The M2 model was selected as the operational model; M3 and M4 require access to historical observations and therefore cannot be used in real operational scenarios such as new locations or system interruptions.

All models were trained with identical hyperparameters: iterations=2000, depth=8, learning_rate=0.05, early_stopping_rounds=200, random_seed=42. This standardization guarantees that performance differences between models arise solely from the feature set.

Model performance was evaluated using two different strategies: temporal and spatial. In the temporal split, the training set covers January–September 2024, the validation set covers October–November 2024, and the test set covers December 2024. In the spatial holdout test, drawing on the spatial generalization requirement emphasized by Boukerche and Wang (2020), 20% of the 2,463 geohash cells were completely excluded from the training set, forcing the model to produce predictions for these locations without having seen them.

2.3 Graph-Based Route Cost

A travel time weight based on the speed prediction produced by the M2 model was assigned to each road network edge:

$$t_{edge} = \frac{L}{\left(\frac{v_{predicted}}{3.6}\right)} \quad (1)$$

Where L represents edge length in meters and vpredicted represents the speed in km/h obtained by multiplying the model's predicted speed ratio by the speed limit. Rather than making separate predictions for 506,667 edges, a geohash-based architecture was adopted; predictions were made at the level of 2,463 unique geohash cells and results were transferred to the corresponding edges. The shortest-time routes between point pairs were determined using Dijkstra's (1959) algorithm and the resulting travel times formed the time matrix provided as input to the VRPTW solver. The static model used for comparison assigns a fixed speed of 45 km/h to all edges.

2.4 Vehicle Routing Problem with Time Windows

Drawing on the VRPTW framework standardized by Solomon (1987), the problem was modeled as an optimization problem in which three vehicles departing from the Yenibosna depot visit 30 customer points. A service time of 15 minutes and an operation window of 09:00–19:00 were defined at each point. Customer points were selected to cover both sides of Istanbul; points close to the depot received early and narrow windows, while distant points received late windows. Three different scales containing 5, 15, and 30 customer points were compared to examine how the advantage of traf-

fic-aware planning varies with problem size. The 5 and 15-point scenarios are subsets of the 30-point scenario, isolating the scale effect independently from point selection. Additionally, the most complex scenario — the 30-point problem — was run for two different dates, weekday and weekend, to concretize the traffic difference between working days and holidays. Optimization was performed using the Google OR-Tools library developed by Perron and Furnon (2023); the initial solution produced by the PATH_CHEAPEST_ARC strategy was improved using the Guided Local Search metaheuristic proposed by Voudouris and Tsang (1999).

2.5 Dynamic Validation

Dynamic validation is the process of re-evaluating the route plan determined by the static model using M2 model traffic predictions instead of the fixed speed assumption. Inspired by the hybrid simulation approach proposed by Shahbazian et al. (2024), the route sequence determined by the static model was kept fixed while the travel time of each edge was recalculated using the speed prediction produced by the M2 model for that hour. The arrival time at each customer point was calculated cumulatively and compared with the time window. This analysis does not use actual sensor data, but it references M2 estimates validated with January 2025 data.

The use of M2 predictions rather than observed sensor data for dynamic validation is a deliberate methodological choice driven by data availability constraints. The 2025 sensor dataset does not provide uniform spatial coverage across all 30 customer points in the scenario; Istanbul's sensor network is concentrated on major arterials and central districts, leaving peripheral locations without direct measurements. M2 predictions, by contrast, can generate travel time estimates for any location within the road network by leveraging geographic proximity features, thereby enabling a consistent and spatially complete simulation environment. While this introduces model-based uncertainty into the validation, the M2 model's demonstrated accuracy of R^2=0.863–0.884 on January 2025 sensor data provides a reasonable empirical basis for its use as a reference.

3. RESULTS

3.1 Model Performance

Four models were evaluated on the December 2024 test set. Results are presented in Table 1. Although only geographic distance features were added in the transition from M1 to M2, R^2 increased from 0.820 to 0.856 and RMSE dropped from 7.69 to 6.82 km/h. The additional gain achieved by M3 and M4 with historical observations is an expected result; traffic conditions from the same hour of the previous week serve as a strong predictor. However, these models were not used in this study due to operational constraints. The standard deviation ratio calculated to measure the model's tendency toward mean regression was found to be 0.910 for M2, indicating that the model can represent the

extreme conditions of traffic density with sufficient variation.

Table 1. Performance of M1–M4 models on the December 2024 test set.

Model	R^2	RMSE (km/h)	MAE (km/h)
M1 Baseline	0.820	7.69	5.26
M2 Geographic	0.856	6.82	4.58
M3 Historical	0.895	5.85	3.75
M4 Real-Time	0.901	5.69	3.68

The M1 model failed completely in the spatial holdout test with R^2=–0.340. This result clearly demonstrates that M1 learns location information only through the geohash identity variable and cannot produce meaningful predictions for a geohash it has not seen during training. The M2 model achieved R^2=0.418 in the same test. The spatial generalization capacity difference between the M1 and M2 models was observed as 0.758 (Figure 1). This finding indicates that the integration of geographic features substantially enhances the model's capability to generalize across different spatial zones within the studied network. In real-world logistics scenarios, such as a vehicle fleet expanding into new depots or areas with limited sensor coverage, the M2 model demonstrates the potential to mitigate spatial prediction degradation by leveraging location-based relationships, thereby providing more robust estimations than the baseline model.

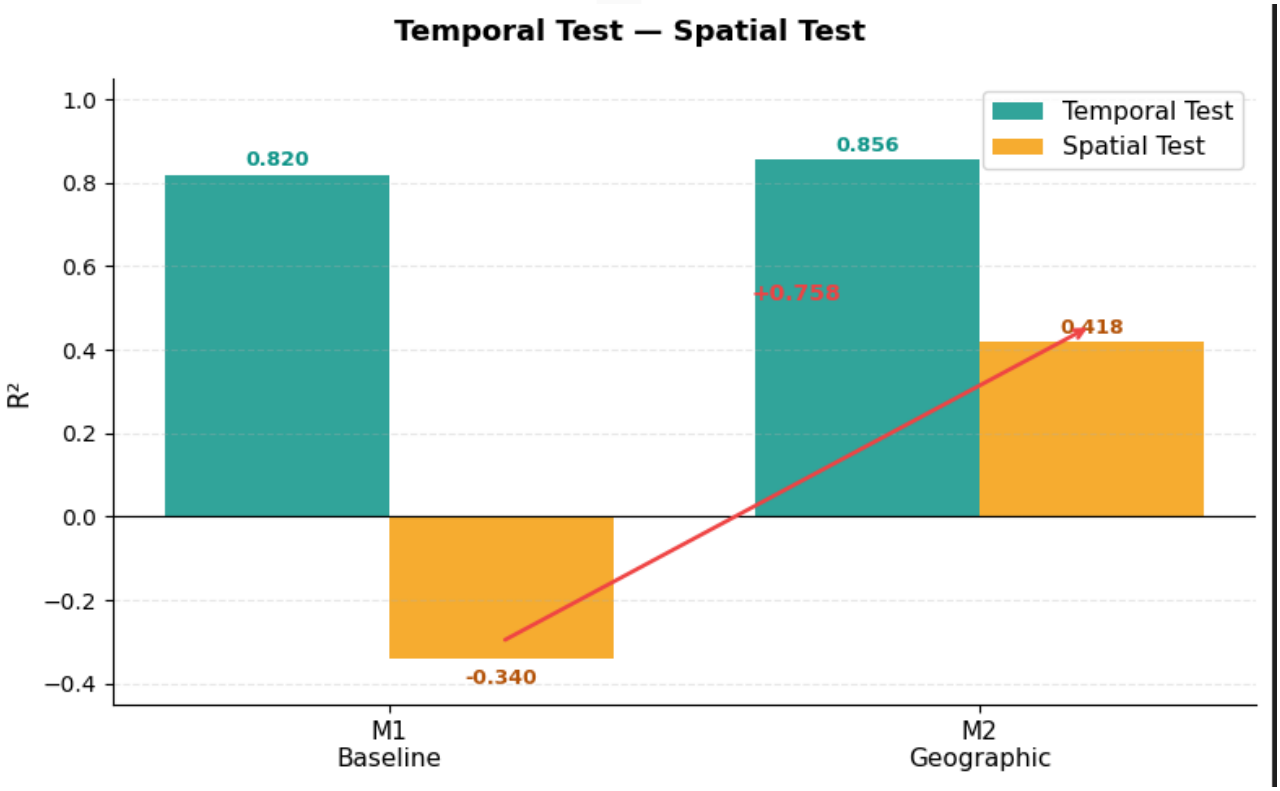

Figure 1. Temporal and spatial validation comparison of M1 and M2 models.

The external validation of the model with January 2025 data is presented in Figure 2. R^2=0.863 was achieved during morning peak hours (08:00), R^2=0.884 at midday (12:00), and R^2=0.847 at nighttime (23:00). The preservation of this performance on data from January 2025 demonstrates that the model has strong generalization capacity against seasonal traffic variability. The highest accuracy at midday reflects the relatively stable nature of traffic patterns at this hour, while the relatively lower performance at nighttime reflects the more variable character of nighttime traffic.

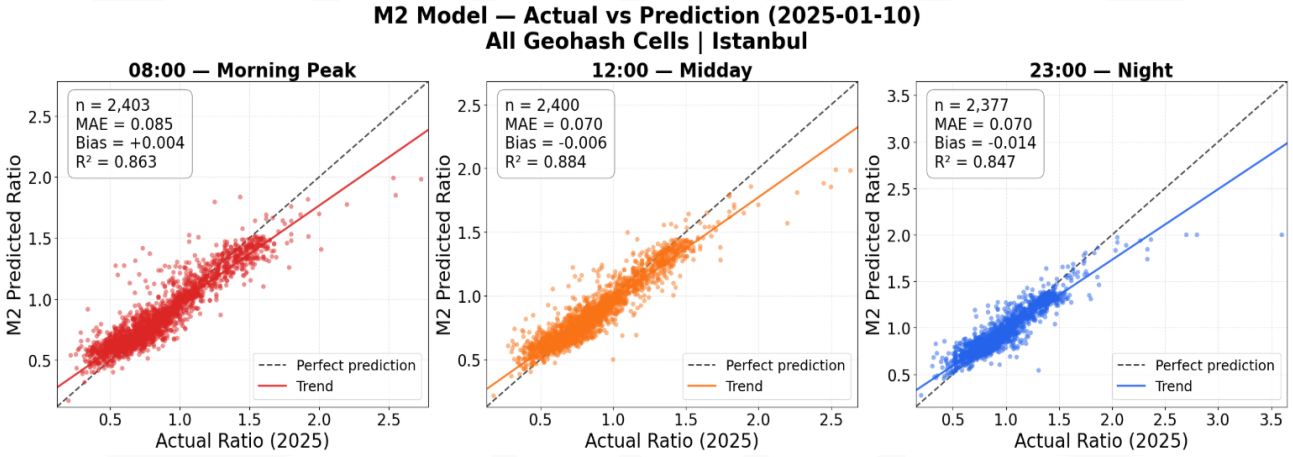

Figure 2. Comparison of the M2 model with real data in geohash cells on 2025-01-10.

Additionally, point-based validation was conducted at the Taksim (sxk97m) and Kadıköy (sxk9hq) geohash cells to evaluate whether the model captures the daily traffic pattern. Results are presented in Figure 3.

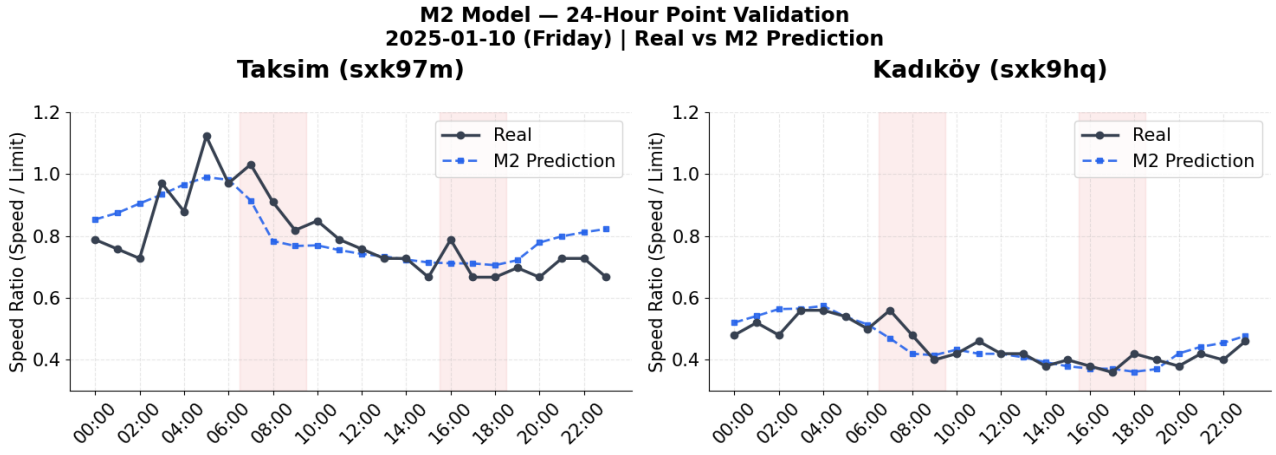

Figure 3. 24 Hour point validation.

When the figure is examined, it can be seen that the model accurately captures the daily traffic pattern at both points. The decrease in speed during morning and evening rush hours and the increase during nighttime hours were predicted by the model.

3.2 Segment Analysis

The two models diverged significantly in the comparative analysis conducted on the Esenyurt–Üsküdar route. As shown in Table 2, dynamic validation simulating the route that the static model planned at 53.7 minutes in the M2 environment revealed that it actually takes 64.8 minutes. The M2 model produced a more realistic plan of 59.1 minutes under the same conditions. The comparative map is presented in Figure 4.

Table 2. Esenyurt–Üsküdar route comparison at 08:00 and 23:00.

Scenario	Model	Planned Duration	Distance	Actual Duration	Error
08:00	M2	59.1 min	40.6 km	—	—
08:00	Static	53.7 min	40.3 km	64.8 min	+11.1 min
23:00	M2	45.5 min	41.5 km	—	—
23:00	Static	53.7 min	40.3 km	53.9 min	+0.2 min

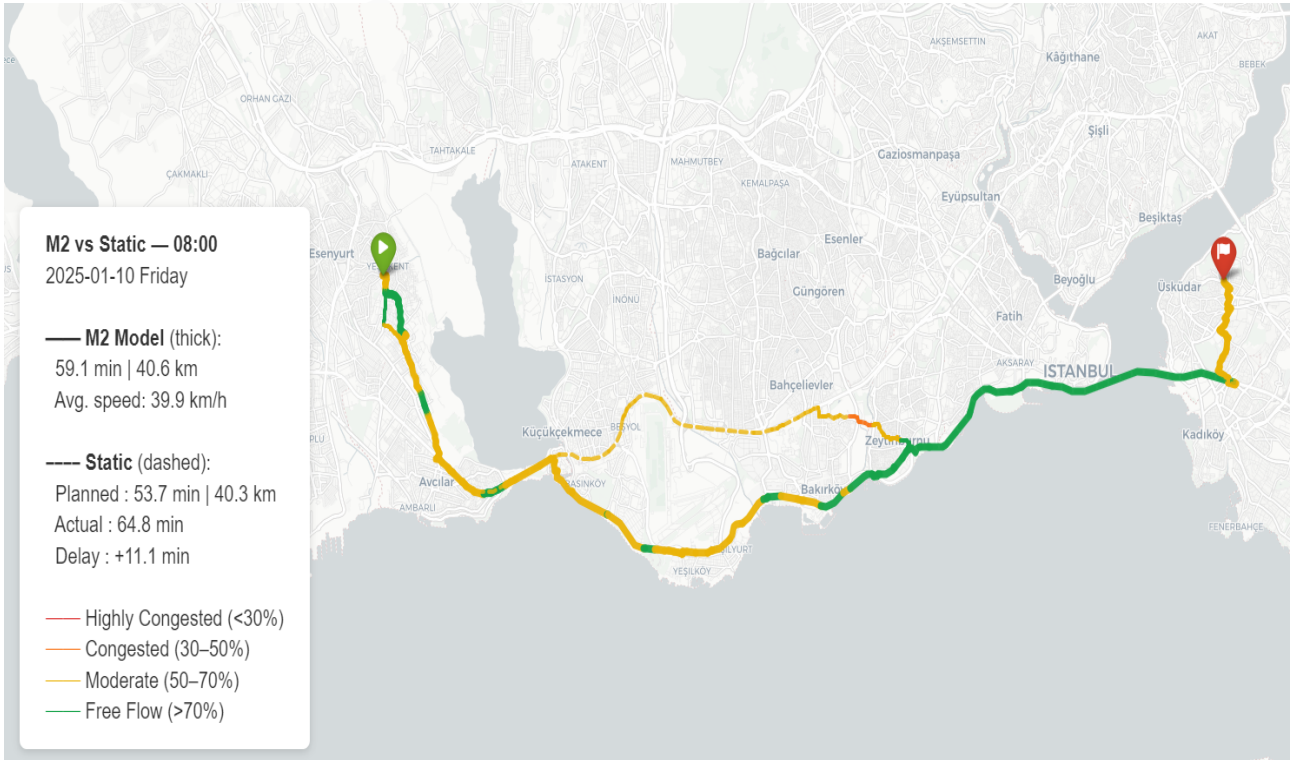

Figure 4. Segment analysis map at 08:00.

Under nighttime 23:00 conditions, the route changes substantially (Figure 5). While the M2 model produces a plan of 45.5 minutes by leveraging traffic fluidity, the static model again yields the same 53.7 minutes. Dynamic validation measured the static plan's duration in the M2 environment at

nighttime as 53.9 minutes; this 0.2-minute deviation demonstrates that the fixed speed assumption converges to reality during nighttime hours. It was observed that the two models propose not only different durations but also different routes, demonstrating that traffic information contributes to planning not only in terms of duration but also in terms of geographic decision-making.

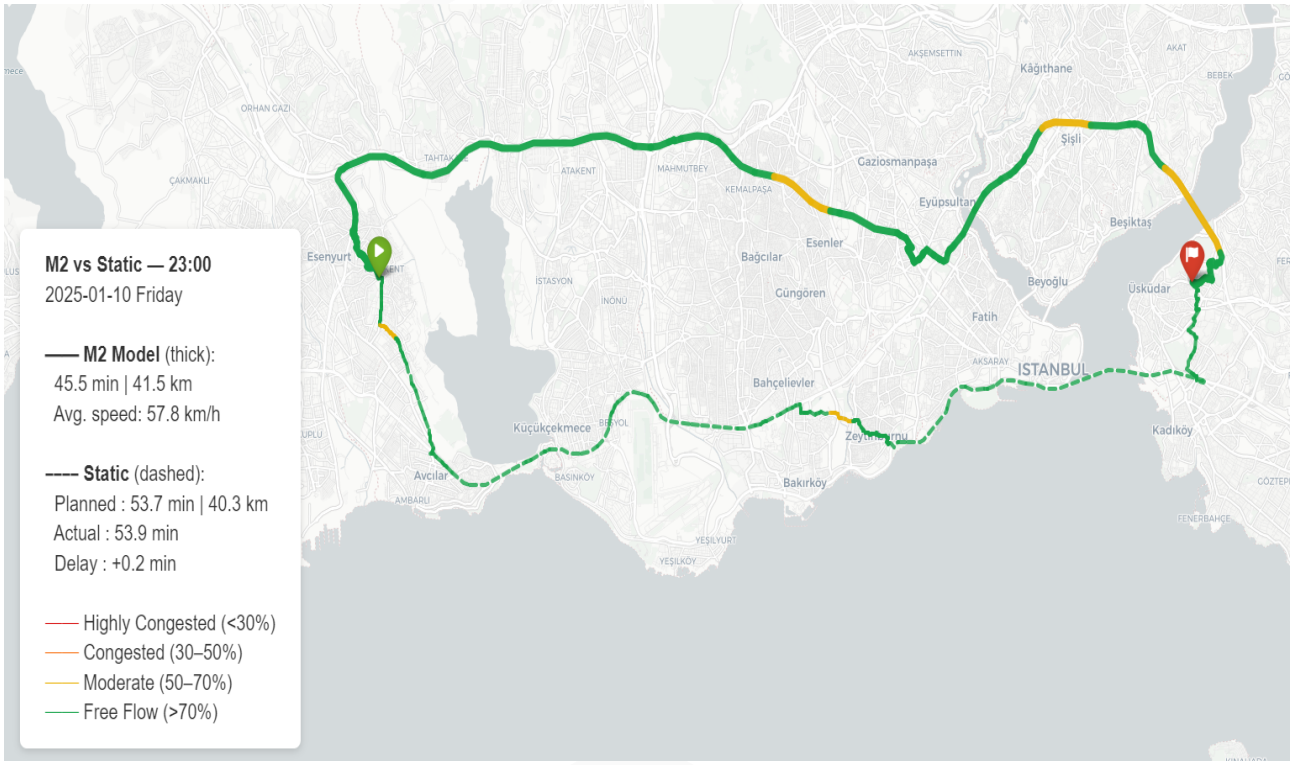

Figure 5. Segment analysis map at 23:00.

3.3 Vehicle Routing Results

Scale analysis results conducted with soft time windows under morning 08:00 peak conditions are presented in Table 3.

Table 3. Comparison of M2 and static models at different problem scales (Soft window, 08:00 am).

Scale	M2 (min)	Static (min)	Difference (min)	Difference (%)
5 points	280.5	259.5	+21.0	+8.1
15 points	638.9	543.8	+95.1	+17.5
30 points	1035.8	917.4	+118.4	+12.9

The absolute difference between M2 and the static model increases as problem scale grows. The 21-minute difference in the 5-point scenario reaches 118 minutes in the 30-point scenario. Each additional customer point adds a new travel segment and each segment contributes to cumulative delay.

Hour-based analysis results for the 30-customer-point scenario are presented in Table 4.

Table 4. Hour-based soft window comparison for 30 point scenario.

Hour	M2 (min)	Static (min)	Difference (min)	Difference (%)
08:00	1035.8	917.4	+118.4	+12.9
12:00	1011.9	917.4	+94.5	+10.3
23:00	916.0	917.4	−1.4	−0.2

The static model producing the same total duration at all three hours is the inevitable consequence of the fixed speed assumption. The −1.4- minute difference at 23:00 demonstrates that the M2 model is capable of not only cautious planning during peak hours but also efficient planning during fluid traffic conditions.

Under hard time window conditions, the static model plans to reach 28/30 points on time while the M2 model plans 26/30. The distribution of the 4 points excluded from the route in the M2 model is shown in Figure 6. Dynamic validation results obtained by simulating the static plan in the M2 environment are presented in Table 5.

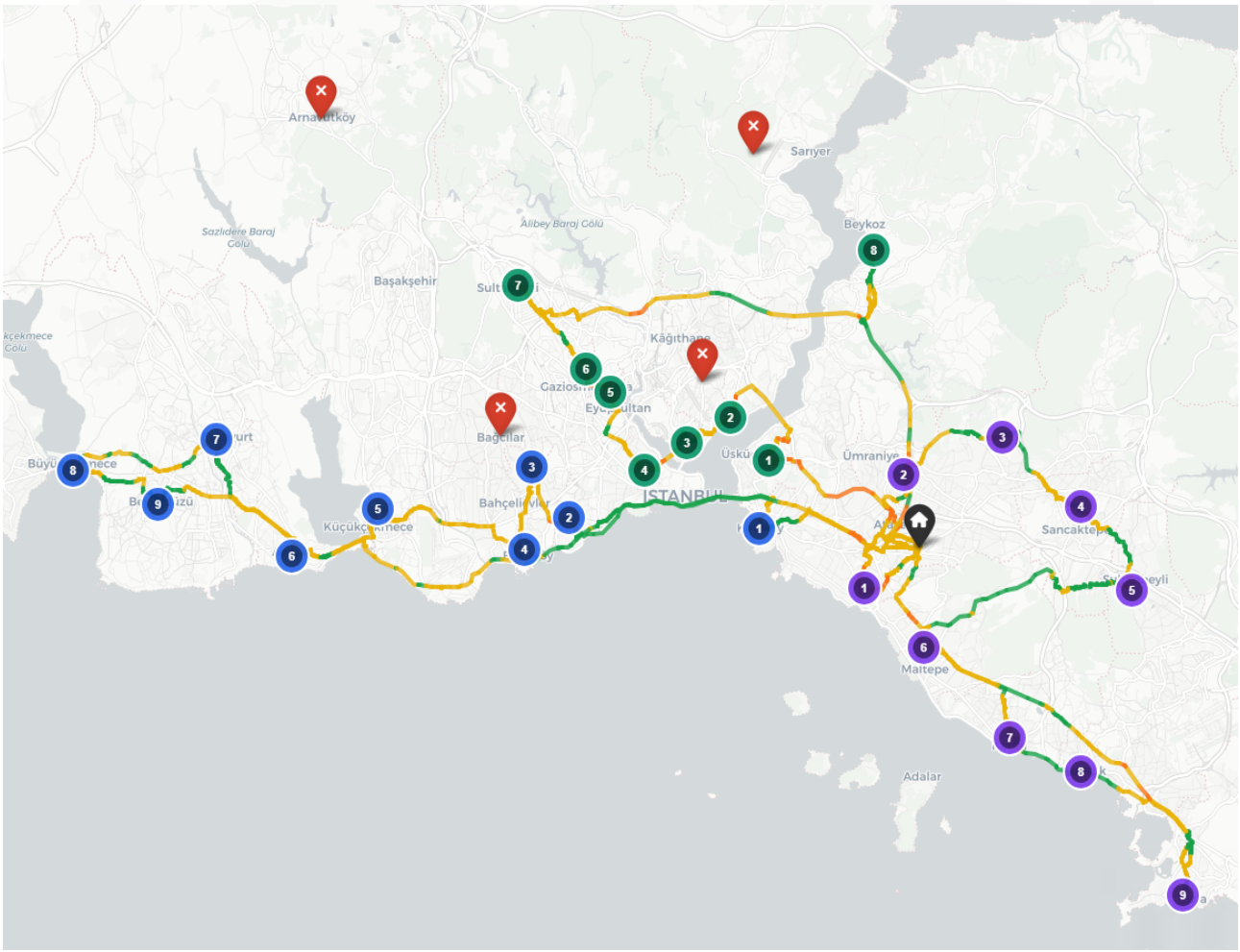

Figure 6. Solution of the M2 model.

Table 5. Dynamic validation of static plan in M2 environment.

Hour	On Time	Missed	Total Delay (min)
08:00	19/30	11/30	1236
12:00	19/30	11/30	1214
23:00	19/30	11/30	975

The difference between the 28 planned by the static model and the 19 actually achieved corresponds to a 32% error rate. The highest delays were observed at bridge-dependent points — Üsküdar, Ümraniye, and Beşiktaş. The lower total delay in the nighttime scenario confirms that the static model's error diminishes as traffic load decreases. The route on which the static plan was applied within the scope of dynamic validation is presented in Figure 7.

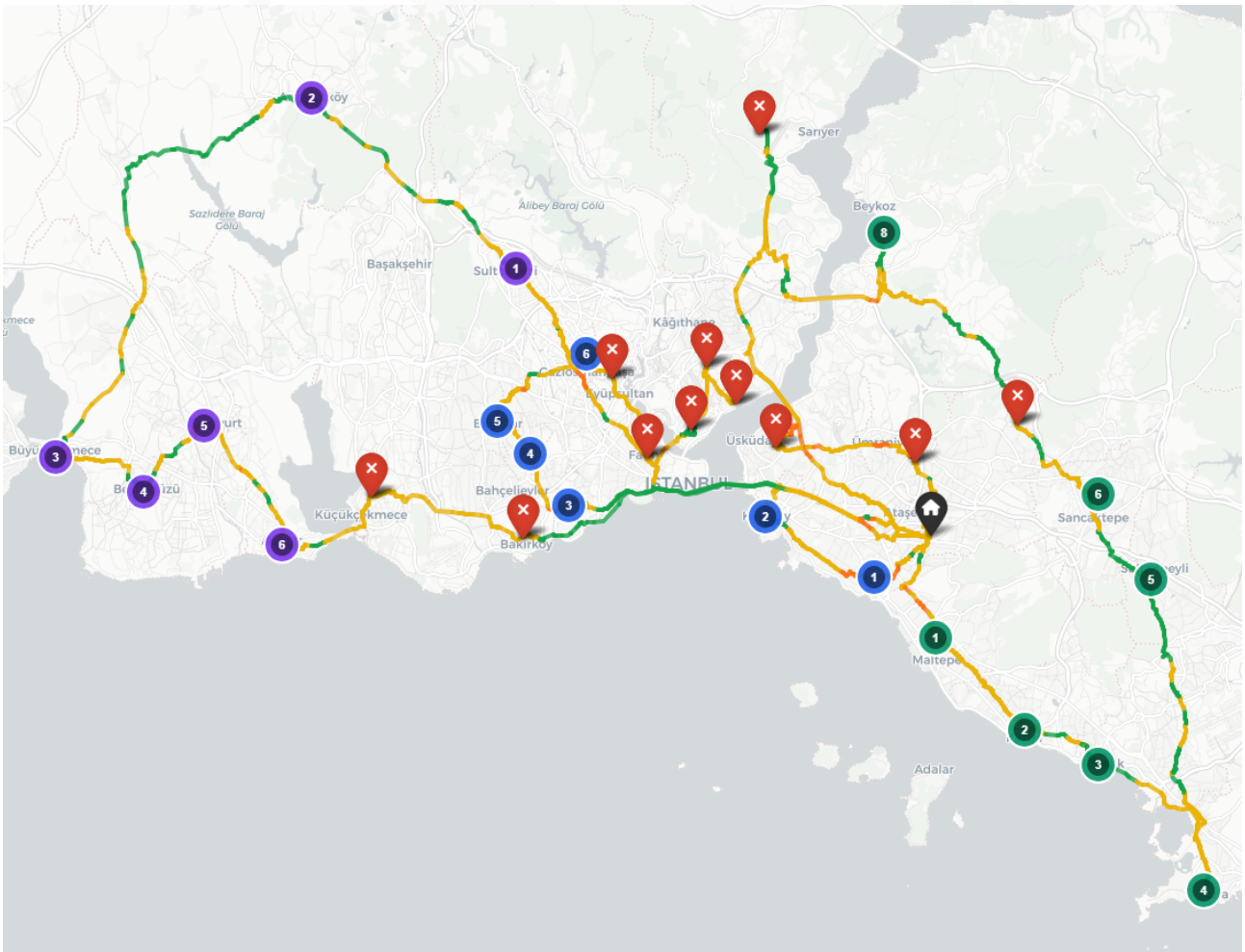

Figure 7. Implementation of the static plan in M2 traffic.

The comparison conducted for Friday (2025-01-10) and Saturday (2025-01-11) revealed that the advantage provided by the M2 model is directly related to traffic density. The M2–Static difference of 12.9% on Friday morning dropped to 3.5% on Saturday morning. When dynamic validation results are examined, it is observed that the number of missed points remained at similar levels for both days, while total delay dropped significantly on Saturday: the total delay of 1,236 minutes on Friday morning fell to 797 minutes on Saturday morning. Four comparative charts are presented together in Figure 8.

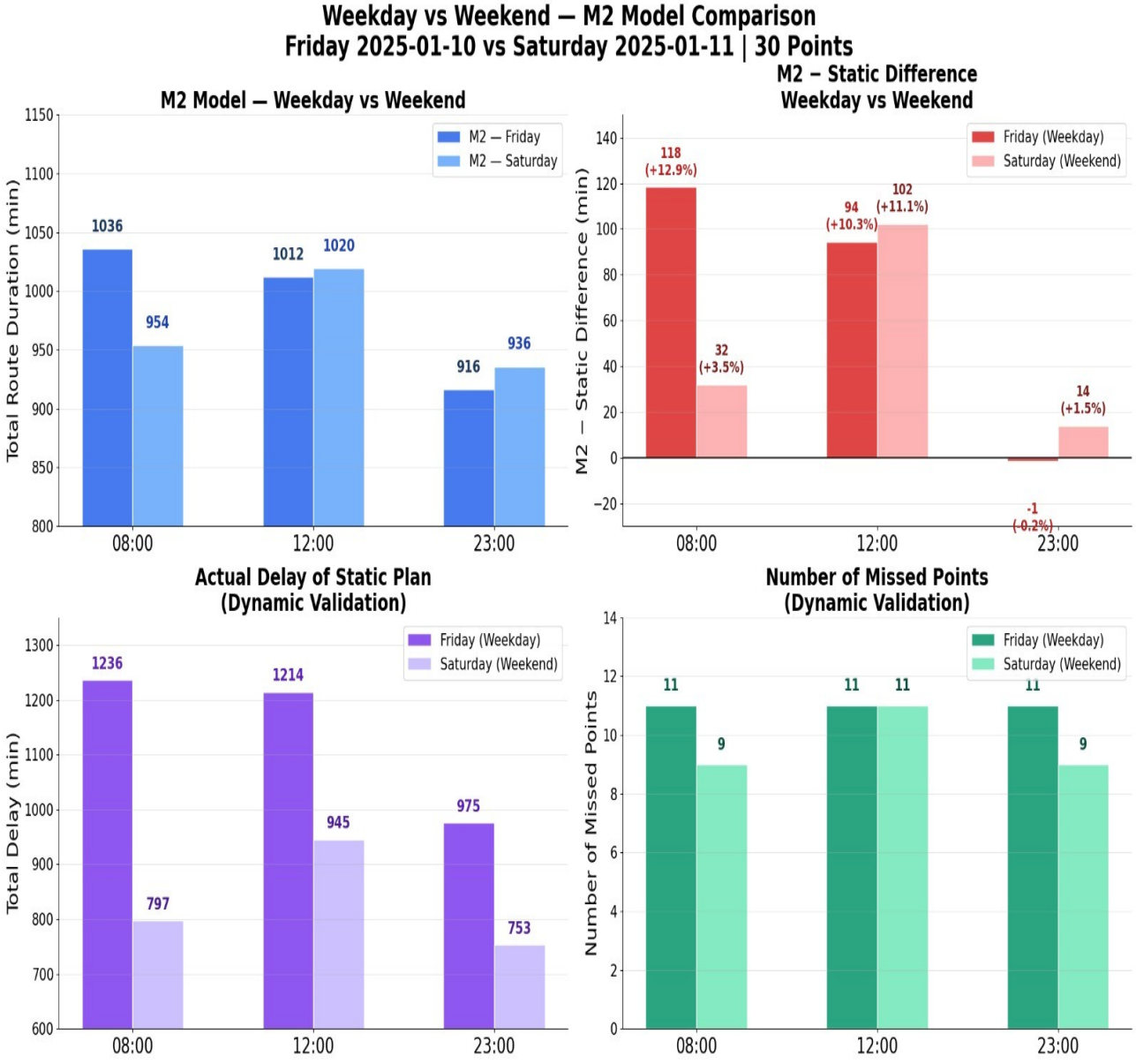

Figure 8. Weekday vs. weekend model comparison.

4. DISCUSSION

The findings obtained in this study concretize the impact of a pipeline integrating traffic prediction with vehicle routing optimization at three different levels.

4.1 Evaluation of Model Performance

When model performance is evaluated, achieving R^2=0.856 accuracy with the M2 model is a strong result when considered in isolation. However, what is truly decisive in this study is not the absolute accuracy value but the spatial generalization capacity that geographic features contribute to the model. While the temporal test difference between M1 and M2 is only 0.036, the difference in the spatial holdout test reaches +0.758. This finding raises a distinction frequently overlooked in traffic prediction literature: a good temporal test score does not guarantee that the model will be functional at new locations. Boukerche and Wang (2020) emphasized that spatial generalization capacity is a critical criterion in evaluating machine learning-based traffic prediction models; the spatial holdout test findings of this study concretely confirm this emphasis.

The higher accuracy achieved by M3 and M4 models is an expected and explainable result. Traffic conditions from the same hour of the previous week serve as a strong predictor in a city like Istanbul with repeating weekly patterns. However, this performance advantage comes with an operational cost. The selection of M2 is therefore not only a technical but a strategic decision. A less accurate model that works under all conditions is operationally superior to a more accurate but fragile model that works only under certain conditions. Shahbazian et al. (2024) used a similar framework when evaluating the operational applicability of hybrid systems and demonstrated that generalization capacity is as decisive as accuracy in model selection.

The preservation of performance in the range of R^2=0.847–0.884 with January 2025 data is particularly noteworthy. Subaşı (2025) achieved R^2=0.8486 with the GWO-XGBoost combination on Istanbul traffic data. The M2 model in this study remaining within a similar accuracy range with data from January 2025 confirms that gradient boosting-based approaches can model Istanbul traffic dynamics in a stable manner.

4.2 Evaluation of Routing Findings

When routing findings are evaluated, the fact that the M2 model produces longer plans than the static model under peak hour conditions appears to be a disadvantage at first glance. However, this impression reflects a common misconception. The dynamic validation analysis concretely revealed this error. The static model claims to reach 28/30 points under hard time windows, while in reality only 19 can be reached. Figliozzi (2012) quantitatively examined the effect of traffic density on time windows and demonstrated that the fixed speed assumption leads to serious planning errors particularly

during morning peak hours. The dynamic validation findings of this study measure the magnitude of this error in the Istanbul context at 32%.

The increase in M2's advantage as problem scale grows is also an important finding. While traffic effects accumulate in a limited number of segments in small-scale operations, in the 30-point scenario each vehicle passes through dozens of segments consecutively and the delay in each segment cumulatively transfers to the final points. This finding is consistent with the cumulative delay effect demonstrated by Li et al. (2010) in their stochastic travel time VRPTW study.

The weekday and weekend comparison is perhaps the analysis that most clearly demonstrates M2's value. The drop from 12.9% on Friday morning to 3.5% on Saturday morning proves that the model's advantage is directly linked to traffic density. Kim et al. (2015), while examining the dynamic effects of traffic conditions in urban routing problems, reached a similar conclusion and emphasized that traffic-aware planning plays a decisive role particularly in weekday morning operations.

4.3 Limitations

The methodological and data-related limitations of this study should be explicitly addressed. The traffic data covers only locations with sensors, and underrepresentation is an issue in Istanbul's peripheral districts. The model was trained only on 2024 data; regular updates will be required to capture traffic dynamics that change over the years. Furthermore, the single depot and homogeneous fleet assumptions do not fully reflect the complexity of real logistics operations.

Dynamic validation in this study is based on model-predicted travel times rather than observed travel times from real sensors. While the M2 model was validated against January 2025 sensor data at R^2=0.863–0.884, predicted travel times are inherently smooth estimates that may underrepresent the stochastic variability of real traffic conditions — sudden incidents, road closures, or weather events that are not captured in the training data. Consequently, the reported error rates and delay figures should be interpreted as conservative estimates; the actual performance gap between static and traffic-aware planning under real operational conditions may be larger than reported here.

5. CONCLUSION

This study combined a machine learning prediction system modeling Istanbul-specific traffic dynamics with the Vehicle Routing Problem with Time Windows within a single integrated pipeline. Travel times derived from traffic predictions were transferred to road network edges via Dijkstra's algorithm and converted directly into routing decisions. The effectiveness of the developed framework was evaluated comparatively with a static planning approach based on fixed speed assumptions at the levels of model accuracy, segment analysis, and fleet planning.

At the model level, the most decisive finding relates to spatial generalization capacity. While the base-

line model collapsed with R^2=–0.340 at locations it had never seen, the M2 model achieved R^2=0.418, and the contribution of geographic features to spatial generalization capacity was measured at +0.758. Performance in the range of R^2=0.863–0.884 was preserved in independent external validation conducted with January 2025 data. These results demonstrate that the model has a generalizing rather than memorizing structure and can operate reliably across different time periods and new locations.

At the segment level, the contribution of traffic information to route decisions was concretized. The Esenyurt–Üsküdar route, which the static model planned at 53.7 minutes during morning peak hours, took 64.8 minutes in the M2 environment. Under nighttime conditions, the M2 model leveraged traffic fluidity to fall 8.2 minutes below the static model. It was observed that the two models propose not only different durations but also different routes, demonstrating that traffic information shapes planning not only in terms of duration but also in terms of geographic decision-making.

At the fleet level, the most critical finding of the study was obtained from the dynamic validation analysis. While the static model planned to reach 28 out of 30 points on time under hard time windows, simulating this plan in the M2 environment showed that only 19 points could be reached. This 32% error rate proves that plans produced without traffic information render customer commitments unfulfillable from the outset. This gap widens as problem scale grows and traffic density increases.

When all these findings are evaluated together, the fundamental contribution of this study can be summarized as follows: by developing a workable pipeline bridging traffic prediction and vehicle routing, operational outputs that neither field could produce independently were obtained. In cities like Istanbul that are dependent on bridge crossings and where traffic density changes dramatically on an hourly basis, the operational counterpart of this transformation is concrete and measurable. The integration of traffic information into logistics planning processes should be regarded in this context not merely as a performance improvement but as a prerequisite for being able to make reliable service commitments.

REFERENCES

Boeing, G. (2017). OSMnx: New methods for acquiring, constructing, analyzing, and visualizing complex street networks. Computers, Environment and Urban Systems, 65, 126-139.

Boukerche, A., & Wang, J. (2020). Machine learning-based traffic prediction models for intelligent transportation systems. Computer Networks, 181, 107530.

Bratsas, C., Koupidis, K., Salanova, J.-M., Giannakopoulos, K., Kaloudis, A., & Aifadopoulou, G. (2020). A comparison of machine learning methods for the prediction of traffic speed in urban places. Sustainability, 12(1), 142.

Cordeau, J. F., Desaulniers, G., Desrosiers, J., Solomon, M. M., & Soumis, F. (2002). VRP with time windows. In P. Toth & D. Vigo (Eds.), The Vehicle Routing Problem (pp. 157-193). Philadelphia: SIAM.

Dantzig, G. B., & Ramser, J. H. (1959). The truck dispatching problem. Management Science, 6(1), 80-91.

Dijkstra, E. W. (1959). A note on two problems in connexion with graphs. Numerische Mathematik, 1(1), 269-271.

Figliozzi, M. A. (2012). The time dependent vehicle routing problem with time windows: Benchmark problems, an efficient solution algorithm, and solution characteristics. Transportation Research Part E, 48(3), 616-636.

Ichoua, S., Gendreau, M., & Potvin, J. Y. (2003). Vehicle dispatching with time-dependent travel times. European Journal of Operational Research, 144(2), 379-396.

Istanbul Metropolitan Municipality [IMM]. (2024). Hourly traffic density data set [Dataset]. Retrieved October 2024, from https://data.ibb.gov.tr/dataset/hourly-traffic-density-data-set

Kim, G., Ong, Y. S., Heng, C. K., Tan, P. S., & Zhang, N. A. (2015). City vehicle routing problem (City VRP): A review. IEEE Transactions on Intelligent Transportation Systems, 16(4), 1654-1666.

Li, X., Tian, P., & Leung, S. C. H. (2010). Vehicle routing problems with time windows and stochastic travel and service times: Models and algorithm. International Journal of Production Economics, 125(1), 137-145.

Meteostat. (2024). Meteostat: Historical weather and climate data [Software]. Retrieved October 2024, from https://meteostat.net

Niemeyer, G. (2008). Geohash [Software]. Retrieved October 2024, from https://en.wikipedia.org/wiki/Geohash

OpenStreetMap Contributors. (2024). OpenStreetMap [Geographic database]. Retrieved October 2024, from https://www.openstreetmap.org

Perron, L., & Furnon, V. (2023). OR-Tools [Software]. Google. Retrieved October 2024, from https://developers.google.com/optimization

Prokhorenkova, L., Gusev, G., Vorobev, A., Dorogush, A. V., & Gulin, A. (2018). CatBoost: Unbiased boosting with categorical features. Advances in Neural Information Processing Systems, 31, 6638-6648.

Shahbazian, R., Pugliese, L. D. P., Guerriero, F., & Macrina, G. (2024). Integrating machine learning into vehicle routing problem: Methods and applications. IEEE Access, 12, 93087-93115.

Solomon, M. M. (1987). Algorithms for the vehicle routing and scheduling problems with time window constraints. Operations Research, 35(2), 254-265.

Subaşı, N. (2025). Optimization of Istanbul urban traffic data with grey wolf optimization-assisted machine learning techniques: Comparative analysis of long short-term memory and eXtreme gradient boosting. ELECTRICA, 25(1), 1-15.

Voudouris, C., & Tsang, E. P. K. (1999). Guided local search and its application to the traveling salesman problem. European Journal of Operational Research, 113(2), 469-499.

ADVANCES IN GEOMATICS

https://aigjournal.com advancesingeomatics@gmail.com

+90 262 303 32 46

e-ISSN: 3023-4980